The University of West Bohemia
Faculty of Applied Sciences

Diagnostics and modeling of high-power impulse magnetron sputtering discharges

Ing. Jan Lazar

A thesis submitted for the degree of
Doctor of Philosophy
in the field of
Plasma physics and physics of thin films

Supervisor: prof. RNDr. Jaroslav Vlček, CSc.
Department of Physics

In Plzeň, 2012

Západočeská univerzita v Plzni
Fakulta aplikovaných věd

Diagnostika a modelování vysokovýkonových pulzních magnetronových výbojů

Ing. Jan Lazar

disertační práce
k získání akademického titulu doktor
v oboru
Fyzika plazmatu a tenkých vrstev

Školitel: prof. RNDr. Jaroslav Vlček, CSc.
Katedra fyziky

V Plzni, 2012

I submit this thesis written at the Faculty of Applied Sciences, University of West Bohemia (The Czech Republic) for examining and defending.

I am pleased that I can express my gratitude to prof. Jaroslav Vlček who determined the subject-matter of this work, assessed the direction to take to fulfill the aims of the work and devoted his time and energy to give me a vital leadership. I am also obliged to all my colleagues and co-workers at the Department of Physics for the stimulating working environment they formed as well as for their feedback on the work I did. Especially the cooperation with Jiří Rezek and the consultations with Petr Zeman and Pavel Baroch were fruitful in order to solve the issues that emerged within the scope of this work. The comprehensibility of the thesis was enhanced by the review done by Šimon Kos.

Here, I would like to express my great thanks to my parents and siblings who provided me continuing support during my studies.

This work was supported by the Ministry of Education of the Czech Republic under project No. MSM 4977751302.

I hereby declare that I wrote the thesis myself using duly cited literature and results obtained and published during my Ph.D. study.

In Plzeň, 2012

Ing. Jan Lazar

Abbreviations

BG	Background Gas
DC	Direct Current
ECR	Electron Cyclotron Resonance
HiPIMS	High-Power Impulse Magnetron Sputtering
IES	Ion Energy Spectra (cs^{-1})
IED	Ion Energy Distribution ($eV^{-1}m^{-3}$)
IEDF	Ion Energy Distribution Function ($eV^{-1}s^{-1}m^{-2}$)
MS	Mass Spectroscopy
MW	Micro Wave
OAS	Optical Absorption Spectroscopy
OES	Optical Emission Spectroscopy
PVD	Physical Vapor Deposition
RF	Radio Frequency
RG	Reactive Gas
RGA	Residual-Gas Analysis, Reactive-Gas Atom
SIMS	Secondary Ion Mass Spectroscopy
TOF	Time of Flight

Basic Definitions

f_r	(Hz)	Pulse repetition frequency	
Γ	(m^{-2})	Density of particle flux	
I_d	(A)	Discharge current	
$\bar{I}_d$	(A)	Average discharge current	$\bar{I}_d = \frac{1}{T}\int_0^T I_d(t)dt$
I_s	(A)	Substrate current	
J_s	(Am^{-2})	Substrate current density	
J_t	(Am^{-2})	Target current density	
q	(sccm)	Gas flow rate	
Q	(s^{-1})	Gas flow rate	
Q_I		Ion charge state number	
$\bar{S}_d$	(Wm^{-2})	Average target power density	$\bar{S}_d = \frac{1}{T}\int_0^T U_d(t)J_t(t)dt$
S_{da}	(Wm^{-2})	Average target power density in a pulse	$S_{da} = \frac{1}{t_1}\int_0^{t_1} U_d(t)J_t(t)dt$
T	(s)	Pulse period	$T = 1/f_r$
t_1	(s)	Pulse-on time	
U_d	(V)	Discharge voltage	
U_{da}	(V)	Average discharge voltage in a pulse	$U_{da} = \frac{1}{t_1}\int_0^{t_1} U_d(t)dt$

Contents

1 Introduction **8**

2 The basic concepts of the magnetron sputtering **8**

2.1 Magnetron sputtering – general overview 8

2.2 HiPIMS techniques for film depositions 13

2.3 HiPIMS discharge plasmas 14

2.4 Reactive HiPIMS 16

2.5 Mathematical modeling of magnetron sputtering processes 18

3 Aims of the thesis **20**

4 Methodology **21**

4.1 Mass spectroscopy using Hiden EQP 300 instrument 21

4.1.1 Spectrometer structure and functioning 21

4.1.2 Spectrometer functioning in detail 25

4.1.3 Sensitivity of the spectrometer 27

4.1.4 Tuning the spectrometer 31

4.1.5 Spectra acquisition 35

4.1.6 Spectra interpretation 40

4.2 Calibration of the ion energy spectra 42

4.3 Deposition system and experimental conditions 46

4.3.1 Deposition system in general, basic definitions 46

4.3.2 HiPIMS depositions of zirconium 49

4.3.3 Reactive HiPIMS depositions of zirconium oxides 51

4.4 Measurements of film properties 52

4.5 Sputtering process analysis 52

4.6 Mathematical modeling of reactive sputtering processes 55

4.6.1 Model assumptions and governing equations 55

4.6.2 Setting the parameters of the model 64

5 Results and discussion 67

5.1 HiPIMS depositions of zirconium 67

5.1.1 Discharge characteristics 68

5.1.2 Ion energies and compositions of total ion fluxes 74

5.1.3 Deposition characteristics 84

5.1.4 Efficiency of the magnetron sputtering and the transfer of sputtered particles to the substrate 85

5.2 Diagnostics of reactive HiPIMS discharges 93

5.2.1 Control system settings 93

5.2.2 Discharge characteristics 95

5.2.3 Ion energies and compositions of total ion fluxes 97

5.3 Reactive HiPIMS depositions of zirconium-oxide films 102

5.3.1 Discharge characteristics 102

5.3.2 Deposition rates and optical properties of zirconium-oxide films 103

5.3.3 Elemental composition and structure of zirconium-oxide films 105

5.4 Mathematical modeling of controlled reactive HiPIMS depositions of zirconium oxides 107

5.4.1 Parameters of the model 107

5.4.2 Model results - process parameters and film stoichiometry 110

6 Conclusions 115

7 References 118

8 Publications of the candidate 126

8.1 Refereed journal papers 126

8.2 Conference papers and proceedings 126

1 Introduction

A multitude of physical vapor deposition techniques (PVD) are currently used for a surface treatment of materials. Magnetron sputtering is very often the process of choice since it enables the depositions of high-quality films of various chemical compositions and material structures on a large variety of substrate materials. The process is easily up-scalable from the laboratory conditions to the industrial production, depositions can be performed in non-equilibrium conditions and dangerous chemicals are often avoidable when compound layers are produced. The thesis is focused on the research in the field of a particular variant of the magnetron sputtering technique – 'the high-power impulse magnetron sputtering' (HiPIMS), which is characterized by making use of high instantaneous power densities which are dissipated into the discharge plasmas within low duty-cycle pulses at relatively low repetition frequencies.

Within the scope of the thesis, HiPIMS discharges were studied under various experimental conditions. An unbalanced magnetron equipped with a zirconium target was sputtered in pure argon atmosphere and in an argon/oxygen gas mixture. For the latter case, the properties of deposited films were analyzed and feedback control system was developed in order to control the film stoichiometry and the deposition rate. Discharges were analyzed by means of mass spectrometry and by investigation of target and substrate current-voltage waveforms and respective deposition rates. Methodology of ion flux measurements using Hiden EQP 300 apparatus is presented together with the procedure of the data interpretation. Mathematical model of the reactive sputtering process was implemented and used to predict the usability and limits of the developed control system.

2 The basic concepts of the magnetron sputtering

In this chapter, an overview of the magnetron sputtering is given. Then, the HiPIMS techniques are described from a technological and research perspective. The general aim of this chapter is to present the incentives for the thesis in the light of the current state of the art and to provide an appropriate summary of references. The intended reader is assumed to be familiar with basic concepts of the magnetron sputtering technology as described e.g. in Refs. [1-9]. For reader's convenience, the basic concepts of the magnetron sputtering are summarized in the following text.

2.1 Magnetron sputtering – general overview

Material sputtering was first observed in 1852 and was considered to be an unwanted dirt effect. It started to be utilized by the industry almost one century later due to substantial improvements of the vacuum equipment and an increasing demand for high-quality thin films [10]. The early sputtering systems were diode systems which suffered from many drawbacks stemming from relatively high operating pressures (around 100 Pa). Generally, deposition rate was low and the substrate thermal loading was high. Introduction of the planar magnetron in the mid 1970's made low-pressure depositions possible.

The plasma impedance in magnetron systems is significantly lower and mean free paths of the sputtered particles are in the range of centimeters [5,6]. Thus, the deposition rate attains higher values, typically from 1 nm/s to 10 nm/s for metallic films, the substrate thermal load is lower and the growing films, being hit by highly-energetic particles, exhibit a denser structure. Moreover, the substrate can be easily biased so that the energy of the ions striking the growing film is controlled. The so called 'structure zone models' or 'structure zone diagrams' have been developed to describe the resulting structure of the film by means of the sputtering process parameters such as the process pressure, the ion current onto the substrate, the substrate bias, the substrate temperature, etc. [2,11,12].

The requirements for the (i) high target utilization (ii) high deposition rate, (iii) better control over the film properties, (iv) substrate pretreatment and sufficient film-to-substrate adhesion, (v) deposition of insulating films and (vi) the need to coat complex substrate shapes have led to many modifications of the magnetron sputtering process. From the technological point of view, the particular solutions of the above mentioned requirements can be summarized as follows [1-3,6,13]:

Attain a high uniformity of the target erosion (i)

This issue is solved by an appropriate design of the magnetic field in the vicinity of the target.

Static magnetic fields – increase the magnetic field homogeneity:

- Magnetic field lines almost parallel to the magnetron target surface.
- Ferromagnetic plates placed into the magnetic circuit.

Movable magnets:

- Magnets move behind the magnetron target and "scan" it.

Movable sputtering targets:

- Tubular magnetrons – rotation of the cylindrical cathode around the static magnets.

Increase the sputtering efficiency (ii, iii)

Reducing the surface binding energy of the sputtered material:

- Sputtering from target operated at elevated temperature [14].

Increasing the sputtering yield:

- Serial co-sputtering – heavy atoms beneath the target surface "reflect" the collision cascade back towards the target surface [6].
- Lowering the poisoning of the target erosion zone when reactive sputtering is employed – sputtering yield from the surface covered by the compound is about 10 times lower [15].

Enhance the transport of sputtered particles towards the substrate (ii, iii)

Avoid the scattering from the process gas.

- Decrease the system pressure and/or target-to-substrate distance.
- Attain a sustained self-sputtering mode of the discharge.

Avoid the backward flux of ionized sputtered species onto the target:

- Do not apply high current densities in long-lasting (more than approximately 50 μs) pulses onto the target.

Use the magnetic field to enhance the transport of the charged sputtered particles along magnetic field lines:

- Unbalanced magnetrons.
- A closed-field or a mirror-field configuration of the set of magnetrons [16].
- Additional coils in the region between the target and the substrate [9,17,18].
- Sources generating dense plasma in the target region – ionized fraction of sputtered particles move along magnetic field lines (e.g., hollow cathode magnetrons, HiPIMS).

Use the electric field to enhance the transport of the charged sputtered particles:

- Apply a bias on the substrate to extract the sputtered ionized material towards it [19].

Repel the ionized sputtered particles from the target:

- Switch the target potential to positive values – RF or pulsed bipolar DC sputtering [3].

Control the energy of the particles striking the substrate (iii, iv, v)

Use the initial energy of sputtered particles:

- Low system pressure and/or target-to-substrate distance.
- Make use of ‘gas rarefaction’ - apply high target current densities, process-gas is then rarefied due to the ‘sputtering wind’ and scattering from the process gas is lower.

Accelerate sputtered particles from the target:

- Switch the target potential to high positive values [3,20].
- A negative target voltage accelerates negative ions that are formed at the target surface or in the sheath/pre-sheath domains (particularly when a compound formed on the target surface is sputtered during reactive depositions) [21,22].

Utilize the plasma at the substrate position – requires a sufficient plasma density (ion current) or a high electron temperature (floating potential) at the substrate position. The potential energy of ions with respect to the substrate surface and the energy of excited plasma species must be taken into account too:

- Make use of the plasma generated by the target power – enable the plasma transport towards the target (e.g. by a magnetic field configuration).
- Additional plasma source in the system (RF antenna or the electron cyclotron resonance [ECR] discharge) [18,23].

Apply an additional electric field between the substrate and the target:

- Substrate biasing – DC, pulsed DC or RF voltage, synchronizing target and substrate voltage sources [3].
- Biased grids between target and substrate [24].

Control the direction of the particles striking the substrate (iii, v)

Use the scattering by process-gas particles:

- Set an adequate system pressure – covering the trench and via structures by neutral particles requires mean free paths shorter than the characteristic dimension of the feature to be covered.

Employ inherent electric fields at the plasma-substrate interface to drive the directions of ions (see the paragraph '**Control the energy of the particles striking the substrate**' on p. 10). At the same time, the above mentioned scattering by process gas should not be neglected:

- Set the conditions (i.e., plasma density, electron temperature, substrate bias) to get plasma sheath thickness lower than the characteristic dimension of the substrate feature to be covered.
- Tilt the substrate surface – usable only if particle scattering is low [25].

Control the composition of particle fluxes onto the substrate (iii, iv)

- Equip the magnetron with a target of an appropriate chemical composition.

Control the composition of the working atmosphere:

- Set the process-gas pressure – the flux of the process-gas ions onto the substrate corresponds to the number density of process-gas particles. The effect of process-gas neutrals on the film properties is often negligible.
- Control of reactive-gas pressure – both reactive-gas neutrals and ions form the film (see the paragraph '**Control the reactive-gas partial pressure**' on p. 12)
- Make use of the "gas rarefaction" – see the paragraph '**Control the energy of the particles striking the substrate**' on p. 10).

Adjust the geometry of reactive-gas inlets – the position and orientation of gas inlets strongly affects the flux of the reactive-gas particles onto the target and onto the substrate. The use of this approach is limited by process-gas pressures due to scattering effects [15].
Change the ion-to-neutral ratio in the flux onto the substrate:

- Set the target-to-substrate distance and/or system pressure – the flux magnitude of the sputtered neutral particles may change differently with the distance from the target as compared to the flux magnitude of ionized sputtered particles (see the paragraph '**Enhance the transport of sputtered particles towards the substrate**' on p. 9).
- Additional plasma source in the system (RF antenna or ECR discharge) [9,18,23,26].

Control the substrate temperature (iii, iv)

External heating:

- Ohmic heating, radiant heating.

Utilizing the plasma:

- Heating by an ion current drawn from the plasma – negative substrate bias. Note that the process-gas ions may embed into the film and subsequently escape resulting in increased tensile stress.
- Heating by an electron current drawn from the plasma – positive substrate bias must be set for a fraction of the deposition time.
- Radiation from the plasma inevitably heats the growing film.

Control the reactive-gas partial pressure (ii, iii, vi)

Operate the reactive-gas supply via feedback loops. Feedback loops can be divided according to the adopted sensing method:

- Sensing of the reactive-gas pressure – optical emission spectroscopy, mass spectroscopy, lambda probes.
- Sensing of the flux of sputtered particles – optical emission spectroscopy, mass spectroscopy.
- Measuring the target and/or plasma impedance – discharge current-voltage characteristic.

The reactive-gas control can be further enhanced by suppressing the target poisoning:

- Provide a high pumping speed.
- Adjust the reactive-gas inlet geometry.
- Make the target erosion zone smaller.

Avoid the arcing at the target surface (iii, vi)

Eliminate the positive charge accumulated on the target surface as a result of a positive ions bombardment – attract the electrons from the plasma towards the target:

- RF sputtering – limited by cathode dimensions [15].
- Pulsed DC sputtering – unipolar or bipolar pulses [27,28].

Counter the disappearing anode effect (vi)

Cleaning the surface of the electrodes by sputtering:

- The use of multiple targets – each time some of the targets act as the cathode and are sputter-cleaned, others serve as the anodes and are being poisoned. Later on, their roles are switched.

2.2 HiPIMS techniques for film depositions

'High-power impulse magnetron sputtering' (HiPIMS), sometimes also called 'high-power pulse magnetron sputtering' (HPPMS) is an emerging physical vapor deposition technique. In recent years, various HiPIMS systems have been used for the deposition of films and characterized [29-38]. Generally, they use conventional magnetron designs but the target power density in a pulse attains a peak value of up to several $kWcm^{-2}$ which is considerably higher than a typical target power density (usually less than 10 Wcm^{-2}) applied in the conventional DC magnetron sputtering. The high-power pulses with relatively low duty cycles (up to about 10%) are applied on the target at low frequencies (50 Hz – 10 kHz) to prevent target overheating. Consequently, very dense discharge plasmas with high degrees of ionization of the sputtered atoms are generated and the film deposition can be carried out at highly ionized fluxes of the sputtered target-material atoms [39-41]. As follows from the overview given above (see Sec. 2.1 [p. 8]), this is of significant interest for a directional deposition into high-aspect-ratio trenches and via structures, for substrate-coating interface engineering, and for ion-assisted growth of films [9,25]. From the application perspective, it is crucial to investigate the capabilities of the deposition system (i) to achieve a reasonable deposition rate, (ii) to produce films free from macroparticles, (iii) to generate desired ion fluxes onto the substrate and (iv) to attain a sufficient ionization degree of the sputtered particles at the substrate position [34,42-48].

HiPIMS technique development and requirements

The early HiPIMS systems made use of discharging the energy stored in a capacitor bank into the plasma in a rather uncontrolled manner resulting in system-dependent current-voltage waveforms [29]. A further development was directed towards HiPIMS power sources and techniques with the ability (i) to generate a well-defined shape of the voltage waveform during the pulse – either rectangular or arbitrarily shaped, (ii) to avoid the transition from the glow discharge to arc, (iii) to suppress the arcs that have already emerged, particularly as a consequence of the formation of insulating films at the target during reactive deposition processes, (iv) to operate the target in combination with other sources – e.g. with DC or pulsed DC power sources, (v) to synchronize the target and substrate bias voltages and (vi) to integrate a HiPIMS operated target in systems with additional plasma sources, such as RF coils [18,27,28,34,49,50]. Slightly apart from these general trends, there is an effort to develop (i) systems capable of operation in gasless sustained self-sputtering mode, meaning that the plasma is composed only of sputtered target-material species, (ii) systems generating arbitrarily shaped pulses of low frequencies and relatively long pulse-on times; the technique is called 'modulated pulsed power magnetron sputtering' (MPPMS) and (iii) the development of systems generating high-power pulsed sputtering discharges without using a magnetic field [35-37,51-53].

Open problems

The performance of HiPIMS systems is strongly dependent on the pulse parameters, such as pulse-on time, average target power density in a pulse, shape of the current and voltage waveforms etc. Nevertheless, the studies performed to uncover the interdependencies between HiPIMS discharge

parameters and deposition characteristics are still not allowing us to fully understand the processes of ionization and transport of the sputtered species.

2.3 HiPIMS discharge plasmas

Generally, the HiPIMS discharge plasmas are experimentally studied by the same diagnostic tools as plasmas generated by other sources, i.e. by optical emission/absorption spectroscopy (OES, OAS) [18,40,54,55], Langmuir probe [18,56-59] mass spectroscopy (MS) [21,60-63] and time-of-flight spectroscopy (TOF) [64]. The investigations of temporal evolutions of discharge plasmas throughout the pulse are of key importance for understanding the plasma behavior. That is why time-resolved techniques are often used and why it is always essential to provide corresponding discharge current-voltage waveforms when the results of HiPIMS experiments are presented.

Formation of HiPIMS plasmas

Low duty cycles and low pulse frequencies used in HiPIMS processes result in long off-times between subsequent pulses, typically several hundred or thousand μs. In some cases, plasma decay processes have time constants on the order of hundreds of μs, so excited ionic and neutral species could be present at the target vicinity in considerable amounts even after several hundred of milliseconds after the voltage pulse termination [61,65,66]. Nevertheless, the deficiency in the plasma species at the pulse beginning increases the time of the pulse onset, especially at low pressures, or even disables the plasma ignition [29,60,61]. To avoid the stochastic nature of the pulse formation or slow pulse run-up, there is sometimes a need for plasma ‘pre-ionization’. Technically, this is achieved by employing a low-current discharge before the main high-power pulse [4,34,49,66,67].

Temporal evolutions of HiPIMS plasmas

Once the discharge has been ignited, there is a sharp increase in the discharge current which reaches its maximum in a few tens of μs. At the same time, the plasma density starts to rise and peak values on the order of 10^{12} cm^{-3} are readily obtained. Based on measured electron densities and temperatures, the dominant ionization mechanism is recognized to be the electron impact ionization. If the pulses last longer than typically 50 μs, an increase in the plasma impedance further within the pulse is usually observed. This phenomenon is commonly attributed to a particle density reduction in front of the target caused by collisions of the process-gas particles with the sputtered ones (the ‘sputtering wind’. The plasma composition changes within a pulse and the sputtered species start to play a more important role. Depending on the target current density and target-material’s properties (ionization cross-section, self-sputtering yield and secondary-electron emission coefficient), the plasma may “switch” to a sputtered-material-dominated state and even to a sustained self-sputtering regime. Typically, in this phase, higher charge-states of the sputtered material ions are formed. Due to the corresponding change in the plasma impedance, the current-voltage characteristics of the discharge also vary [40,42,64].

Some works have reported populations of electrons with high energies of even several tens of eV at the pulse beginning causing plasma floating potential to drop for a few μs to values of minus several tens of volts with respect to the grounded chamber walls [56,59,68]. After an initial drop, the plasma floating

potential attains low negative values typically no lower than -10 V. Later on, the effective electron energy approaches values on the order of units or tenths of eV and does not change significantly, but a group of electrons with relatively high energies is still present. Since the excitation and ionization energies of the sputtered material are typically lower than those of the used process gas and the density of the sputtered species rises considerably, the population of high-energy electrons tends to be reduced as the pulse develops [56-59,69]. The spatial distribution of the plasma potential is rather complicated due to the presence of the magnetic field and the plasma potential could be negative with respect to the grounded chamber walls even at a distance of several centimeters from the target [68,70,71]. But usually, further from the target, the plasma potential is close to zero at the pulse beginning and it attains positive values of a few volts within the pulse [57-59].

Other HiPIMS-related phenomena

As a result of high instantaneous power densities dissipated in the magnetron plasma, new phenomena which are not observed at moderate power loadings emerge. The most pronounced ones are (i) the decrease in the deposition rate and (ii) glow-to-arc transitions. These two effects impose severe practical limitations on the application of HiPIMS [34,44,46,72]. The first effect is generally attributed to a transition from a process-gas-dominated to a sputtered-material-dominated discharge and a corresponding decrease in the sputtering yield together with an increased backward flux of ionized sputtered particles onto the target. The second one stems either (a) from the high current densities on the target causing the thermal emission of electrons from the target surface or (b) from the break-down of the insulating layer formed on the target surface. Other phenomena observed in HiPIMS discharges are: (iii) ion acoustic solitary waves, (iv) an anomalous transport of electrons across the magnetic field accompanied by a creation of intrinsic electric fields in the MHz range which may cause a deflection of ions and thus a decrease in the deposition rate, (v) oscillations of the electron density at a relatively low frequencies (12.5 kHz) even quite long after the HIPIMS pulse was terminated, (vi) rising oscillations of the discharge current when the sustained self-sputtering regime is achieved and (vii) magnetic field changes caused by high instantaneous fluxes of charged particles [4,62,73-76].

Open problems

From the standpoint of HiPIMS applicability, it is essential to grasp the connection between deposition process parameters (e.g. pulse-on time, discharge voltage, pulse frequency, process-gas pressure, magnetic field configuration etc.) and properties of particle fluxes onto the substrate. The energy distributions of individual ionic species bombarding the growing films and the composition of total ion fluxes onto the substrate are of key importance for the characterization of the HiPIMS sources and for a good understanding of the deposition processes. Nevertheless, the relationships between deposition process parameters, discharge characteristics and ionic fluxes onto the substrate are still not well understood. In addition, the information on the settings of the diagnostics equipment (mass spectrometers in our case) and on the procedure of interpretation of measured data is often incomplete in the literature.

2.4 Reactive HiPIMS

The ability of the HiPIMS technique to generate highly ionized fluxes of particles at the substrate position was a strong incentive to adapt HiPIMS also to the field of reactive sputtering, i.e. to sputter a metallic or compound target(s) in an atmosphere containing "reactive" species such as nitrogen, oxygen, hydrogen, carbon dioxide etc. The main benefits expected are, as stated in Sec. 2.1 (p. 8) and Sec. 2.2 (p. 13), a better control over the film properties and a better coverage of complex substrate structures (e.g. high-aspect-ratio trenches) when compared to other sputtering processes. It was demonstrated that it is possible to prepare a multitude of material systems, e.g. TiO_2, Al_2O_3, ZrO_2, CrN, TiN, etc. [27,28,38,77-79]. Just like the other reactive sputtering processes, the reactive HiPIMS faces two key obstacles resulting from the formation of a compound on the target surface ('target poisoning') – the hysteresis effect and arcing. Solutions of these are discussed in the text below.

Key physical processes, plasma-target interactions

The reactive sputtering process is greatly influenced by the state of the target surface since it determines (i) the emission and recapture of secondary electrons (and thus the discharge impedance), (ii) the sputtering yield of the target material (and thus the deposition rate and the reactive-gas consumption) and (iii) the flux of accelerated negative ions out from the target (these ions may originate on the target surface as a consequence of sputtering of a compound). Reactive-gas species interact with the target surface in the following manner – they (i) are adsorbed on the surface, (ii) form a compound with the target material and (iii) are implanted into the target's sub-surface regions; the implantation depth is estimated to be 2 nm – 7 nm. It was observed, that adsorbed species may influence the 'effective secondary electron emission' (i.e. the overall balance between electron emission and recapture processes) in a different manner than a compound formed on the surface [80-87].

The main features of the HiPIMS mode of operation, i.e. (i) high instantaneous target power densities, (ii) a low pulse repetition frequency and (iii) low duty-cycle result in several specifics in target poisoning. The relatively high cathode voltage and plasma density during the pulse cause an extensive implantation of ionized reactive species into the target sub-surface regions. Furthermore, chemisorbed or compound-forming atoms of the reactive gas which are located at the target surface are also "knocked" into the sub-surface regions by particles accelerated towards the target. Then, the role of the compounds formed in the sub-surface region of the target is more significant as compared to the other magnetron sputtering processes. Also the time necessary for the sputter-removal of the compound from the target is longer (typically on the order of minutes) causing a gradual drift in the process characteristics such as a decline in the target erosion rate (accompanied by the decrease in the deposition rate) and a progressively less pronounced hysteresis effect [88,89].

Reactive sputtering – control strategies

The key physical phenomenon to be coped with in reactive sputtering processes is an intrinsic positive feedback loop of the sputtering process causing an abrupt poisoning of the target surface. Briefly, these are the stages of an uncontrolled target poisoning:

1. Increase in the reactive-gas partial pressure. → **2.** Higher target poisoning. → **3.** Lower target erosion, i.e. also lower deposition rate. → **4.** Lower gettering of the reactive gas by sputtered species → **1.**

The transition from the 'metallic', i.e. compound-free, to a 'poisoned' target state is hysteretic and imposes additional demands on the deposition control system.

As clearly seen, the main challenge associated with the hysteresis is to fabricate films of desired chemical composition at a reasonable deposition rate which implies the need for process stabilization, i.e. to control the target poisoning. Unfortunately, chemical compounds formed on the target are often electrically insulating causing charging of the poisoned surfaces, which leads to arcing when the critical value of electric field intensity across the compound layer is attained. Some authors have reported disappearing of the hysteresis effect during reactive HiPIMS and explained it as a consequence of an enhanced sputter-cleaning of the target surface during the high-power pulse [72,77]. Nevertheless, more detailed studies did not confirm this and the existence of a hysteresis loop seems to be inherent also to reactive HiPIMS [88-90].

Several approaches to handle the hysteresis are currently used:

- Suppression of the hysteresis by the system configuration – (i) increase of the pumping speed, (ii) impeding the flow of reactive species towards the target, (iii) decrease of the flux of the sputtered species onto the substrate and (iv) sputtering from small area targets [7,8,15,91].
- Two-step process – sputter deposition of several monatomic layers of the target-material onto the substrate and a successive exposition to the plasma-activated reactive species [7].
- Pulsing the flow of the reactive gas into the deposition system [78].
- Feedback control of the process by adjusting the reactive-gas flow rate or discharge power. [7,8,79,92,93].

Arcing is reduced through:

- Capabilities of power supplies to detect an arc (via sudden current rise or voltage drop) and switch off the discharge transitorily.
- Integration of HiPIMS power supplies with power supplies with inherent ability to suppress the arcing – combined pulsed DC and HiPIMS sputtering [27].

Feedback control techniques

Feedback control of the reactive sputtering process is preferred to the other above mentioned strategies for it does not require any extensive modifications of the deposition system. Just the sensor(s), controller and actuator(s) must be installed. At first, it is essential to decide which property of the deposition process is the representative one with respect to the application requirements and which are the adequate process parameters to be driven. Additionally, the response time of the feedback loop should be sufficiently short to allow for a stable deposition and homogeneous properties of the deposited film.

Common currently used sensors allow for the on-line measurements of:

- Deposition rate – piezoelectric crystal sensors.
- Flux of the sputtered material – OES [90,93].
- Number density of the reactive species – OES, MS, lambda probe [27,92].
- Discharge impedance – current-voltage waveforms [7,8].

Controlled process parameters are usually:

- Reactive-gas flow into the system – driven by gas flow operating valve(s).
- Discharge power – driven by (i) target voltage, (ii) pulsing frequency or by (iii) pulse-on time [27,28,32].

Open problems

Several works reported on depositions of oxide films using a reactive HiPIMS controlled via a feedback loop and on the relation between deposition parameters and film properties. However, the deposition rates did not exceed 50 nm/min and the fluxes of the film forming species onto the substrate were rarely investigated. The feedback loops employed predominantly OES and lambda-probe sensors. It is not clear whether the information on discharge impedance could be utilized for an effective control of the system. The impact of the gas inlet configuration on the process controllability and on the film properties is also not satisfactorily explored.

2.5 Mathematical modeling of magnetron sputtering processes

Besides the diagnostics of the magnetron sputtering process, mathematical models may give us a profound insight into the underlying physics. Some process properties are even inaccessible via contemporary measurement techniques and an appropriate model can provide us with the desired information. In the following paragraphs, the models of discharge plasmas and sputter depositions are presented. Models of film growth are not included in this overview.

Overview of the models

In general, the direct solution of the key governing equation, i.e. the Boltzmann equation is mathematically a very complicated and complex task. For that reason its approximations are commonly employed. Due to the complexity of the model, the corresponding sets of equations are solved numerically using various approaches and computer codes. Currently used models of plasmas can be divided into two main groups – particle and fluid – depending on the way they treat plasma species. Particle models handle the plasma as a set of individual particles and store the information on the state (position, velocity etc.) of each of them. Naturally, these models employ statistics and probabilities since only a small fraction of the particles can be simulated. Basically, any information on the plasma can be obtained from a particle model but the complexity of the models is limited by computational restrictions. On the other hand, fluid models, which are based on the velocity moments of the Boltzmann transport equation treat the plasma species as

individual fluids. Inherently, these models assume the particle distribution functions to be of a certain form. Thus, it is not possible to compute the distribution functions for they serve as an input parameters of a fluid model. This implies that some properties, e.g. collision frequencies, may be calculated incorrectly when the system is out of a local thermodynamic equilibrium. The applicability of the fluid approach is further limited by the value of the 'Knudsen number', which is the ratio of the mean free path of the particles and the characteristic length of the modeled system. Fluid models are unusable for the cases of high values of the Knudsen number [94-96].

Generally, models of plasmas can be classified based on these criteria:

- Handling of plasma species – particle / direct solution of the Boltzmann equation / fluid.
- Time dependence – steady-state / time-resolved.
- Dimensionality – homogeneous / one- / two- or three-dimensional.
- Interdependencies between properties of the modeled system – all properties are self-consistently evaluated / some of them are input.
- Calculation method – analytical / numerical / probabilistic.

In addition to the above mentioned classification, particular plasma processes are often modeled using different modeling approaches and then integrated into one complex ('hybrid') model. This is done in order to optimize the calculation time and with respect to the demanded output of the model [97,98].

Analytical models

Analytical models represent a specific class of non-particle models which consider the modeled system to be homogeneous or divided into a few space domains. These models employ a relatively low number of equations targeting some particular phenomena. The solution is readily obtained and the models are very fast but approximate and valid only over a limited range of conditions. Examples of analytical models are models of the cathode sheath region, ionization processes, ion implantation into the cathode, electronegative discharges, etc. [86,99-102].

Open problems

The main issues related to the HiPIMS technique are (i) to increase its relatively low deposition rate (ii) to attain a high ionization degree of the sputtered species in the flux onto the substrate and (iii) to fabricate non-conducting films using a reactive HiPIMS. Recently, several analytical models have been developed to gain the understanding of (i) the processes of target poisoning/sputtering and (ii) pathways of plasma species during reactive sputtering processes [91,103-105]. These models can be applied also to the HiPIMS mode of operation. It would be beneficial to match the parameters of reactive HiPIMS models with the measured data and to investigate the capabilities of the models to gain the development of the control systems for reactive HiPIMS.

3 Aims of the thesis

Based on the open problems for research of high-power impulse magnetron sputtering (HiPIMS) processes as presented in the previous section, the areas of interest and particular research tasks were stated as follows:

Mass spectroscopy

(1) Develop a consistent methodology of the spectrometer tuning and of the ion energy spectra acquisition in order to investigate the ion fluxes in the case of HiPIMS discharge plasmas.

(2) Develop a methodology of the ion energy spectra interpretation with focus on the interpretation of the spectra of multiply charged ions.

HiPIMS depositions of zirconium films

(3) Set up the system for HiPIMS depositions of zirconium films.

(4) Perform measurements of discharge characteristics.

(5) Perform measurements of the ion energy spectra in the face-to-face spectrometer-to-target setup.

(6) Use the measured deposition characteristics and ion energy distribution functions to analyze the deposition process.

Reactive HiPIMS depositions of zirconium-oxide films

(7) Develop a system for controlled reactive HiPIMS depositions of zirconium-oxide films.

(8) Perform measurements of discharge characteristics.

(9) Perform measurements of the ion energy spectra in face-to-face spectrometer-to-target setup.

(10) Analyze the properties of deposited films.

(11) Provide a volume-averaged mathematical model of the controlled reactive sputtering process and use it for the analysis of the zirconium-oxide depositions.

4 Methodology

In this chapter, the necessary theoretical background is provided in order to explain the functioning of the mass spectrometer and the acquisition and the interpretation of data measured (Sec. 4.1 [p. 21]). The procedure of the calibration of the ion energy distribution functions is also given (Sec. 4.2 [p. 42]). Then the experimental setup for HiPIMS experiments is described together with the control system used for the reactive HiPIMS depositions (Sec. 4.3 [p. 46]). After that, the methods used for evaluation of film properties are described (Sec. 4.4 [p. 52]) and the mathematical models employed to elucidate some of the physical processes taking place in the deposition system during HiPIMS is presented (Sec. 4.5 [p. 52], Sec. 4.6 [p. 55]).

4.1 Mass spectroscopy using Hiden EQP 300 instrument

The basic principles of the spectrometer's functioning are well-described in the user's manual provided by Hiden Analytical. However, there is a lack of information on measurements of ions with charge state numbers greater than 1 and on the impact of the spectrometers settings on the signal intensity [106,107]. Therefore the main objectives of this section are (i) to give the necessary theoretical background of the functioning of the spectrometer to enable the correct interpretation of the energy spectra, especially of those of higher charge-state ions, (ii) to provide the procedure of tuning the spectrometer and (iii) to provide a procedure of ion energy spectra acquisition and interpretation.

4.1.1 Spectrometer structure and functioning

As depicted in Fig. 4.1 (p. 22), Hiden EQP 300 mass spectrometer system comprises of (i) the differentially pumped probe (hereafter called the 'spectrometer') equipped with a removable radio frequency head ('RF Head') and an electrostatic analyzer head ('ESA Head'), (ii) the mass spectrometer interface unit (MSIU) and (iii) the control PC. The ion optics, energy filter, mass filter and detector are located in the spectrometer whereas the voltage sources for particular spectrometer electrodes are inbuilt in the MSIU. Each measurement procedure is programmed using 'Hiden Mass Soft' application program and subsequently loaded in the MSIU, which controls the scan. The data measured are continuously transmitted to the PC during the scan. Hereafter, the spectrometer's functioning is described since the setup of this part of the EQP 300 system directly influences the measured data and its interpretation.

The design of the spectrometer is outlined in Fig. 4.2 (p. 23). Starting from the left, the spectrometer comprises: (i) extraction section, (ii) ionization source, (iii) drift tube, (iv) energy filter, (v) mass filter and (vi) detector. In the text, the voltage supplies are designated in the same way as the corresponding output voltages, i.e. starting with upper case letter and marked by single quotation marks. For example, the term 'Energy' denotes the particular value of the voltage or the voltage supply itself. In the 'secondary ion mass spectroscopy' mode (SIMS, the term 'secondary' is used to emphasize the fact that the ions are formed outside the spectrometer, as opposed to the RGA mode described below) ions enter the spectrometer via orifice (100 µm diameter hole was used) in the extraction section and are focused by 'Lens1', 'Lens2' and

quadrupole lens (‘Vert’, ‘Horiz’ and ‘D.C.Quad’) prior to entering the electrostatic energy filter. Only the ions with kinetic energies within a specific energy range are allowed to pass through the filter. Further focus is done by the ‘Focus2’ lens. Then, the time-varying voltages applied on the electrodes of quadrupole mass filter define the range of the mass-to-charge ratio (m/q) of ions which go through it and hit the conversion electrode where electrons are emitted as a result of the ion impact. The energy of the ions striking the conversion electrode is set by the ‘1st Dynode’ voltage. Finally, electron signal is magnified in the multiplier and detected. In the ‘residual gas analysis’ mode (RGA), neutral particles are ionized in the spectrometer’s internal ionization source after entering the spectrometer. Their succeeding trajectory is the same as in the SIMS mode. All the spectrometer’s lenses are electrostatic.

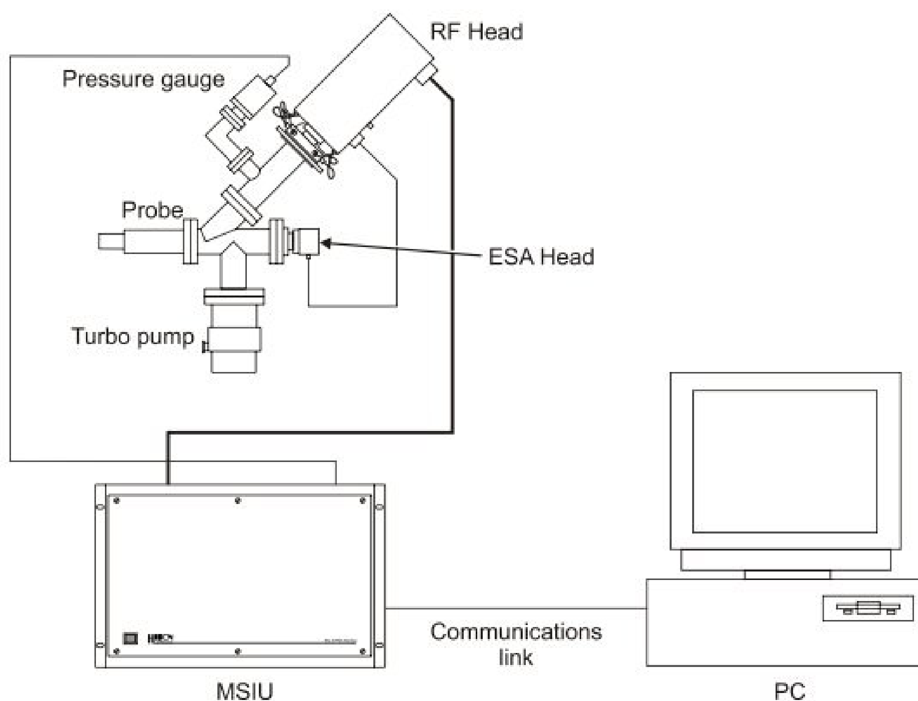

Fig. 4.1
Schematics of the entire EQP 300 mass spectrometer system. Spectrometer is differentially pumped and has a separate Penning pressure gauge mounted in the vicinity of the detector in order to prevent the detector's damage by overpressure. The spectrometer is controlled by the mass spectrometer interface unit (MSIU) where all the voltage sources are located. MSIU governs the scan sequence and communicates with the control PC where the ‘Mass Soft’ application program is installed. Adapted from [106].

To achieve the correct function of the spectrometer, it is essential to avoid collisional scattering of ions inside it. On that account, the spectrometer is differentially pumped by a turbomolecular pump (TMP) and the diameter of the spectrometer extraction orifice is limited depending on the pressure outside the spectrometer apparatus. Besides, a high pressure in the detector section can result in a damage of the

detector, so the pressure in the detector vicinity is monitored by the Penning gauge to switch off the detector when the pressure attains a critical level.

Under the conditions of high thermal loadings of the extraction orifice and its exposition to dense plasmas it is unavoidable to protect it, e.g. by means of protective screens or apertures. In Sec. 4.1.5 (p. 35) theoretical considerations regarding this issue are discussed; in Sec. 4.3.2 (p. 49), the particular technical solution is described and depicted in Fig. 4.17 (p. 47) and Fig. 4.18 (p. 48).

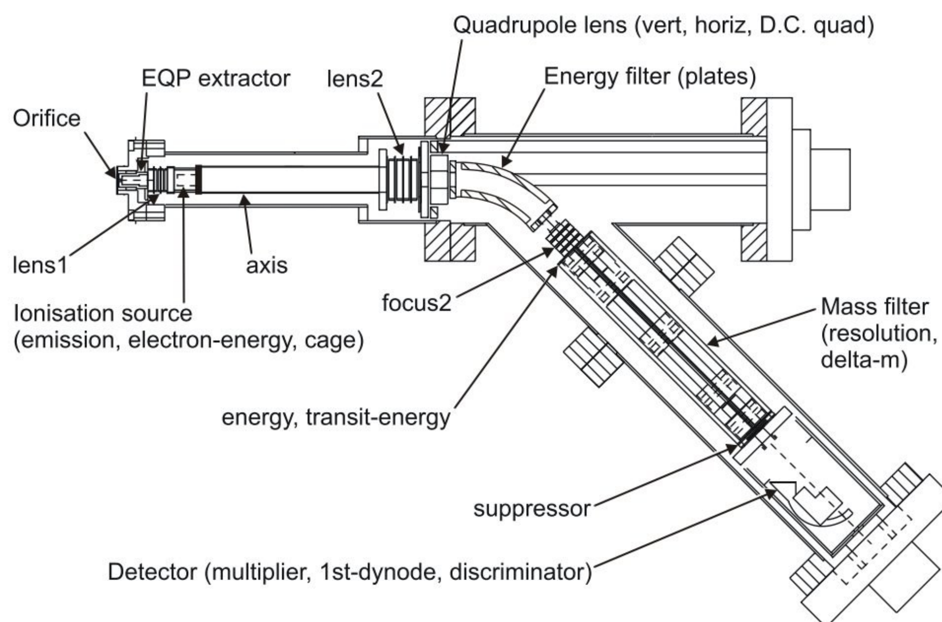

Fig. 4.2

Schematics of the mass spectrometer. Starting from the left side, the spectrometer comprises: (i) extraction section, (ii) ionization source, (iii) drift tube, (iv) energy filter, (v) mass filter and (vi) detector. All ion-guiding elements are electrostatic: extraction electrode (‘Extractor’), focusing lenses (‘Lens1’, ‘Lens2’, ‘Vert’, ‘Horiz’, ‘D.C.Quad’ and ‘Focus2’), electrodes governing the velocity of the ions in the spectrometer (‘Axis’, ‘Energy’ and ‘Transit-energy’) energy filter electrodes (‘Plates’), mass-filter electrodes and detector electrodes (‘Suppressor’, ‘Multiplier, ‘1stDynode’ and ‘Discriminator’). Adapted from [106].

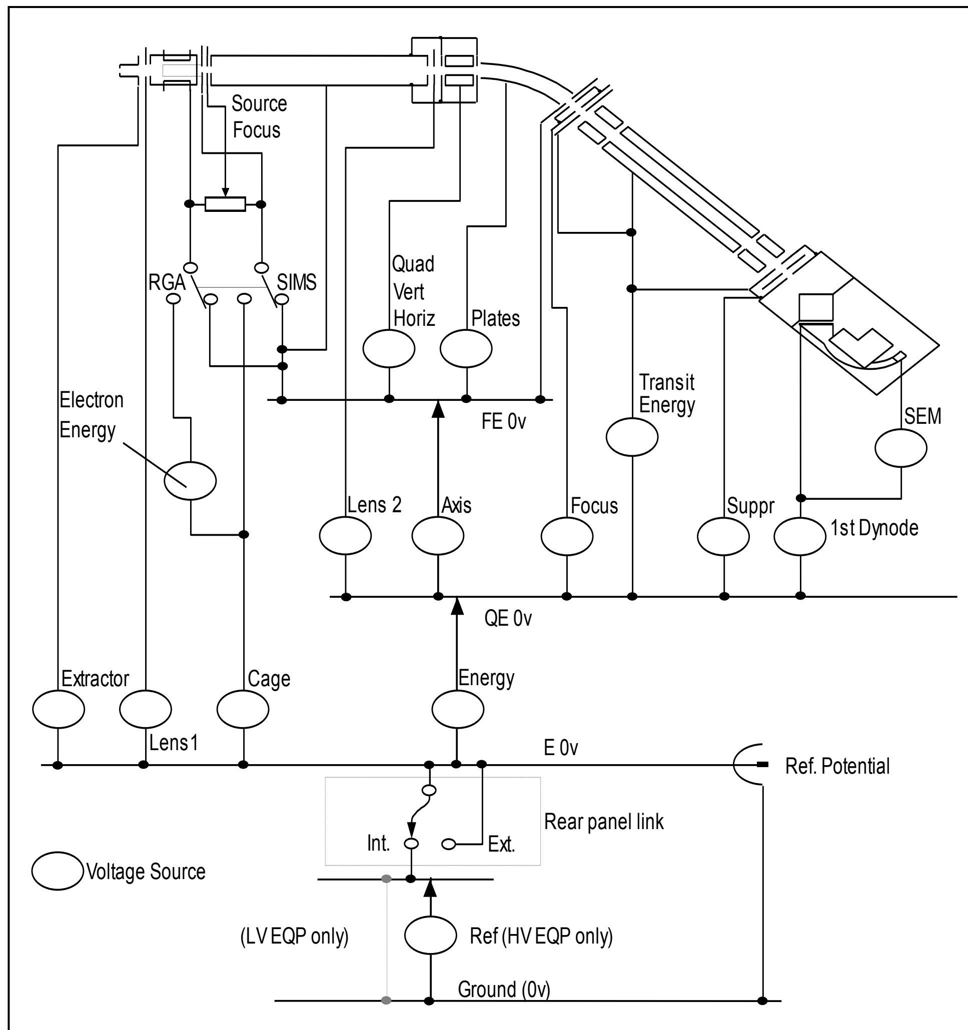

Fig. 4.3

Spectrometer circuitry diagram. Lens electrodes ('Lens1', 'Lens2', 'D.C.quad.'[marked as 'Quad' in the drawing], 'Vert.', 'Horiz.', 'Focus2' [marked as 'Focus']) master the focusing of the ion beam. When the spectrometer is operated in the SIMS mode, the 'Extractor' voltage source defines the potential used to extract the ions from the plasma. 'Axis' and 'Plates' electrodes are coupled in order to allow the ions with the kinetic energy equal to the absolute value of the potential of the 'Axis' electrode to pass through the energy filter, see Eq. 4.5 (p. 26). The 'Energy' electrode adjusts the actual kinetic energy of the ions, see. Eq. 4.2 (p. 25). 'Transit-energy' is a virtual source, meaning that the energy of the ions passing through the mass filter is controlled by other electrodes. The detector section is operated by the 'Suppressor', '1stDynode' and 'Multiplier' (marked as 'SEM') sources. In the RGA mode, the ion source is biased to 'Cage' potential and the energy of electrons ionizing the neutral particles is set by 'Electron-energy'. The entire spectrometer can be biased to a desired potential either by making use of the internal 'Reference' (marked as 'Ref') voltage source or by applying an additional voltage source marked as 'Ref. Potential'. Adapted from [106].

4.1.2 Spectrometer functioning in detail

In order to correctly operate the spectrometer it is crucial to fully understand the purpose of particular electrodes and how these influence the direction and the kinetic and potential energies of the ions within the instrument. The spectrometer circuitry diagram is delineated in Fig. 4.3 (p. 24). The explanation of the spectrometer's functioning given is based on clarifying the impact of particular electrodes on the kinetic and potential energies of the positively charged ion extracted from the outside of the spectrometer on its route from the orifice towards the detector. In the following, all the potential energies are relative to the ground potential, i.e. to the potential of grounded chamber walls.

Prior to a detailed description of the functioning of specific components of the spectrometer, it is essential to mention the general behavior of the spectrometer system: (i) All the voltages applied on particular electrodes are set for a certain period of time and are not altered within this time interval. This time span is specified by the 'Dwell time' parameter. (ii) The outputs of all the voltage supplies are changed in steps. The values of the differences between the steps are specific for each supply.

Let the kinetic energy of an ion in the plasma be ε_{pl} and its potential energy (with respect to the ground potential) be equal to the plasma potential, φ_{pl}. In the SIMS mode, the ion is extracted from the plasma region by applying a negative potential on the extractor electrode resulting in the kinetic energy of the ion entering the spectrometer equal to

$$\varepsilon_{extractor} = \varepsilon_{pl} + ne(\varphi_{pl} - \text{'Extractor'}) \quad , \tag{4.1}$$

where n is the charge state of the ion and e, e > 0, stands for the elementary charge. After that, the ion is directed by the 'Lens1' electrostatic lens into the drift tube. The drift tube is biased with respect to the ground potential by the voltage supplies 'Energy' and 'Axis', which results in the kinetic energy of the ion in the drift tube and energy filter regions

$$\varepsilon_{enFil} = \varepsilon_{pl} + ne(\varphi_{pl} - \text{'Energy'} - \text{'Axis'}) \quad . \tag{4.2}$$

Successive direction of the ion into the 45° sector field energy analyser (energy filter) is performed by the 'Lens2', 'Vert', 'Horiz' and 'D.C.Quad' lenses.

The energy filter consists of two parallel electrically biased plates which together with the apertures located at the entrance to the energy filter and between the energy filter and the mass filter allow only the ions with specific kinetic energies to pass through. The potentials on the plates are applied via the 'Plates' supply. Considering the balance between centrifugal (inertia) and centripetal (electrostatic) forces acting on the particle moving on the axis of the energy filter, we find

$$\frac{m(v_{axial})^2}{R} = \frac{2\varepsilon_{axial}}{R} = ne|E| \approx ne\frac{\text{'Plates'}}{d} \quad , \tag{4.3}$$

where m denotes the mass of the ion, v_{axial} is the velocity of the ion moving on a circular trajectory of the radius equal to the mean radius of the energy filter, R. Apparently, the kinetic energy of the ion passing through the filter, ε_{axial}, is directly proportional to the magnitude of the electric field intensity, $|\mathbf{E}|$, on the axis of the energy filter. $|\mathbf{E}|$ is approximately equal to the ratio of the difference of electrostatic potentials between the plates (driven by 'Plates' supply) and the distance, d, between them. Only the ions with kinetic energies close to ε_{axial} pass through the energy filter and succeeding apertures. Putting $\varepsilon_{enFil} = \varepsilon_{axial}$ and combining Eq. 4.2 and Eq. 4.3 results in

$$\varepsilon_{pl} + ne\varphi_{pl} = ne\left(\text{'Energy'} + \text{'Axis'} + \frac{R\,\text{'Plates'}}{2d}\right) . \qquad (4.4)$$

It is convenient to set the sum of the last two terms in the Eq. 4.4 equal to zero.

$$\frac{R\,\text{'Plates'}}{2d} = -\text{'Axis'} = \frac{\varepsilon_{axial}}{ne} . \qquad (4.5)$$

This setting allows us to determine the sum of the kinetic and potential energy of the detected ion to be calculated using the value of the 'Energy' voltage since

$$\varepsilon_{pl} + ne\varphi_{pl} = +ne\,\text{'Energy'} . \qquad (4.6)$$

The ions with energies close to ε_{axial} pass through the aperture located at the end of the energy filter which sets the energy resolution of the filter. At the exit from the energy filter, the ion is directed into the entrance of the mass filter by a series of lenses (driven by 'Focus' supply) and the kinetic energy of the ion is equal to the nominal value of the 'Transit-energy' voltage (The ion is leaving the section biased by 'Axis' with the kinetic energy – in the units of eV – equal to the absolute value of 'Axis'). To be precise, the 'Transit-energy' supply does not really exist in the spectrometer's hardware and is established making use of the other electrodes, which implies that the identities in the Eq. 4.5 are not exact. However, this deviation is compensated by the operating software and from the operator's point of view the spectrometer circuitry diagram is functionally the one presented in Fig. 4.3 (p. 24).

After undergoing energy-filtering and focusing, the ions enter the triple-selection quadrupole mass filter which allows only the ions with the specific mass-to-charge ratio to fly through and enter the detector section. Then, secondary electrons are emitted as a result of the ion impact onto the conversion electrode biased by the '1st Dynode' supply and the electron signal is magnified via a Channeltron detector to be detected. Note that the secondary electron emission yield from the conversion electrode is dependent also on the kinetic energy of the impacting ion. So the sensitivity of the detector is strongly affected by the '1st Dynode' voltage and by the charge state of the impacting ion.

In the RGA mode, the ion path starts in the internal ionization source of the spectrometer which is close to the extraction section and biased by the 'Cage' voltage supply. Here, neutral particles are ionized via electron impact. Then, their trajectory is the same as in the SIMS mode and these are detected with energies corresponding to the 'Cage' potential.

From the analysis given above, it follows that the ion charge state must be taken into consideration (i) when the kinetic energy of the ion is evaluated, see Eq. 4.6, (ii) when the resolution of the mass filter is assessed since the time-of-flight of the ion through the mass filter is determined by its kinetic energy, which is given by the 'Transit-energy' voltage together with the charge state of the ion and (iii) as the '1st Dynode' voltage is set since the detector's sensitivity depends also on the kinetic energy of the impacting ion.

4.1.3 Sensitivity of the spectrometer

In Sec. 4.1.2 (p. 25), the flight of an ion through the spectrometer was analyzed. For the sake of clarity, the ion's exact values of the kinetic energy and the mass-to-charge ratio were assumed. In reality, the spectrometer detects the ions whose kinetic energy and mass-to-charge ratios are within intervals of values. Therefore, it is desirable to understand how the spread in the kinetic energy and in the mass-to-charge ratio is influenced by the properties of the particular ionic species and by the settings of the spectrometer. In addition to this, some of the ions are not detected at all due to the arrangement of the spectrometer's extraction section and due to the limitations of the detector. Generally, the ratio of the spectrometer's output signal to the magnitude of the flux of ions onto the extractor's orifice is determined by (i) the directionality of the flux of the respective ions, (ii) the properties of the extraction system, (iii) the energy filter, (iv) the electrostatic lenses, (v) the mass filter and (v) the detector [107,108].

Extraction system – acceptance angle

Considering the ions with high kinetic energies striking the extractor at high angles of incidence, we observe that the extractor is not capable of directing these ions into the instrument. This phenomenon is quantified by the so called 'acceptance angle', meaning that the ions with specific kinetic energy are directed into the spectrometer only if the angle of incidence of these ions is less or equal to a particular value. Graphically, the acceptance angle for the Hiden EQP 300 spectrometer is captured in Fig. 4.4 (p. 28). Note that the acceptance angle data in Fig. 4.4 (p. 28) are derived from SIMION simulation software calculations on the ion transport system, and not from experimental data. The real situation is much more complicated due to the presence of the electric field in the sheath region formed between the plasma space and the extraction orifice and due to the collisions of the ions with other plasma species.

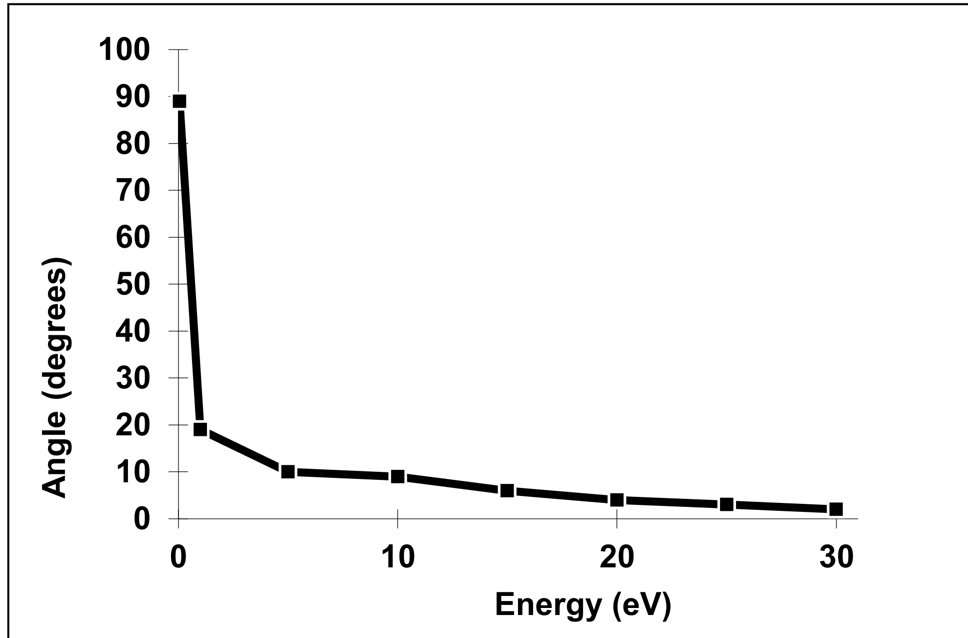

Fig. 4.4
Probe acceptance angle. The acceptance angle data is derived from SIMION simulation software calculations on the ion transport system, and not from experimental data. Data taken from [107].

Energy filter – resolution

As follows from the description of the energy filter functioning in Sec. 4.1.2 (p. 25), the ions with energies $\varepsilon_{axial} \approx neR'Plates'/2d = -ne'Axis'$, see Eq. 4.5 (p. 26), pass through the energy filter on the trajectory coincident with the axis of the filter (for the sake of simplicity, we neglect the ions entering the filter in oblique directions). If an ion with the energy $\varepsilon = \varepsilon_{axial} + \Delta\varepsilon$ enters the filter, its trajectory differs from that of the ion with the energy ε_{axial}. The task is to evaluate the position of this ion at the filter's exit in order to decide whether this ion passes through the filter's exit aperture or not. For a sector energy analyser, the energy resolution is given by [107]:

$$\Delta\varepsilon = \frac{w\,\varepsilon_{axial}}{R(1-\cos\phi)+L\sin\phi} = \frac{w\,ne'Axis'}{R(1-\cos\phi)+L\sin\phi} \quad , \qquad (4.7)$$

where w is the filter's aperture diameter, ϕ is the sector angle and L stands for the distance between the end of the filter's electrodes and the aperture. To be precise, the filter has two apertures, both of the same diameter, one located at the entrance and the second one at the exit. For the particular case of EQP 300

spectrometer, $w = 3$ mm, $\phi = 45°$, $R = 75$ mm and the in $L = 35.4$ mm which gives $\Delta\varepsilon \approx 2.5$ eV for singly charged ion and 'Axis' voltage equal to 40 V. Note that the energy resolution is dependent on the charge state number of an ion and independent of its mass-to-charge ratio.

Mass discrimination

As follows from the analysis of the Lorentz force law, trajectories of the ions in the electrostatic fields are independent of the mass-to-charge ratio [109]. But this is not the case for the quadrupole mass filter since its electrodes are driven by an RF voltage source. In order to determine the mass discrimination of the instrument, the response of the system was evaluated using different chemical compounds and the results are presented in Fig. 4.5 (p. 29) [107]. The mass discrimination must be taken into account when the data on the composition of the ion flux are to be interpreted.

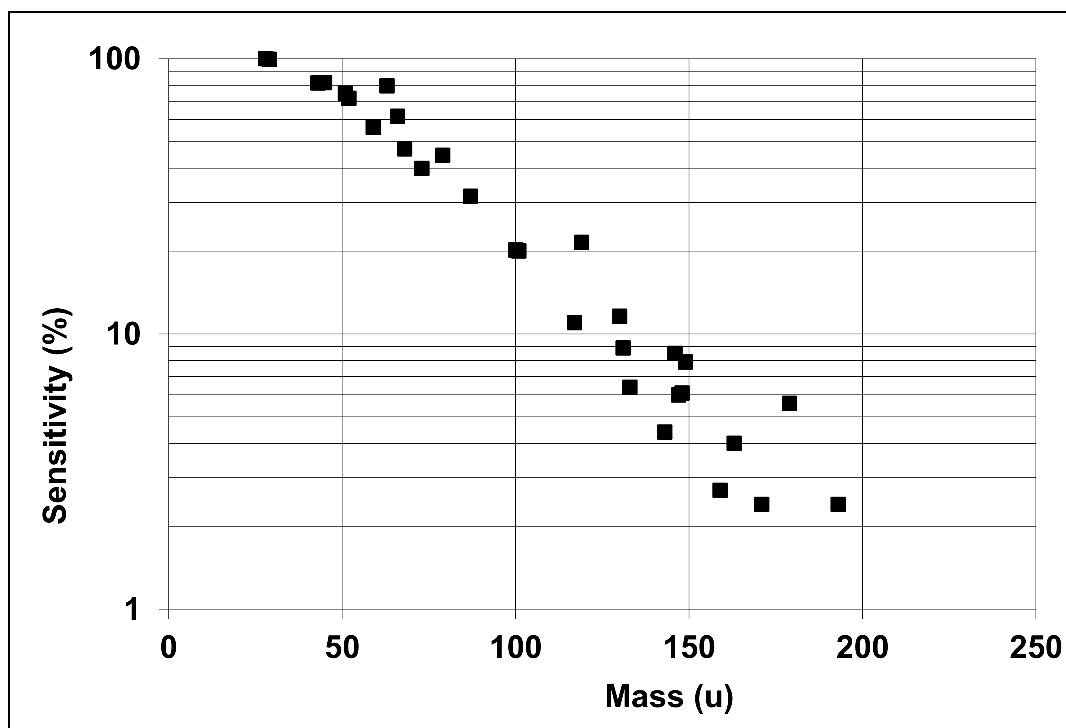

Fig. 4.5
Mass discrimination of the spectrometer. The figure shows the response of the analyser and the detector. Mass of 28 AMU is given a value of 100%. Data taken from [107].

Sensitivity of the detector

The spectrometer system is equipped with the ion counting Channeltron detector. There is also the option to install the Faraday cup detector, but the following description will concern the first one.

As the ion strikes the conversion electrode, biased by '1stDynode', secondary electrons are emitted from the electrode's surface. Subsequently, the secondary electrons are extracted towards the multiplier by a strong positive electric potential applied to the multiplier's electrodes. The overall bias of the multiplier's electrodes is controlled by the 'Multiplier' source. Inside the multiplier, the signal of the electrons is magnified by accelerating the electrons towards the electrodes which are progressively positively biased with respect to one another. The electrons (called 'primaries') hitting the particular electrode (i) are partially reflected, (ii) are partially absorbed and (iii) cause the emission of secondary electrons ('secondaries') from that electrode. Reflected primaries and emitted secondaries are pushed towards the next electrode giving rise to an 'avalanche' of electrons. Finally, the avalanche is detected by the control electronics.

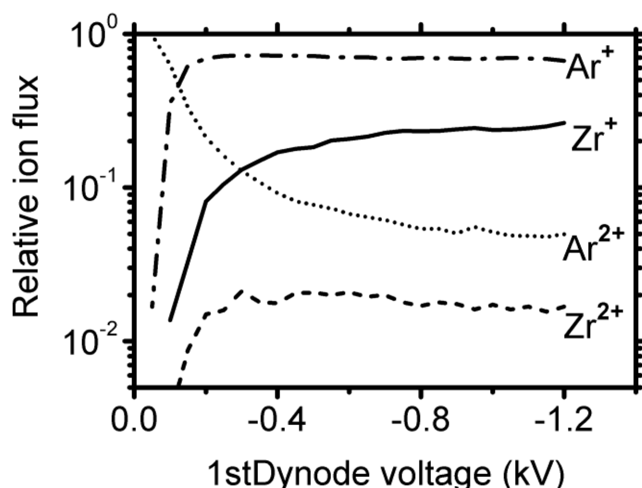

Fig. 4.6
Setting the adequate '1stDynode' voltage. The voltage should be high enough to cause the kinetic emission of electrons from the conversion electrode to prevail over the potential emission, see the high relative value of the signal of Ar^{2+} ions at low '1stDynode' voltages caused by their high ionization potential. Energy resolution and mass discrimination were not considered.
Experimental conditions: Pulsed DC discharge, discharge voltage U_d = 380 V, repetition frequency f_r = 500 Hz, pulse duration t_1 = 200 μs, Ar process-gas pressure p = 2 Pa, target power density $\overline{S}_d$ = 3.8 Wcm^{-2}.

The number of ions detected per time interval is limited, since the time of one detection cycle is not negligible and some ions may hit the conversion electrode while the electron avalanche triggered by the hit of preceding ion(s) is still being developed. Therefore the signal intensity should not exceed 5×10^6 counts per second (cs^{-1}).

To keep the signal intensity proportional to the number of ions striking the conversion electrode, a sufficient number of secondary electrons must be emitted per each ion impacting the conversion electrode in order to invoke the electron avalanche in the multiplier. The average number of secondary electrons emitted from the surface per one impacting ion, i.e. secondary emission yield, is primarily dependent on the ion's kinetic energy and ionization potential. Since the ionization potential of different

ionic species varies strongly, it is feasible to control the secondary emission yield via the kinetic energy of an impacting ion. That is why the '1st dynode' potential should be set high enough to favor the kinetic emission over the potential one and thus to make the detector signal independent of the properties of the particular ionic species. The effect of the potential emission is illustrated in Fig. 4.6 (p. 30). The ionization potential of Ar^{2+} ions (27.63 eV) prevails over those of AR^{1+} (15.76 eV), Zr^{2+} (13.16 eV) and Zr^{1+} (6.63 eV) causing the signal of Ar^{2+} to be significantly stronger than the signal of other ions present in the flux onto the conversion electrode. As the '1st dynode' bias rises, the kinetic emission of secondary electrons prevails over the potential one. So, the '1stDynode' must be set high enough to eliminate higher kinetic energies and thus higher secondary electron emission yields of higher-charge-state ions since these are accelerated by the same voltage applied on the '1stDynode'.

4.1.4 Tuning the spectrometer

The general aim of the tuning procedure is to set the potential of the spectrometer electrodes in such a way that the maximum number of the ions entering the system reach the detector. Clearly, a change in the electric potential of each particular electrode requires an adjustment of the potential of other electrodes since these are adjusted to each other. Because the spectrometer is operated under different conditions, it is necessary to adjust the setting of the electrodes to gain the optimum signal. Generally, the need for tuning the spectrometer stems from the changes in (i) the plasma properties in the extractor region, e.g. plasma potential, plasma density, directionality of the ionic flux and the energy distribution functions of the ions to be measured, (ii) the setup of the spectrometer's extraction system, i.e. the geometry of shielding and extraction electrodes together with the electric bias applied on them, (iii) the contamination of the spectrometer caused by the material being deposited on the extractor and also on the electrodes inside the spectrometer, (iv) stray magnetic fields influencing the paths of the particles in the spectrometer and (v) the instabilities of the spectrometer itself, i.e. shifts in the properties of voltage sources etc. Note that the presented tuning procedure is optimized in order to measure the ion energy spectra (IESs) of selected ionic species.

As mentioned in Sec. 4.1.2 (p. 25) and Sec. 4.1.3 (p. 27), the trajectory of an ion through the detector is dependent on the kinetic energy of the ion. However, it would be too time demanding to find the optimum settings for each value of energy of the ion species. It is more suitable to find the value of ion energy at which the ion energy spectrum exhibits its maximum and then to tune the electrodes to accommodate to the ions with this energy. A shift in ion energy spectra as a result of different setting of a particular electrode is illustrated in Fig. 4.7 (p. 32). As the voltage applied on the 'Lens1' electrode decreases, the maximum of the IES drops and, at the same time, the signal of ions with high kinetic energies rises, i.e. the transmission of the ions with high kinetic energies through the spectrometer may increase when the settings of some of the electrodes does not correspond to the settings optimal for lower kinetic energies. The effect of the 'Lens1' electrode on the shape of the IES is thought to be general because it was observed under various discharge conditions and for different ion species, as shown in two graphs in Fig. 4.7 (p. 32).

Previously, see Sec. 4.1.2 (p. 25) and Sec. 4.1.3 (p. 27), it was claimed that the trajectory of an ion in an electrostatic field is independent of the mass-to-charge ratio of the ion. Practically, this fact can be used in the tuning procedure since the shape of the IES does not differ significantly when different ions are used for tuning the spectrometer. As illustrated in Fig. 4.8 (p. 33), tuning the spectrometer with respect to the maximum of IES of $^{40}Ar^{+}$ or $^{90}Zr^{+}$ ion has almost no impact on the IES of both of the ionic species since the respective IESs exhibit their maxima at almost the same energies.

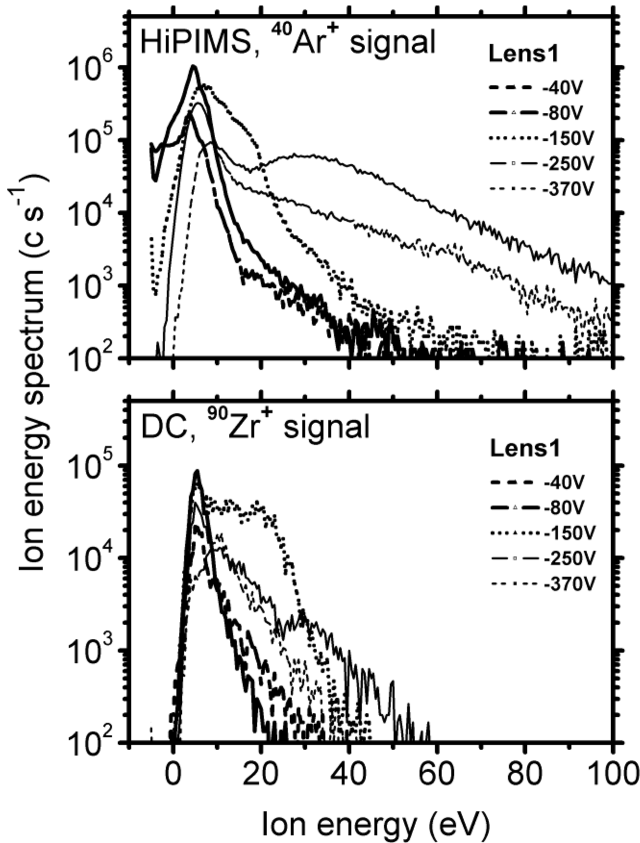

Fig. 4.7
Sensitivity of the ion energy spectra (IES) to the 'Lens1' potential. Changing the 'Lens1' potential to more negative values causes (i) ions with high kinetic energies to be preferred in the spectra and (ii) value of the maxima in the IES to be lowered. This effect was observed under different discharge conditions for different ionic species:
(a) $^{40}Ar^{+}$ ion IES. Pulsed DC discharge, discharge voltage U_d = 600 V, repetition frequency f_r = 500 Hz, pulse duration t_1 = 200 µs, average target power density $\overline{S}_d$ = 50 Wcm^{-2}, argon process-gas pressure p = 2 Pa, oxygen flow rate Q = 4 sccm,
(b) $^{90}Zr^{+}$ ion IES. DC discharge, U_d = 400 V, discharge current $\overline{I}_d$ = 1 A, $\overline{S}_d$ = 5 Wcm^{-2}, argon process-gas pressure p = 0.5 Pa.

Tuning of a particular electrode is carried out by changing the voltage applied on it (i.e. 'scanning' the electrode) and finding the value at which the output signal exhibits its maximum. This can be done manually or via an automatic user-defined procedure. For the correct function of the automated tuning procedure it is necessary to suppress the noise in the output signal. Otherwise the maximum in the signal may not correspond to the optimum settings of the electrode voltage. So the time of the acquisition of one sample of the signal (called the 'Dwell time') should be sufficiently long and the ion flux from the plasma should be stable (e.g. discharge should be free from arcing).

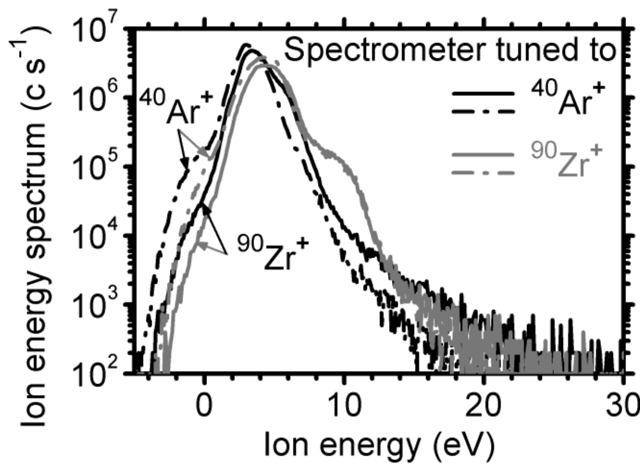

Fig. 4.8
Sensitivity of measured ion energy spectra (IES) to the mass-to-charge ratio of the ion used for the spectrometer tuning. Tuning the spectrometer with respect to the maximum signal of $^{40}Ar^+$ ion (black lines) or $^{90}Zr^+$ signal (grey lines) has minor impact on the IES of the respective ions: $^{40}Ar^+$ (dash-dotted lines) and $^{90}Zr^+$ (full lines).
Experimental conditions: Pulsed DC discharge, discharge voltage U_d = 380 V, repetition frequency f_r = 500 Hz, pulse duration t_1 = 200 µs , average target power density $\overline{S}_d$ = 3.8 Wcm^{-2}, argon process-gas pressure p = 2 Pa.

Based on the experience and on the instructions in user manual [106], the tuning strategy in different spectrometer modes is proposed as follows:

Positive ion SIMS mode

(1) Set the ‘Extractor’ bias to a value of a few volts below the plasma potential in the extractor vicinity to attract the ions and repel the electrons (i.e., to avoid the extractor overheating by the electron current drawn from the plasma). The bias should be small enough to prevent an additional ionization in the extractor’s vicinity caused by secondary electrons emitted from the extractor’s surface.

(2) Set the mass-to-charge ratio of the ionic species to be scanned.

(3) Set the voltages in the detector section to values recommended in the user manual [106]. Make sure that the ‘1st Dynode’ voltage is sufficient, i.e. the further increase in the magnitude of ‘1st Dynode’ has no impact on the ion flux composition, see Sec. 4.1.3 (p. 27).

(4) Scan the ‘Energy’ electrode to find the energy at which the ion energy spectrum exhibits its maximum.

(5) Scan the electrodes in the sequence that reflects the flight of the ions through the spectrometer. The tuning sequence is: ‘Lens1’, ‘Source Focus’ (if present), ‘Lens2’, ‘Horiz’, ‘Vert’, ’D.C.Quad’, ‘Focus2’. Perform the scan several times and identify (i) the electrodes that influence the output signal the most and (ii) the range of voltages in which the signal exhibits significant variations.

(6) Scan the following electrodes for the maximum signal several times: the ‘Energy’ electrode and then the electrodes identified in step (5) as having major influence on the output signal. Scans are performed in the same sequence as in step (5).

(7) Scan the electrodes identified in step (5) as having marginal influence on the output signal for maximum signal one time. Scans are performed in the same sequence as in step (5).

(8) Repeat the sequence from the step (6) until the tuned values and signal intensity do not vary significantly.

Negative ion SIMS mode

The tuning procedure is analogous to the tuning in the positive SIMS mode. In step (1) it is necessary to determine the appropriate value of the 'Extractor' bias, since as mentioned before, positive bias could result in overheating of extractor due to the high electron currents drawn from the plasma.

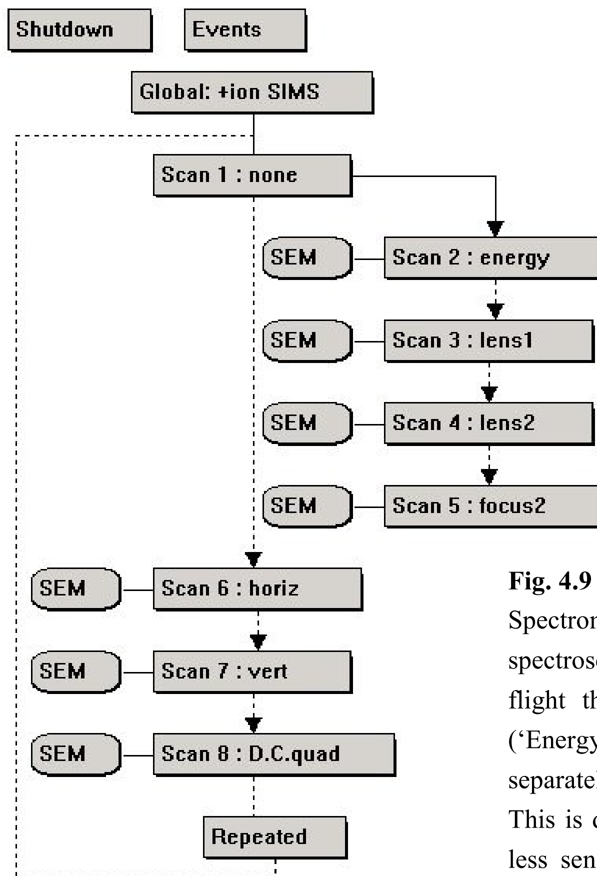

Fig. 4.9
Spectrometer tuning procedure in the secondary ion mass spectroscopy (SIMS) mode. The tuning sequence reflects the ion flight through the spectrometer. The most critical elements ('Energy', 'Lens1', 'Lens2' and 'Focus2') are adjusted separately in several cycles at the beginning of the tuning loop. This is done via the "dummy" 'None' initial branch. Then, the less sensitive electrodes ('Horiz', 'Vert' and 'D.C.Quad') are scanned. The entire tuning loop is repeated several times.

RGA mode

The tuning strategy in the RGA mode is analogous to the tuning in the SIMS mode. The differences are: (i) In step (1) the parameters of the ionization source (i.e., the energy of electrons that cause the electron impact ionization – set by the 'Electron-energy' bias – and the magnitude of the ionization current – set by the 'Filament' parameter) are to be set instead of 'Extractor' bias which has marginal influence on the spectra in RGA mode. (ii) In step (5) the 'Cage' electrode is scanned instead of the 'Lens1' electrode.

In Fig. 4.9 (p. 34), an automatic tuning procedure is presented, illustrating steps (4) – (8) as described in preceding paragraphs. The electrodes 'Lens1, 'Lens2' and 'Focus2' were identified to have major influence on the signal intensity, see step (5), and thus they are scanned for the maximum signal several times using the "dummy" 'None' branch. After that, the 'Horiz', 'Vert' and 'D.C.Quad' electrodes are scanned one time and the entire tuning loop is repeated.

4.1.5 Spectra acquisition

Some of the key practical issues regarding the spectra acquisition are not summarized in one concise operating instruction or are missing in the operator's manual at all. Therefore, the objective of this section is to provide an overview of the main topics related to the correct operation of the spectrometer. Unless otherwise specified, the procedures described in this section are applicable both to the time-averaged and to the time-resolved scans.

First, a proper protection of the spectrometer from the power flux coming from the plasma must be ensured. Namely in the conditions of high target power loadings and short extractor-to-target distances the extractor should be screened by additional shielding in order to prevent an overheating and a consequent deformation of the extraction orifice. It is recommended to shield the extractor using several electrodes with circular holes that do not impede the flux of the ions into the extraction orifice. The electrodes may be grounded, biased or operated at a floating potential. For details of the solution used see Fig. 4.18 (p. 48) and Fig. 4.17 (p. 47). Then, the grounding of the spectrometer itself must be ensured to allow for the correct interpretation of the energy of the ions detected by the spectrometer, see Sec. 4.1.2 (p. 25).

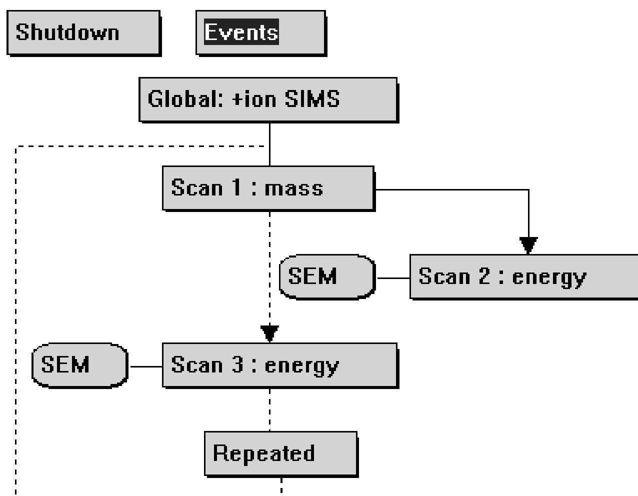

Fig. 4.10
Scan procedure employed to perform the scan over a specific range of ion mass-to-charge ratios of positive ions in the secondary ion mass spectroscopy (SIMS) mode. This routine is to be used when the contamination of the system is investigated. The same scan structure is employed in the residual gas analysis (RGA) mode when the composition of the chamber atmosphere is explored.

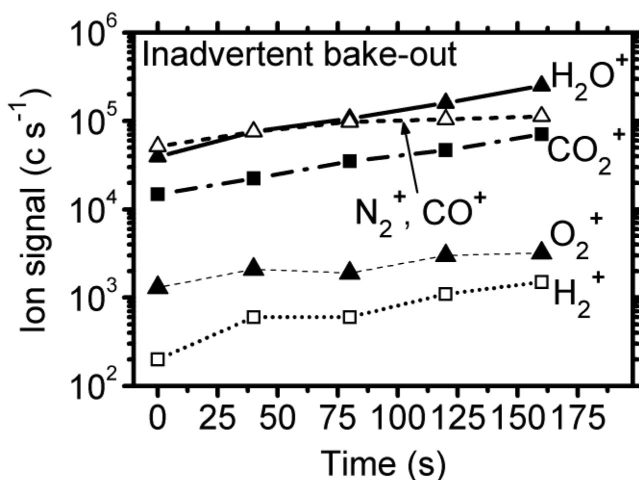

Fig. 4.11
Inadvertent bake-out of the spectrometer's interior. The operation of the spectrometer's internal ionization source causes rise in the temperature of the ionization section. The signal of the major contaminants is increased several times. In most cases, water was identified as the main contaminant of the spectrometer's interior. The signal is integrated over the 'Energy' scan ranging from -0.5 V to 4.0 V
Experimental Conditions: Ionization current set by 'Emission' = 2×200 µA (both filaments are operated), energy of electrons emitted from the filaments (set by 'Electron-energy' supply) = 70 V, no process gas in the chamber.

Before measurements of ion fluxes from the plasma, it is necessary to make sure that the contamination originating (i) from the chamber surfaces and (ii) from the spectrometer itself does not significantly influence the measured spectra. The first kind is usually diminished since the sputtered material is often very reactive causing the contaminants to be chemisorbed at the chamber walls. The gases chemisorbed on the surfaces inside the spectrometer should be removed by baking out the spectrometer. This is performed by applying external heating by a resistance wire and via internal heating located in the spectrometer's ionization section utilizing electron emitting filaments. As demonstrated in Fig. 4.11 (p. 36), as the temperature rises in the ionization section, the signal of the major contaminants increases several times. Water was identified as the main contaminant of the spectrometer's interior. It may enter the plasma space when the spectrometer is heated up during the measurement, cause the contamination of the deposition system and, consequently, lead to the generation of several ionic species (H_2O^+, H^+, H_2^+, H_3^+, ArH^+ etc.) which are detected by the spectrometer.

After the spectrometer is baked out, it is useful to roughly tune the spectrometer and to measure the composition of the working atmosphere with no plasma present and also when the discharge is on, i.e. to perform the RGA and SIMS scans, both over wide range of mass-to-charge ratio. As mentioned in Sec. 4.1.4 (p. 31), it is necessary to set an appropriate bias of the extraction electrode. High extraction voltages would result in an additional ionization of the plasma species in the vicinity of the extractor by secondary electrons that are emitted from the extractor surface. For that reason, the potential of the 'Extractor' is recommended to be a just few volts lower than the plasma potential.

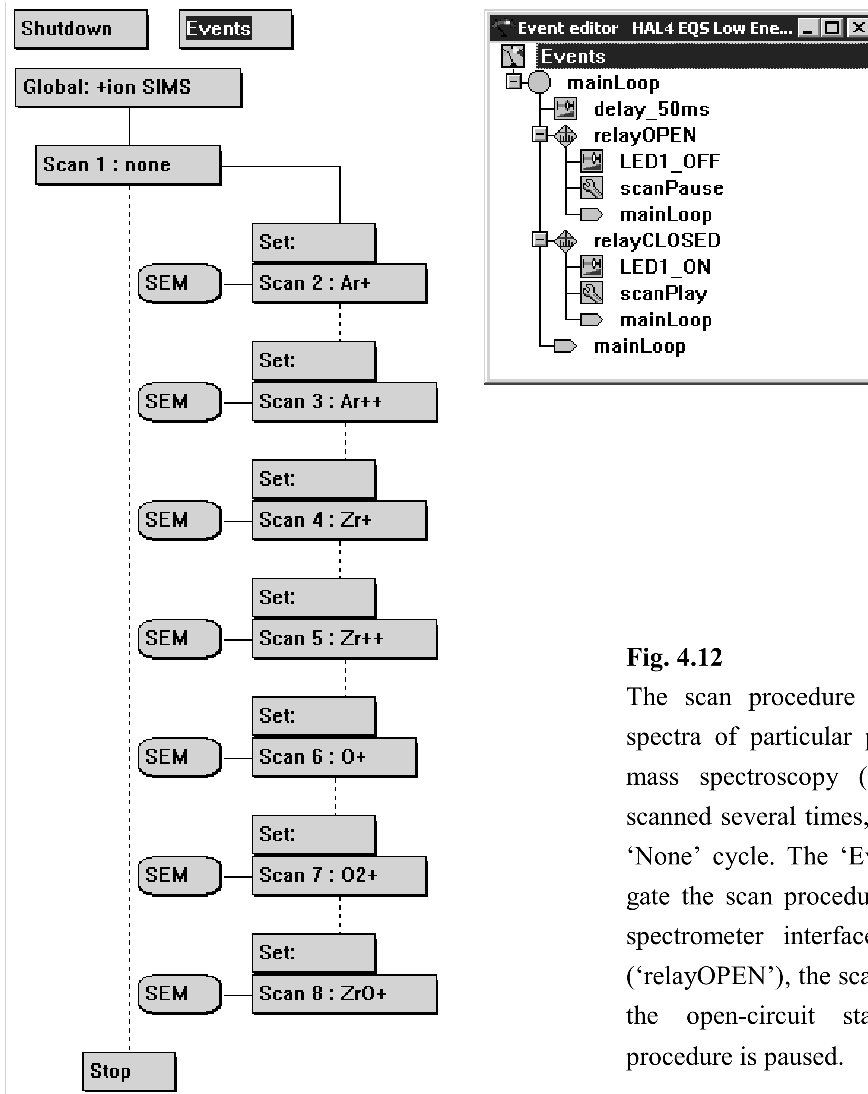

Fig. 4.12
The scan procedure used to measure the ion energy spectra of particular positive ions in the secondary ion mass spectroscopy (SIMS) mode. Each spectrum is scanned several times, which is ensured by the "dummy" 'None' cycle. The 'Events' feature is used to externally gate the scan procedure. As the relay input of the mass spectrometer interface unit (MSIU) is short-circuited ('relayOPEN'), the scan is running and once it switches to the open-circuit state ('relayCLOSED'), the scan procedure is paused.

As shown in Fig. 4.13 (p. 38), the contamination which is independent of the process-gas used is found in the system. Employing the RGA scan (Fig. 4.10 [p. 35]) can help us reveal chamber leakages and leakages into the tubing system delivering the gas into the chamber. In the case presented in Fig. 4.13 (p. 38), the RGA scan may identify the penetration of the outer atmosphere into Ar or O_2 feed tubing. Then, a raw scan of the plasma composition should be done in order to explore the ion fluxes drawn from the plasma into the spectrometer. Examples of these are given in Fig. 5.19 (p. 97): the plasma composition is explored (i) when discharge is operated in pure Ar atmosphere and also (ii) when the reactive gas is introduced into the system resulting in the decrease in gettering of the contaminants by the sputtered target-material.

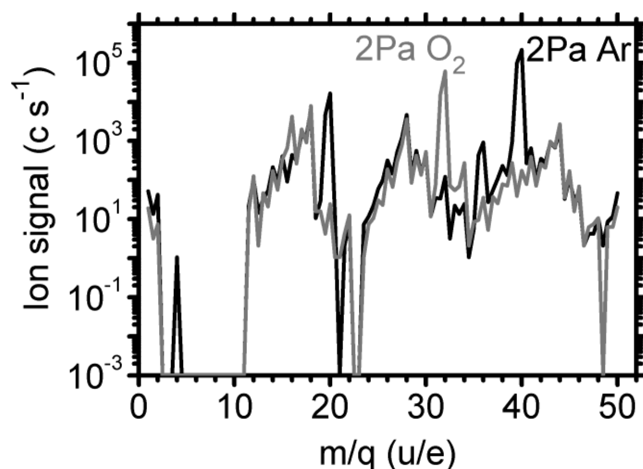

Fig. 4.13
RGA analysis performed when different filling gases are used. The contamination which is independent of the process-gas used is found in the system. Employing the RGA scan may reveal chamber leakages and leakages into a particular gas feed tubing. The signal is integrated over the 'Energy' scan ranging from -0.5 V to 4.0 V
Experimental Conditions: Ionization current set by 'Emission' = 2×200 μA (both electron-emitting filaments are operated), 'Electron-energy' = 70 V. Process-gas pressures and flows: argon 2 Pa, 30 sccm, oxygen 2 Pa, 33 sccm.

When it is assured that the concentration of contaminating species is reasonably low, the proper tuning procedure, proposed in Sec. 4.1.4 (p. 31), should be performed. Considering the energy resolution and mass discrimination, it is reasonable to tune the spectrometer using the most abundant ionic species and to apply the same settings of the spectrometer also during measurements of fluxes of all the other species. Different settings of the spectrometer used for different ionic species would impose additional complications on the spectra interpretation.

As far as time-averaged measurements of pulsed discharges are concerned, the ratio of the pulse period to the 'Dwell time' (i.e. to the time of the acquisition of one sample of the signal) must be taken into account in order to correctly set the spectrometer. The 'Dwell time' should be several times longer than the pulse time to reduce a noise in the signal. When the ion-counting detector is used, the duty cycle also influences the interpretation of the signal intensity. For example, in the case of a 10% duty cycle, the signal should not attain more than 10% of the maximum signal intensity otherwise the detector becomes saturated within the pulse-on time. Therefore, it is advised to measure the waveform of the ion current onto the surface in the extractor position since the information on the time evolution of the ion current can be used to decide whether the detector became saturated within the pulse: the ratio of the maximum to the time-averaged value of the ion current should not exceed the ratio of the maximum recommended detector signal to its time-averaged (i.e. measured) value. Another way of how to check for the detector's saturation is to compare the fluxes of suitable isotopes of some specific ionic species. For example the abundance numbers of the ^{90}Zr and ^{91}Zr isotopes are 51.5% and 11.2%, respectively. If the corresponding signal intensities of these ionic species do not tally with these abundance numbers and if the signal of the ion with lower abundance number is higher than expected, it may be indicative of the detector's saturation.

If the signal intensity is too high and the detector becomes saturated, then either (i) the isotope of the ionic species of interest with lower a abundance number should be measured or (ii) a smaller extraction orifice should be used or (iii) the beam of ions inside the spectrometer should be defocused a bit using electrostatic lenses located closest to the spectrometer's detector [110].

The term 'time-resolved measurement' usually refers to a measurement of the plasma evolution within a pulse, i.e. commonly on the microsecond time scale. Yet, some plasma processes exhibit fluctuations in plasma parameters also on time scales of seconds. Especially in the case of controlled reactive sputtering it is important to determine the time-varying fluxes of ions onto the surface of the growing films. Then, the signal acquisition can be driven by external electronics connected to MSIU to scan the ion fluxes in the desired time intervals, see Fig. 4.12 (p. 37).

During the measurements, the extractor becomes covered by a layer of sputtered material impeding the flux of the ions into the spectrometer. Sometimes, the orifice becomes even blocked. The diameter of the orifice can be easily estimated by this procedure:

(1) Equip the spectrometer with an extractor orifice of a known cross-section.

(2) Pump down the chamber to the lowest reasonably attainable pressure (base pressure) and note the pressure measured by the spectrometer's pressure gauge.

(3) Introduce the process gas into the chamber. The process-gas pressure should be high enough to cause the pressure in the spectrometer to increase at least two orders of magnitude. Note the pressure in the chamber and the pressure measured by the spectrometer's pressure gauge.

(4) Each time the spectrometer is to be used, set the chamber pressure to the same value as in the step (3) and check the pressure in the spectrometer since this is indicative of the extraction orifice cross-section.

As demonstrated in Fig. 4.12 (p. 37), to measure the IESs of a particular ionic species, the mass-to-charge ratio of the ionic species is set and the output of the 'Energy' voltage source is changed in a stepwise manner. Since the plasma properties tend to submit to various fluctuations, especially in the case of HiPIMS processes, it is reasonable to measure the IES several times and then average.

The range of the energies of the ions detected by the spectrometer is limited by the capabilities of the 'Energy' voltage supply, see Fig. 4.3 (p. 24). The 'Energy' voltage source can provide a bias ranging from -100 V to +100 V. Fortunately, as shown in Fig. 4.3 (p. 24) , it is possible to bias the entire interior of the spectrometer by the spectrometer's inner 'Reference' voltage supply or to employ an external reference potential. Thus, also ions with energies (meaning the sum of the plasma potential and the kinetic energy of ions) exceeding 100 eV can be detected. In order to keep the consistency of the measurements, the difference between the extraction potential and the ground potential must be kept the same. For example, as illustrated in Fig. 4.14 (p. 40), the 'Extractor' was set to -5 V prior to the employing the 'Reference' voltage source. Then, the 'Reference' was set to +86 V, and, consequently, the 'Extractor' voltage had to be set to -91 V. The benefit is that the usable range of the 'Energy' voltage source was increased allowing us to use negative values of the 'Energy' voltage. In our particular example ('Reference' set to +86 V), setting 'Energy' to the voltage of -80 V caused the ions with the energy of 6 eV to be detected.

In case of IES measurements of negatively charged ions, the instructions given above can also be applied. Just the spectrometer should be set to the negative ion SIMS regime of operation and the appropriate extraction potential should be applied as discussed earlier in this section and in Sec. 4.1.4 (p. 31).

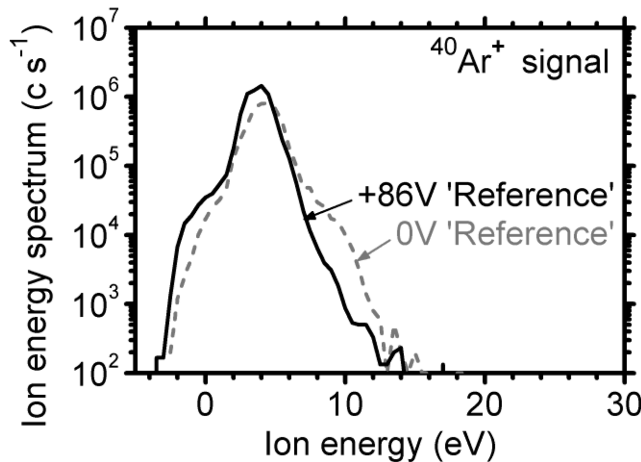

Fig. 4.14
Sensitivity of the ion energy spectra to the spectrometer's bias. Biasing the spectrometer by the 'Reference' voltage source from 0 V to +86 V requires a shift in the voltages applied to the 'Extractor' from -5 V to -91 V Then, the entire ion energy spectra must be shifted by the respective value of -86 eV. As a consequence, it is possible to detect the ions with energies up to 180 eV.
Experimental conditions: Pulsed DC discharge, discharge voltage U_d = 380 V, repetition frequency f_r = 500Hz, pulse-on time t_1 = 200 µs, average target power density in a period $\overline{S_d}$ = 4.8 Wcm^{-2}, argon process-gas pressure p = 2 Pa, target-to-orifice distance d = 100 mm.

4.1.6 Spectra interpretation

The following issues are to be discussed when it comes to the interpretation of the spectra measured:

(1) **The probe acceptance angle**. Because of the unknown directional distribution of the flux of the ions and because of the complicated nature of the particle trajectories in the plasma sheath, the influence of the acceptance angle is neglected, see the paragraph '**Extraction system – acceptance angle**' on p. 27.

(2) **The relation between the measured energy of the ions and their charge state.** The thorough analysis given in Sec. 4.1.2 (p. 25) reveals that the energies of singly charged ions in the units of eV correspond to the output voltage of the 'Energy' source. If the 'Reference' source is employed, the energy of singly charged ion corresponds to the sum of 'Reference' and 'Energy' voltages. The energy of the multiply charged ions, as determined by the sum of 'Energy' and 'Reference' voltages, must be multiplied by the respective charge state number of the ions to obtain the correct value of their energies.

(3) **The magnitude of signal intensities of multiply charged ions.** The factors to be taken into account are presented in Sec. 4.1.2 (p. 25) and Sec 4.1.3 (p. 27): (i) the energy spread of the multiply charged ions passing the energy filter is directly proportional to the charge state number of the ion resulting in a higher signal of multiply charged ions, see the paragraph '**Energy filter –**

resolution' on p. 28, (ii) the time of flight of multiply charged ions through the quadrupole mass filter decreases with the square root of the charge state number of the ion, i.e., the velocity of the ion through the filter increases and thus the mass filtering is reduced resulting in a higher signal of multiply charged ions , see the paragraph '**Mass discrimination**' on p. 29, and (iii) the sensitivity of the detector which is different for different ionic species, see paragraph '**Sensitivity of the detector**' on p. 30. The first two phenomena are to be kept in mind, but the exact evaluation of their effect on the signal magnitudes is a difficult issue. Commonly, no corrections are done to compensate them. The third one can be eliminated by setting an adequate '1st-Dynode' bias.

(4) **The magnitude of the signal of ions with different mass-to-charge ratio.** The mass discrimination of the spectrometer is presented in Sec. 4.1.3, in paragraph '**Mass discrimination**' on p. 29, showing that the signal of ions with a higher mass-to-charge ratio is suppressed. Commonly, no corrections are done to compensate this effect.

(5) **The signal of ions detected when the 'Energy' voltage is set to values lower than the 'Reference' voltage, i.e. ions with energies below 0 eV**. The elucidation of this phenomenon is illustrated in Fig. 4.15 (p. 42) and by the spectrometer's circuitry diagram presented in Fig. 4.3 (p. 24). For the sake of clarity, only the case of a positive ion SIMS measurement is discussed. An ion which is formed in the region where the electric potential is lower than the ground potential can be extracted by the 'Extraction' potential which is set negative with respect to the ground potential. As the ion enters the spectrometer it is accelerated by the sum of 'Energy' and 'Axis' potentials. Let the 'Energy' potential be set to 0 V, then the negative 'Axis' potential causes the ion to be drawn towards the energy filter. But the kinetic energy of the ion is lower than the 'Axis' so the ion does not pass through the energy filter. Now, let the 'Energy' potential be set to the value equal to that of the potential in the place where the ion was formed, i.e. to a negative value. Then, under the assumption of no collision of the ion with any other particle, the kinetic energy of the ion in the energy filter is equal to the 'Axis' potential and it passes through the filter. As a result, an ion with a "negative" energy can be detected. The same explanation fits the situation when an ion formed in the region of a positive electric potential (with respect to the ground potential) moves towards the extraction orifice and loses its kinetic energy in a collision with another particle in the vicinity of the negatively biased extractor. When the IESs are measured during the depositions of insulating films, it must be taken into account that (i) some of the surfaces of the spectrometer – especially those in its extraction section – are being covered by an insulating film, (ii) the value of a floating plasma potential may attain values several volts negative with respect to the ground and (iii) electrons emitted from the surfaces – e.g. as a result of an ion impact – on a floating plasma potential may have kinetic energies sufficient to ionize the gaseous particles. Consequently (i) the potential applied on the extraction electrode may be shielded by the charge build-up on the insulating film which covers it, (ii) the potential barrier separating the spectrometer interior and plasma space is lowered (potential applied on 'Lens1' is typically lower than -70 V see Fig. 4.3 [p. 24]) and (iii) gaseous species are ionized in a space domain where the electrostatic potential is lower than the 'Extractor' voltage. As a result, the ions with "negative" kinetic energies lower than 'Extractor' voltage are detected. Furthermore, (i) considerable number density of plasma species may penetrate the interior of the spectrometer and (ii) neutral particles may be ionized inside the spectrometer also in the SIMS mode of operation, both making the spectra interpretation even

more complicated. The need for measurement of the fluxes of ions with “negative” energies stems from the nature of the spectra calibration procedure, see Sec. 4.2 (p. 42). The current probe is biased negatively w.r.t. the ground potential, so ions with “negative” energies are one of the components of an electric current drawn from the plasma. Then, the number of ions with “negative” energies striking the probe should be assessed in order to interpret the measured spectra. Moreover, it is often desirable to know the energy delivered by the flux of ions onto a negatively biased substrate.

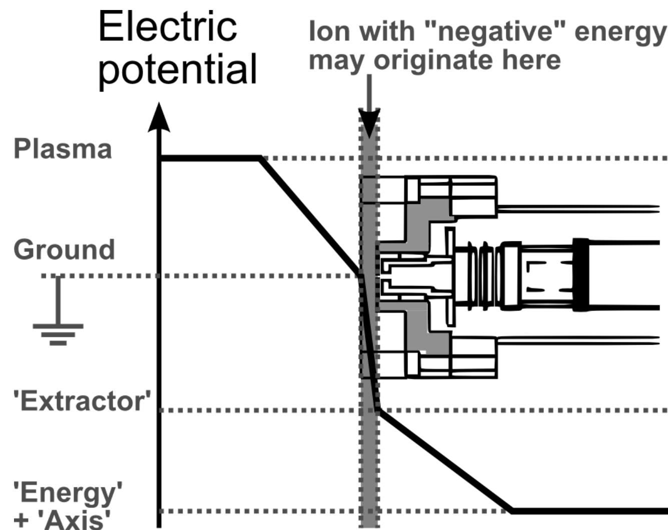

Fig. 4.15
The elucidation of the origin of positively charged ions with “negative” energies in the spectra as measured by the Hiden EQP 300 system. The extraction electrode is negatively biased with respect to the plasma to attract positive ions from the plasma region. An ion may undergo a collision or a neutral particle may be ionized in the region of negative potential (with respect to ground). Successively, the positively charged ion is accelerated towards the spectrometer by the extractor. Further acceleration of the ion is done by the sum of ‘Axis’ and ‘Energy’ potentials. The negative value of the ‘Energy’ voltage compensates the kinetic energy loss due to the escape from the extractor region. In other words, a negative potential applied on the ‘Energy’ electrode causes positive ions that (i) lost their kinetic energy or (ii) were formed in the space of a negative potential to enter the energy filter with energy equal to the value of the ‘Axis’ voltage and pass through it. This results in a reverse function of the ‘Energy’ source - the ion is accelerated by the ‘Energy’ potential as opposed to the usual decelerating role of the ‘Energy’ and, consequently, an ion with a “negative” energy may be detected.

4.2 Calibration of the ion energy spectra

The procedure presented in this section was employed to calibrate the energy spectra of the ions (IESs) striking the surface at the substrate position. The procedure may be applied to process time-averaged as well as time-resolved IESs depending on the provided input data. The assumptions used to make the

procedure of IES calibration clear are presented in one list using a lower-case Roman numbering and introduced step by step as they are applied.

The inputs of the procedure are:

- The density of the ionic current on the surface in the units of Am^{-2}. The current probe must be negatively biased with respect to the local plasma potential in order to avoid an electron current being drawn from the plasma.
- The energy spectra (IESs) of a particular ionic species in the units of counts per second (cs^{-1}), as measured by the mass spectrometer.

The output of the procedure is:

- The ion energy distribution functions (IEDFs) in the units of $eV^{-1}s^{-1}m^{-2}$. This should not be confused with ion energy distributions IEDs expressed in the units of $eV^{-1}m^{-3}$ which refer to the distributions of the particles in the phase space.

The first set of assumptions is: **(i)** the total signal of a particular plasma species can be evaluated based on the signal of one of its isotopes, **(ii)** the flux of ions onto the surface is proportional to the signal intensity and **(iii)** the ionic flux is composed exclusively of the ions whose energy spectra were provided as the inputs. This allows us to write

$$\Gamma_I^n(\varepsilon) = f_I^n(\varepsilon) S_I^n(\varepsilon) = f_I^n(\varepsilon) S_{Isotope}^n(\varepsilon) / a_{Isotope}^n \quad , \qquad (4.8)$$

Here, $\Gamma_I^n(\varepsilon)$ is the flux of all ionized isotopes of the n-th chemical species impinging on the surface with the kinetic energy ε, $S_I^n(\varepsilon)$ denotes the sum of signals of all the isotopes of that chemical species and $S_{Isotope}^n(\varepsilon)$ is the signal of the spectrometer set to detect a specific isotope with the kinetic energy ε. Note that the correct value of ε is calculated by multiplying the potential applied on the 'Energy' electrode by the corresponding charge state number of the ionic species, as described in Sec. 4.1.2 (p. 25). $a_{Isotope}^n$ is the isotope abundance number and $f_I^n(\varepsilon)$ stands for the function relating the signal of the particular ionic species as measured in the units of cs^{-1} to the flux of the ions in the units of $eV^{-1}s^{-1}m^{-2}$. $f_I^n(\varepsilon)$ also compensates for all the phenomena related to the spectrometer's sensitivity, as introduced in Sec. 4.1.3 (p. 27): acceptance angle, energy resolution, mass discrimination and detector's sensitivity. Later in this section it will be demonstrated that it is sufficient to know the ratio of all the $f_I^n(\varepsilon)$ functions to some reference function $f_I^{n,ref}(\varepsilon)$ in order to perform the calibration procedure.

The energy distribution of the ionic flux, introduced in Eq. 4.8, is considered to be a continuous function and the total flux of a particular ionic species is

$$\Gamma_I^n = \int_0^{+\infty} \Gamma_I^n(\varepsilon) d\varepsilon = \int_0^{+\infty} f_I^n(\varepsilon) S_I^n(\varepsilon) d\varepsilon \quad . \qquad (4.9)$$

Due to the method of signal acquisition used by Hiden EQP 300 system (the output of all voltages sources are changed in steps and are set to particular values for a certain period of time, see Sec. 4.1.2 [p. 25]), the spectrometer's output signal is available at discrete values of energy, ε_j. Then, **(iv)** the signal variations are assumed to be reasonably low within the energy interval $\varepsilon_j^{n,step} = \varepsilon_{j+1} - \varepsilon_j$ and **(v)** the $\varepsilon^{n,step}$ is a constant value. Because the value of $\varepsilon^{n,step}$ is directly set by the spectrometer as the difference between the steps in the 'Energy' voltage, it must be multiplied by the ion charge state number of the respective ion. To simplify the calculations, **(vi)** $f_I^n(\varepsilon)$ functions are assumed to be independent of energy ε. Then, Eq. 4.9 can be written in the form of sum

$$\Gamma_I^n = \sum_j \Gamma_I^n(\varepsilon_j)\varepsilon_j^{n,step} = \sum_j f_I^n(\varepsilon_j) S_I^n(\varepsilon_j)\varepsilon_j^{n,step} = f_I^n \varepsilon^{n,step} \sum_j S_I^n(\varepsilon_j) \quad . \tag{4.10}$$

The total ionic flux onto the substrate is

$$\Gamma_I = \sum_n \Gamma_I^n = \sum_n f_I^n \varepsilon^{n,step} \sum_j S_I^n(\varepsilon_j) \quad . \tag{4.11}$$

It is helpful to introduce F_I^n as the ratio of the flux of the n-th ionic species to the total ionic flux.

$$F_I^n = \Gamma_I^n / \Gamma_I \quad . \tag{4.12}$$

Clearly, $\sum_n F_I^n = 1$. In this step, it is impossible to evaluate the particular F_I^n since the values of all the calibration constants, f_I^n, are unknown. That is why the constants $f_I^{n,rel}$ are introduced as

$$f_I^{n,rel} = f_I^n / f_I^{ref} \quad . \tag{4.13}$$

Here f_I^{ref} is chosen from the set of the f_I^n constants as the reference. Obviously, it is sufficient to know the ratio of the spectrometer's sensitivity to the n-th species to the spectrometer sensitivity to the reference species.

For example, consider the fluxes of $^{16}O^{2+}$ and $^{40}Ar^{+}$ ions. Let (1) the $^{40}Ar^{+}$ be the reference specie, (2) the spectrometer's energy resolution of the $^{16}O^{2+}$ 2.0 times as high as that of the $^{40}Ar^{+}$ ions (the flux of $^{16}O^{2+}$ is 2.0 times decreased by the energy filter with respect to the flux of $^{40}Ar^{+}$) and (3) the mass discrimination of the $^{40}Ar^{+}$ be 0.8 of that of the $^{16}O^{2+}$ (the flux of $^{16}O^{2+}$ is 1.25 times increased by the spectrometer with respect to the flux of $^{40}Ar^{+}$). Then, $f_I^{O2+,rel} = f_I^{O2+} / f_I^{Ar+} = 2.0 \times 0.8 = 1.6$. By definition, $f_I^{Ar+,rel} = 1.0$.

The corresponding fractions of particular fluxes in the total flux are determined as

$$F_I^n = \frac{f_I^{n,re.l}\varepsilon^{n,step}\sum_j S_I^n(\varepsilon_j)}{\sum_n f_I^{n,rel}\varepsilon^{n,step}\sum_j S_I^n(\varepsilon_j)} \quad . \tag{4.14}$$

Furthermore, if **(vii)** the spectrometer's sensitivity is assumed to be the same for all the measured ions, the Eq. 4.13 is reduced to

$$F_I^n = \frac{\varepsilon^{n,step}\sum_j S_I^n(\varepsilon_j)}{\sum_n \varepsilon^{n,step}\sum_j S_I^n(\varepsilon_j)} \quad . \tag{4.15}$$

Clearly, the values of F_I^n can be calculated since $\varepsilon^{n,step}$ and $S_I^n(\varepsilon_j)$ are known.

The flux of each ionic species onto the surface gives rise to the net electric currents of the density J^n. Using Eqs. 4.10 – 4.12, this can written as

$$J^n = \varepsilon^{n,step}\sum_j \Gamma_I^n(\varepsilon_j)(eQ_I^n + e\gamma_{se}^n) = eQ_I^n\Gamma_I^n + e\gamma_{se}^n\Gamma_I^n = e\Gamma_I(Q_I^n F_I^n + \gamma_{se}^n F_I^n) \quad , \tag{4.16}$$

where e, $e > 0$, is the elementary charge Q_I^n is the ion charge state number and γ_{se}^n stands for the secondary electron emission yield which is assumed **(viii)** to be independent of the kinetic energy of the impinging ion and also **(ix)** independent of the particular ionic specie. Then, the secondary emission yield is denoted as γ_{se}. This choice is assumed to be reasonable because the secondary emission is dependent also on the properties of the surface which are hard to determine. The total net current is

$$J = e\Gamma_I\left(\sum_n Q_I^n F_I^n + \gamma_{se}\right) \quad , \tag{4.17}$$

which allows us to evaluate the total ionic flux onto the surface, Γ_I,

$$\Gamma_I = \frac{J}{e\left(\overline{Q}_I + \gamma_{se}\right)} \quad , \tag{4.18}$$

where $\overline{Q}_I = \sum_n Q_I^n F_I^n$ is the mean ion charge state number in the flux. Substituting Eq. 4.18 into Eq. 4.12

gives the ionic fluxes of particular ionic species Γ_I^n

$$\Gamma_I^n = F_I^n \frac{J}{e\left(\overline{Q}_I + \gamma_{se}\right)} \quad . \tag{4.19}$$

Making use of Eq 4.10, the respective calibrating constants f_I^n are readily obtained

$$f_I^n = \frac{\Gamma_I^n}{\varepsilon^{n,step} \sum_j S_I^n\left(\varepsilon_j\right)} \quad . \tag{4.20}$$

Finally, applying Eq 4.18, the spectrometer's output signal, $S_{Isotope}^n(\varepsilon)$, can be expressed in the form of IEDF in the units of $eV^{-1}s^{-1}m^{-2}$.

4.3 Deposition system and experimental conditions

In this section, the deposition system used for the depositions of zirconium (Zr) and zirconium-oxide (ZrO_x) films is described and the basic quantities used to characterize the deposition process are given. The same vacuum chamber, pumping system, power supply, magnetron plasma source and measurement equipment were used for all depositions. In the case the of ZrO_x depositions, the oxygen (O_2) inlet piping, O_2 flow control system and additional ring-shaped anode were integrated into the deposition system. These differences as well as the different experimental condition are presented.

4.3.1 Deposition system in general, basic definitions

The experiments were performed using a strongly unbalanced magnetron source with a directly water-cooled planar Zr target (99.9% Zr purity, diameter of 100 mm and thickness of 6 mm) in a standard stainless-steel vacuum chamber (diameter of 507 mm and length of 520 mm), which was evacuated by a diffusion pump (2 m^3s^{-1}) backed up with a rotary pump (30 m^3h^{-1}). The base pressure before deposition was 10^{-3} Pa. The argon (Ar) process gas of 99.999% purity was used. The magnetron's geometry and the model of its magnetic field are given in Fig. 4.16 (p. 47). The maximum parallel component of the magnetic induction above the racetrack region, measured at the distance z = 4 mm from the target surface, was 425 G. The absolute values of the corresponding vertical component, being up to 1500 G at the target surface, were approximately 30 G and 10 G for z = 60 mm and 180 mm, respectively [111]. This configuration of the magnetic field was used to enhance the transport of ionized sputtered atoms along the target normal to the substrate, to reduce the ion losses to chamber walls and to provide an additional electron impact ionization of the sputtered atoms in the bulk of the plasma and in the substrate's vicinity.

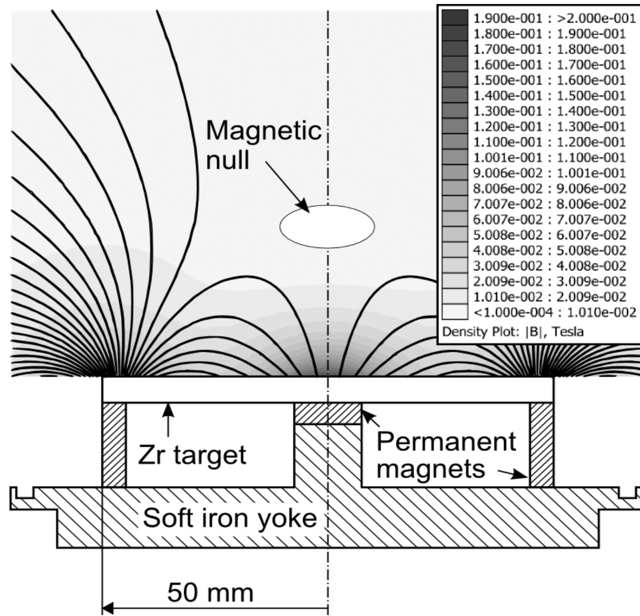

Fig. 4.16
Model of the magnetic field of the magnetron. The field lines of the magnetic induction and the location of the magnetic null region are given. FEMM code was used to evaluate the magnetic field. Permanent magnet material was modeled using a 'Linear B-H Relationship'; its values of the relative permeability and the coercive force were set to 1.1 and 8×10^5 Am^{-1}, respectively. Software's default magnetization curve for 'Pure Iron' was used for the yoke material. The zirconium target was modeled as a diamagnetic region [135].

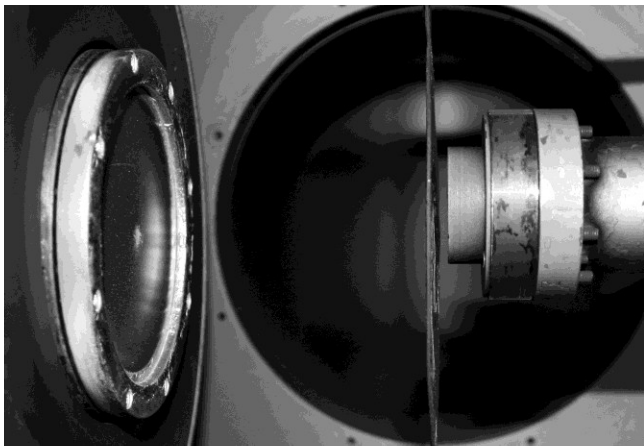

Fig. 4.17
Detail of the spectrometer sampling orifice located in the face-to-face position with respect to the magnetron target surface. For more details see Fig. 4.18 (p. 48).

The magnetron was driven by a pulsed DC power supply (HMP 2/1, Hüttinger Elektronik). In this work, the repetition frequency, f_r, was 500 Hz and the corresponding pulse period, $T = 1/f_r$, was 2000 µs. Waveforms of the magnetron voltage, $U_d(t)$, and the discharge current, $I_d(t)$, were monitored using a voltage probe (GE 3421, General Elektronik) and a current probe (TPC 303, Tektronix), which was connected to an amplifier (TCPA 300, Tektronix). The voltage probe and the current probe amplifier were connected to a digital oscilloscope (M 621, ETC) and our own software evaluated the average target power density in a period, $\overline{S}_d$, given by

$$\overline{S}_d = \frac{1}{T}\int_0^T U_d(t) J_t(t)\,dt \quad . \qquad (4.21)$$

Here, the target current density $J_t(t) = I_d(t)/A_t$, where A_t = 78.54 cm^2 is the total area of the target. The same integral expression was used to calculate the average target current, $\bar{I}_d$, average target current density, $\bar{J}_t$, the average substrate current, $\bar{I}_s$, and the average substrate current density, $\bar{J}_s$, in a period. The average target power density in a pulse, S_{da}, was evaluated with the use of the formula

$$S_{da} = \frac{1}{t_1}\int_0^{t_1} U_d(t) J_t(t) dt \quad , \qquad (4.22)$$

where t_1 denotes the pulse-on time. The same integral expression was used for calculations of the average magnetron voltage, U_{da}, and the average target current density, J_{ta}, in a pulse. The Zr and ZrO_x films were deposited on silicon substrates at a floating potential. The target-to-substrate distance, d, was 100 mm.

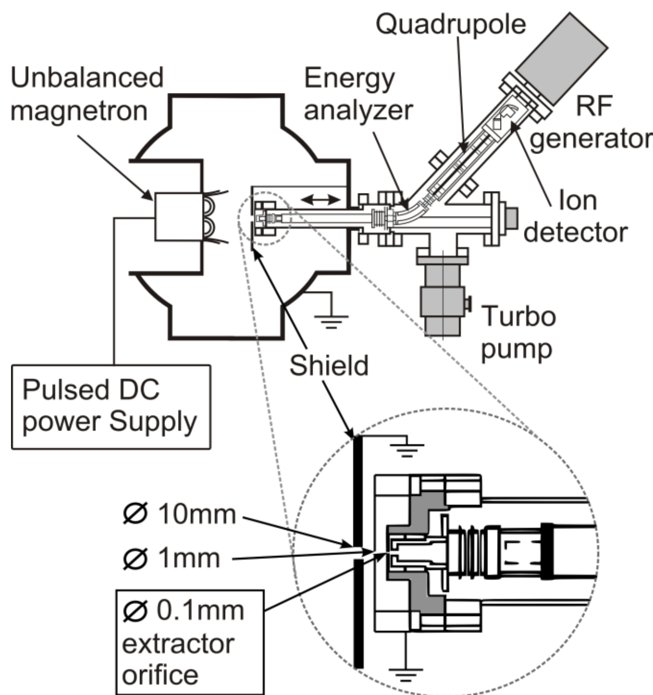

Fig. 4.18
System setup for mass spectroscopy measurements. To reduce the thermal loading of the spectrometer, an additional grounded cylindrical shielding shutter with a diameter of 110 mm with a 10 mm-diameter hole in the center was located 5 mm in front of the end cap of the mass spectrometer barrel. The extraction electrode with a 0.1 mm-diameter orifice in the center was placed 2.5 mm behind a grounded front electrode of the spectrometer with a central input aperture with 1 mm in diameter.

The time-averaged energy-resolved spectra of positive ions were measured with the mass spectrometer (EQP 300, Hiden Analytical). To perform these measurements under the conditions of very large ion fluxes at high target power densities during pulses, an additional grounded cylindrical shielding shutter with a 10 mm diameter hole in the center was located 5 mm in front of the special end cap of the mass spectrometer barrel. The diameter (110 mm) of the shielding shutter was the same as that of the substrate holder. We used a modified configuration of the cap in which an extraction electrode with a 100 μm diameter orifice in the center was placed 2.5 mm behind a grounded front electrode of the spectrometer with a central input aperture with 1 mm in diameter. The schematics and the photo of the placement of the

spectrometer in the vacuum chamber together with the details of the spectrometer's shielding are provided in Fig. 4.18 (p. 48) and in Fig. 4.17 (p. 47).

Prior to the ion energy distribution measurements, the discharge regime with the highest value of $\overline{S}_d$ (100 Wcm^{-2}) and longest t_1 (200 μs) was used for tuning the spectrometer to obtain a maximum $^{40}Ar^+$ signal while keeping the extraction electrode at -5 V with respect to the ground potential. Then, each ion energy distribution was measured and the integral fluxes of the individual ionic species were determined by a direct integration of the respective time-averaged energy distributions. For all discharge regimes and ion species considered, the spectrometer was operated under the same parameter settings in order to have a consistent comparison of signal intensities. All isotopes of Zr ($^{90\text{-}92,94,96}Zr$) and two isotopes of Ar ($^{36,40}Ar$) were considered. Owing to the same behavior of the different isotopes, sums of the corresponding isotope contributions were presented. Assuming the same characteristics for the transmission of all the ionic species through the instrument, the composition of the total ion flux onto the substrate was calculated using the particular integral ion fluxes determined.

4.3.2 HiPIMS depositions of zirconium

During some of the experiments, the pulsed DC power supply worked in a modified regime with a negative voltage (approximately 25% of the pulse-on time value) at the magnetron target during the pulse-off time (see Fig. 5.1 [p. 68]). The current-voltage waveforms are provided for each set of experiments, so it is always clear whether the power supply was operated in the above mentioned modified regime or not. The Ar process-gas pressure was set to 1 Pa.

A flat probe with a diameter of 20 mm was applied to measure the substrate current, $I_s(t)$. In Fig. 4.19 (p. 50), the schematics of the probe, its circuitry and its connection to the deposition system are delineated. One of the main advances of this probe design is the relatively stable active surface of the probe as the probe current and/or probe bias is changed. The probe system must be capable of measurements of (i) waveforms of the probe current and of (ii) mean values of the probe current. The first task was readily resolved by direct connection of the current probe to the flat-probe connecting conductor. The latter one could not be solved making use of the current probe since an electromagnetic interference in the current-probe signal (caused by unavoidable occasional arcing events within the chamber) resulted in a shift of the probe's offset value. So it was necessary to add an additional circuitry and robust DC measuring equipment to the probe. In order to attain a stable probe bias, a capacitor was attached to the flat probe to diminish the impact of high instantaneous current loadings on the stability of the bias voltage source. Then, a resistor suppressing the current fluctuations was mounted between the voltage source and the capacitor. The capacitor of 330 μF and resistor of 160 Ω were used and found to be sufficient to stabilize the probe bias and to allow for reliable measurements of the mean value of substrate current, $\overline{I}_s$, under the conditions investigated.

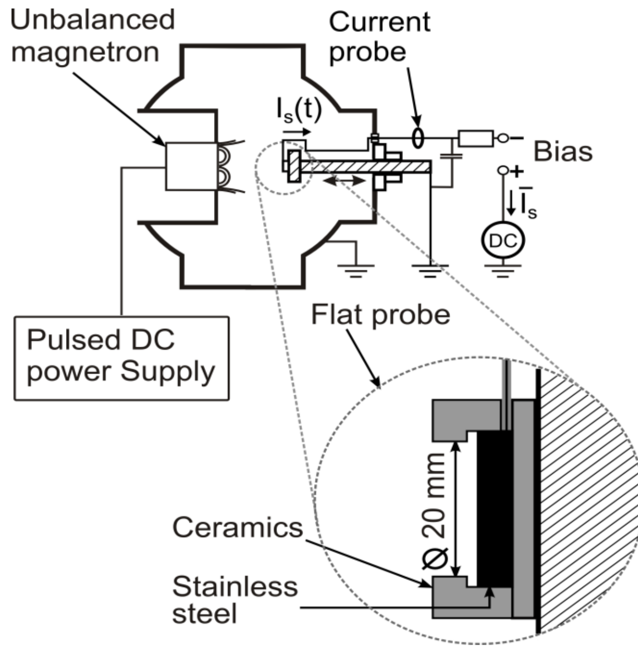

Fig. 4.19

System setup for substrate current, $I_s(t)$, measurements. To stabilize the probe bias, a capacitor (330 μF) was attached parallel to the flat probe and a resistor (160 Ω) was mounted between the voltage source and the capacitor. The time evolutions of $I_s(t)$ were measured by the current probe and the mean value of substrate current, $\bar{I}_s$, was explored by a DC current meter.

The probe was positioned in the center of the substrate holder (on the magnetron axis of symmetry) and electrically isolated from it. Substrate currents were measured at distances d = 70 mm, 100 mm and 200 mm from the target. The probe bias was set to -50 V with respect to the ground potential to repel the electrons coming from plasma space. As a result, only the current of positively charged ions and secondary electrons was measured allowing us to calculate the net ion current after subtracting the secondary electron component. Waveforms of the $I_s(t)$ currents were monitored with a current probe (TCP 312, Tektronix) connected to an amplifier (TCPA 300, Tektronix) and recorded by a digital oscilloscope (TDS 2002 B, Tektronix). The mean values of the $I_s(t)$, i.e. $\bar{I}_s$, were measured with an analog DC current meter (DU20, Metra).

The mass spectrometer was placed at the target-substrate axis in positions directly facing the target surface at the distances of 70 mm, 100 mm and 200 mm from the target (see Fig. 4.17 [p. 47]). The ion energy distributions were measured in the interval from -15 eV up to 100 eV in the 0.2 eV steps. The acquisition time of each data sample was 100 ms and the energy distribution of each ionic species was scanned 5 times and then averaged.

For any discharge conditions, the substrate current density, the ion flux characteristics and the deposition rate were measured during separate experiments. This resulted in slightly different experimental situations (at constant $\bar{S}_d$ the values of $U_d(t)$ decreased and the values of $I_d(t)$ increased by up to 9%) owing to a continuing target erosion. The maximum depth of the race track increased from 1.0 mm to 2.5 mm during the experiments presented.

4.3.3 Reactive HiPIMS depositions of zirconium oxides

In this work, HiPIMS depositions of ZrO_x films were performed using instrumentation which is currenly a subject matter of an ongoing patent process. Therefore, the experimental details are just outlined.

In order to perform reactive depositions of ZrO_x films, an enhanced reactive-gas piping system was embedded into the vacuum chamber. Prior to letting oxygen (O_2) into the system, the Ar flow rate was set to 30 sccm and the system pumping speed was adjusted to attain the pressure of 2 Pa. The settings of Ar flow rate and pumping speed were not changed during the experiment. This value of Ar pressure was set since it was high enough to help reduce the number of arcing events at the target surface and, at the same time, low enough to keep the mean free paths of the gaseous species sufficiently long to allow their fluxes to be directional. The value of O_2 reactive-gas (RG) flow rate, Q, and the value of U_d were driven by the controller.

Due to the well-known 'disappearing anode' effect [8], an additional ring-shaped anode was mounted into the system around the insulated substrate holder located at the distance of 100 mm from the target. It was cleaned periodically to remove the non-conducting ZrO_x layer from its surface and thus to stabilize the discharge conditions. In addition to that, formation of a ZrO_x layer of uncertain electrical properties on all the surfaces inside the deposition chamber precluded the usage of the flat probe to measure the substrate current, $I_s(t)$. On that account, $I_s(t)$ was not investigated at all.

The mass spectrometer was placed at the target-substrate axis in position directly facing the target surface at the distance of 100 mm from the target, analogously to the case of non-reactive sputtering experiments, see Fig. 4.17 (p. 47). The 'Reference' voltage source was used to bias spectrometer electrodes to the value of +86 V which enabled to explore the ion energy distributions in the interval from -8e V up to 186 eV.

To obtain information on the system's contamination and on the composition of the plasma, the spectra of neutral gas species and spectra of positive ions were scanned using the mass-to-charge ratio ranging from 1 u/e to 50 u/e and from 1 u/e to 140 u/e, respectively. The neutral species were detected employing the RGA mode of the spectrometer utilizing the spectrometer's internal ionization source. The fluxes of ionic species were scanned in the interval of energies ranging from -2 eV up to 20 eV. The spectra were measured 10 times and averaged.

The measurements of the IEDFs were performed in two regimes: time-averaged and time-resolved with the 2 s window for spectra acquisition (Fig. 5.17(c) [p. 93]). To perform time-averaged scans, the IEDF of each ionic species was scanned 20 times and then averaged. In the case of time-resolved scans, the IEDF were scanned 5 times and averaged to reduce time demands of the measurements. Each time, the IESs were scanned in 2 eV steps and the acquisition time of each data point (sample) was 100 ms.

4.4 Measurements of film properties

The Zr and ZrO_x films were deposited on silicon substrates at floating potential. The film thickness was measured by profilometry (Dektak 8 Stylus Profiler, Veeco) using a 380 μm thick removable Si step and the corresponding deposition rate, a_D, was determined as the ratio of the film thickness to the deposition time. All the properties listed below were measured in the case of the ZrO_x films.

The elemental composition of the films was measured by a PANalytical wavelength-dispersive X-ray fluorescence spectrometer MagiX PRO equipped with a 4 kW Rh-target X-ray tube. Analytical software SuperQ was used for data collection and FP-Multi software was used for calibration and quantitative data analysis. The following four lines, Zr Kα, Zr Lα, Si Kα and O Kα, were measured. As calibration standards for the FP-Multi software, we used several ZrO_x films on the Si (100) substrate analyzed by a Rutherford backscattering spectrometry. The accuracy of the measurements of the zirconium and oxygen contents in the films can be approximately characterized by 5-7 at. %. X-ray diffraction measurements were collected at a room temperature on a PANalytical X'Pert PRO diffractometer working in Bragg-Brentano geometry using a Cu Kα (40 kV, 40 mA) radiation, a 0.5° divergent slit, 0.04 rad Soller slits, Ni filter for Cu Kβ elimination and an ultrafast semiconductor detector X'Celerator. To avoid a strong reflection from the Si (100) substrate, a slightly asymmetrical diffraction geometry with an ω-offset of 1.5° was used. Samples were scanned over the 2θ-range from 8° to 108° with a scanning speed of $0.0016°s^{-1}$. Data evaluation was performed with a PANalytical software package HighScore Plus. 65°, 70° and 75° in reflection.

The optical data were fitted in the 300-2000 nm range using the WVASE software and an optical model consisting of a c-Si substrate, a ZrO_2 layer and a surface roughness layer. The ZrO_2 layer was described by a Cauchy dispersion formula with an Urbach absorption tail (and a Cody-Lorentz formula for cross-check purposes), combined with Lorentz oscillators for semi- or nontransparent samples ($k \geq 0.1$). Film hardness was determined using a computer-controlled microhardness tester (Fischer-scope H-100B) with a preset maximum load of 20 mN.

4.5 Sputtering process analysis

In this section, the quantities used for the characterization of the processes in HiPIMS of Zr are defined. The analysis is analogous to that performed to elucidate the IEDF calibration, see Sec. 4.1.6 (p. 40). For the sake of clarity, the definitions of key variables are included.

Taking into account that the target current density, J_t, and the substrate current density, J_s, consist of the ion and the secondary electron components, the total current densities can be written in the form similar to that introduced in Eq. 4.16 (p. 45).

$$J = e\Gamma_I\left(\sum_n Q_I^n F_I^n + \sum_n \gamma_{se}^n F_I^n\right) \quad . \tag{4.23}$$

The meaning of the symbols remains the same: e, $e > 0$, is the elementary charge, Γ_I^n is the flux of ions of type n, Q_I^n is the corresponding ion charge state number, γ_{se}^n is the corresponding secondary-electron emission coefficient of the target-material and F_I^n denotes the fraction of the particular type of ions in the total ion flux, Γ_I.

Owing to the lack of data in the literature, it is difficult to evaluate the effect of the secondary electron emission on the characteristics of the HiPIMS discharges with high fluxes of target-material ions (singly and even doubly charged) incident on the target and the substrate [44,103]. Moreover, a significant fraction of the electrons emitted from the magnetron target is expected to be recaptured at the target surface due to the strong magnetic field affecting their motion near the target. Taking into consideration that the yields for the kinetic emission of electrons become comparable with those for the potential emission at the Ar^+ ion (or even Ar atom) impact energies above about 300 eV for “dirty” or “technological” surfaces [112,113], we used the following expression for all the coefficients γ_{se}^n in Eq. 4.23 (p. 52)

$$\gamma_{se}^n = (1 - r)\gamma_{se} \quad , \tag{4.24}$$

where γ_{se} is the secondary-electron emission coefficient of the target-material (Zr) for the potential emission by the incident process-gas ions (Ar^+ ions) and r is the recapture probability due to the reabsorption of electrons at the target or substrate surface. After substituting for γ_{se}^n from Eq. 4.24 into Eq. 4.23, we obtain

$$\Gamma_I = \frac{J}{e\left(\overline{Q}_I + (1 - r)\gamma_{se}\right)} \quad , \tag{4.25}$$

which is analogous to Eq. 4.18 (p. 45), where $\overline{Q}_I$ is the mean ion charge state number in the flux. In agreement with the literature, we took $\gamma_{se} = 0.128$, and $r = 0$ for the substrate surface and $r = 0.5$ for the magnetron target surface [101,103,114]. Based on the corresponding values of $\overline{J}_t$, $\overline{J}_s$ and J_{ta} given by the respective integral formulas in Eq. 4.21 (p. 47) and Eq. 4.22 (p. 48), Eq. 4.25 was used for calculations of the average total ion flux onto the target, $\overline{\Gamma}_{It}$, and onto the substrate, $\overline{\Gamma}_{Is}$, in a period, and of the average pulse total ion flux onto the target, Γ_{Ita}.

The fraction of the target-material ions in the total ion flux onto the substrate, m_s, and the ionized fraction of the target-material atoms in the flux onto the substrate, θ, are defined as

$$m_s = \frac{\overline{\Gamma}_{Is}(Zr)}{\overline{\Gamma}_{Is}(Ar) + \overline{\Gamma}_{Is}(Zr)} \tag{4.26}$$

and

$$\theta = \frac{\overline{\Gamma}_{Is}(Zr)}{\overline{\Gamma}_{Ns}(Zr) + \overline{\Gamma}_{Is}(Zr)} \quad , \tag{4.27}$$

where $\overline{\Gamma}_{Is}(Zr) = \overline{\Gamma}_{Is}(Zr^{+}) + \overline{\Gamma}_{Is}(Zr^{2+})$, and $\overline{\Gamma}_{Ns}(Zr)$ is the average flux of the sputtered zirconium neutrals (atoms) onto the substrate. Assuming the film density to be the same as that of the bulk material ($\rho = 6.52$ gcm^{-3}) [44,111] and the sticking coefficients of the impacting Zr atoms and ions to be equal to unity (note the low impact energies and the low off-normal angles of the particles [115-117]) in the experimental situations investigated, corresponding values of the deposition rate, a_D, were used for the calculation of the average total flux of deposited particles onto the substrate $\overline{\Gamma}_D = \overline{\Gamma}_{Ns}(Zr) + \overline{\Gamma}_{Is}(Zr)$, appearing in Eq. 4.27.

Under the realistic assumptions [101] that almost all of the applied magnetron voltage, U_d, is dropped across the target sheath and that this sheath is very thin (no collisions of ions within the sheath), the average flux of sputtered target atoms, $\overline{\Gamma}_{sp}$, can be expressed as

$$\overline{\Gamma}_{sp} = \sum_{n} \frac{1}{T} \int_{0}^{T} \gamma_{sp}^{n}\left(eQ_{It}^{n} U_d(t)\right) F_{It}^{n}(t) \Gamma_{It}(t) dt \quad , \tag{4.28}$$

where γ_{sp}^{n} is the sputtering yield of the target-material for ions of type n impacting the target. It can be readily calculated for the given kinetic energy of the particular ions, $eQ_{It}^{n} U_d$, using, for example, a TRIM code [118].

Now, (i) taking into account that the magnetron voltage, U_d, decreases relatively slowly during a pulse and that $U_d \cong 0.25 U_{da}$ in the pulse-off time (see Fig. 5.1 [p. 68]) and (ii) assuming the value of the F_{it}^{n} to be a constant over the whole period (the respective IEDFs measured are time-averaged as well), i.e $F_{It}^{n}(t) = \overline{F}_{It}^{n}$, Eq. 4.28 may be simplified as

$$\overline{\Gamma}_{sp} = \Gamma_{Ita} \frac{t_1}{T} \sum_{n} \gamma_{sp}^{n}\left(eQ_{It}^{n} U_{da}\right) \overline{F}_{It}^{n} + \left(\overline{\Gamma}_{It} - \Gamma_{Ita} \frac{t_1}{T}\right) \sum_{n} \gamma_{sp}^{n}\left(0.25 eQ_{It}^{n} U_{da}\right) \overline{F}_{It}^{n} \quad . \tag{4.29}$$

Note that the values of $\overline{\Gamma}_{It}$ and Γ_{Ita} are dependent on $\overline{F}_{it}^{n}$ (see Eq. 4.25 [p. 53] and Eq. 4.23 [p. 52]).

4.6 Mathematical modeling of reactive sputtering processes

In this section, the mathematical model employed to describe the controlled reactive sputtering process is described. The general structure of the model resembles the seminal model of steady-state reactive sputtering as introduced in works of Kusano and Berg and which was expanded to a dynamical one in the work of Kubart [91,104,119,120]. Here, the model of the target current as a function of the target poisoning and the model of the control system are integrated into a dynamical model to capture the behavior of the controlled reactive sputtering system, described in Sec. 4.3.3 (p. 51). Then, the procedure of fitting the parameters of the model is provided.

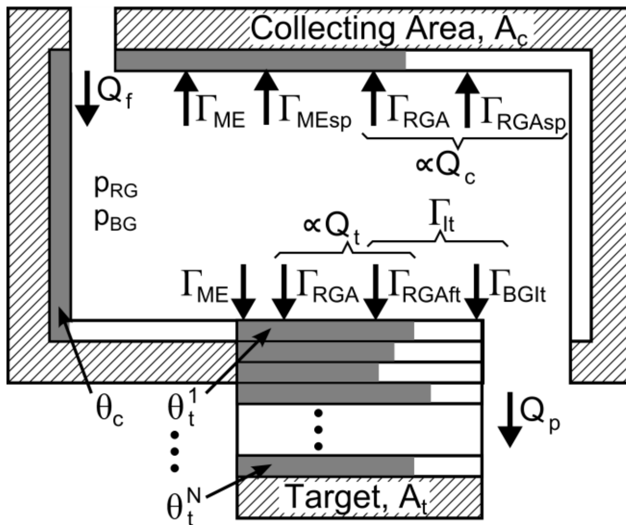

Fig. 4.20
Schematics of the processes included in the model of reactive sputtering deposition. The model divides the deposition system into five domains: (1) gas inlet (flow-in, f), (2) gas outlet (pump, p), (3) chamber volume, (4) collecting (c) area (A_c) and (5) target (t) area (A_t). The chamber is filled with a background inert gas (BG) and a reactive gas (RG) of pressures p_{BG} and p_{RG}. Particle fluxes per unit area are denoted by the 'Γ' letter, 'ME' denotes the sputtered metallic atoms, 'A' stands for atoms and 'I' designates respective ions. To simplify the model, all fluxes of RG species are expressed as fluxes of RG atoms (RGA). The 'Q' letters denote the overall fluxes of RG species. Elemental compositions of monolayers formed on surfaces are captured via 'θ' variables. Target surface is modeled as a set of N monolayers.

4.6.1 Model assumptions and governing equations

The assumptions made to establish the mathematical model are denoted by the lower-case Roman numbering and introduced step by step as they are applied.

Model of the dynamical behavior of the reactive sputtering process

(i) The deposition system is divided into several domains: 1) gas inlets, 2) pumping outlet of area A_p, 3) collecting surfaces of area A_c (comprising a substrate surface and chamber walls), 4) target surface of area A_t and 5) chamber of volume V. To take into consideration the penetration of fast species into the target surface, the target domain is subdivided into N sub-domains each representing one monolayer (either monoatomic or monomolecular) of a given chemical composition.

(ii) The plasma species are supposed to be uniformly distributed within the chamber neglecting the influence of magnetic and electric fields on their motion. The temperature, T, is assumed to be the same for all species and with no variations within the chamber.

(iii) The flux, Γ, of each neutral species onto the surfaces is given by $\Gamma = 0.25 n\bar{v}$, where n is the number density of the particular species and the $\bar{v}$ stands for the corresponding mean thermal velocity.

From the standpoint of model implementation, it is convenient to treat the fluxes and flux densities of plasma species in the units of atom s^{-1} and atom $m^{-2}s^{-1}$, respectively. Hence, applying the above mentioned assumptions, the flux of reactive species into the chamber, Q_f, in the units of atom s^{-1}

$$Q_f = q_f x_{RGAinRGM} \frac{p_{stnd}}{kT_{stnd}} \frac{10^{-6}}{60} = q_f x_{RGAinRGM} k_{qsccm} \quad , \tag{4.30}$$

where q_f denotes the flow rate of reactive gas in the units of sccm, $x_{RGAinRGM}$ is the number of reactive-gas atoms per one reactive-gas molecule (e.g. $x_{RGAinRGM} = 2$ for O_2), p_{stnd} is standard pressure, k is the Boltzmann constant, T_{stnd} is standard temperature (293.15 K) and k_{qsccm} is the conversion factor. The flux density of reactive-gas atoms, Γ_{RGA}, onto the surfaces is

$$\Gamma_{RGA} = \frac{1}{4} n_{RGA} \bar{v}_{RGM} = \frac{N_{RGA}}{V} \left(\frac{kT}{2\pi m_{RGM}} \right)^{0.5} = p_{RG} x_{RGAinRGM} \left(\frac{1}{2\pi kT m_{RGM}} \right)^{0.5} \quad , \tag{4.31}$$

Where N_{RGA} is the number of reactive-gas atoms within the chamber, p_{RG} is the partial pressure of reactive gas, and m_{RGM} denotes the mass of the reactive-gas molecule. The flow of the reactive species outside the system, Q_p, through the pumping outlet of area A_p is

$$Q_p = A_p \Gamma_{RGA} \quad . \tag{4.32}$$

(iv) The chemical species considered are: 1) the target-material (target is assumed to be metallic) – neutral atoms (ME), 2) the inert gas (background gas, BG) – neutral atoms (BGA), singly charged ions (BGI), 3) the reactive gas (RG) – molecules (RGM), singly charged molecular ions (RGI), neutral atoms (RGA), 4) the compound (COMP) – stoichiometric compound of ME and RG, i.e. ME $RG_{XRGAinComp}$.

(v) Generally, in the model, surface areas are treated as being composed of a set of monolayers. The chemical composition of each monolayer is described by its 'compound fraction' or 'coverage', θ, ranging from 0 to 1, meaning that the ratio of the number of ME atoms that form the compound with the reactive species to the number of all ME atoms in the monolayer is equal to θ. In a real situation, the compound is nearly uniformly distributed over the whole monolayer. In the model, the θ fraction of the layer is treated as a separate area formed solely by the compound. Accordingly, the 'metallic fraction' of the layer, $1-\theta$, is considered to consist of elemental non-reacted target atoms. Reactive-gas species are

assumed to form the compound with the metallic part of the surface and, furthermore, they are not assumed to be adsorbed on the compound fraction of the respective areas. On the other hand, the metallic atoms are considered to cover the areas formed by the compound and thus to decrease the respective θ fraction. Further in the text, $\dot{\theta}$ denotes the time derivative of the compound fraction.

In the model, the target surface is subdivided into N layers which may have different contents of the reactive species in order to simulate the implantation of reactive-gas species into the target. According to the above mentioned description of the chemical composition of the individual monolayers, the presence of reactive-gas atoms in the j-th target layer, j = 1..N, is expressed by the θ_t^j parameter.

The physical processes occurring on the target during the sputtering are the crucial ones with respect to the process stability and to the properties of the deposited films. To model particle fluxes onto the target and the target sputtering itself, it is assumed that:

(vi) The secondary-electron component of the electric current onto the target can be neglected. The ion flux onto the target is supposed to be composed of singly charged BG ions (e.g. Ar^+) and singly charged RG molecules (RGI, e.g. O_2^+), which results in the ion flux density, Γ_{It}, onto the "active" target area, A_t, i.e. onto the target erosion zone, to be

$$\Gamma_{It} = \frac{I_d}{eA_t} \quad . \tag{4.33}$$

The flux density of fast reactive-gas atoms, Γ_{RGAft}, onto the target is given by

$$\Gamma_{RGAft} = \Gamma_{RGMIt} x_{RGAinRGM} = \Gamma_{It} \frac{p_{RG}\beta_{RG}}{p_{RG}\beta_{RG} + p_{BG}\beta_{BG}} x_{RGAinRGM} \quad , \tag{4.34}$$

where Γ_{RGMIt} is the flux of ionized reactive-gas molecules onto the target, p_{RG} and p_{BG} are the partial pressures of reactive-gas molecules and background-gas molecules, β_{RG} and β_{BG} stand for the corresponding ionization probabilities.

(vii) The composition of the ion flux can be neglected for the evaluation of the sputtering yield. Only the particles in the target's topmost layer are sputtered and the sputtering yield is assumed to be influenced solely by the chemical composition of the topmost layer. Furthermore, both target-material and the compound-forming species are assumed to be sputtered as separate neutral atoms. Then, the flux density of sputtered target-material atoms, Γ_{MEsp}, is given by:

$$\begin{aligned} \Gamma_{MEsp} &= \Gamma_{It}\left(\gamma_{MEfromCOMP}\,\theta_t^1 + \gamma_{MEfromME}\left(1-\theta_t^1\right)\right) \\ &= \Gamma_{It}\left(\gamma_{MEfromME} + \left(\gamma_{MEfromCOMP} - \gamma_{MEfromME}\right)\theta_t^1\right) \quad . \end{aligned} \tag{4.35}$$

Here, $\gamma_{MEfromCOMP}$ and $\gamma_{MEfromME}$ denote the sputtering yield of the target-material atoms from the compound fraction of the target and from the metallic part of the target, respectively. The flux of reactive-gas atoms, Γ_{RGAsp}, sputtered from the compound fraction of the target is:

$$\Gamma_{RGAsp} = \Gamma_{It}\gamma_{RGAfromCOMP}\theta_t^1 \quad , \qquad (4.36)$$

where the $\gamma_{RGAfromCOMP}$ is the sputtering yield of reactive-gas atoms from the compound fraction of the target. Eqs. 4.33 – 4.36 enable the evaluation of the changes in the elemental composition of the target.

(viii) The chemical composition of the topmost target layer is assumed to be influenced by (1) the adsorption of neutral RG molecules onto the metallic fraction since RG molecules are supposed not to be adsorbed at the compound fraction, (2) the sticking of thermalized ME atoms onto the compound fraction, (3) target erosion causing the second target layer being exposed, (4) the sputtering of RGA and by (5) "knocking" RGA from the topmost layer into the bottommost layer by the impinging ions, the probability of an RGA being "knocked" is equal to $\left(1-\theta_t^N\right)$:

$$\begin{aligned} n_{st}x_{RGAinComp}\dot{\theta}_t^1 = & \overbrace{\Gamma_{RGA}\alpha_{RGMtoMEt}\left(1-\theta_t^1\right)}^{\text{RG sticking}} - \overbrace{\Gamma_{ME}\alpha_{MEtoCOMP}x_{RGAinCOMP}\theta_t^1}^{\text{sticking of thermalized ME}} \\ & + \overbrace{\Gamma_{MEsp}x_{RGAinCOMP}\theta_t^2}^{\text{Target erosion, 2nd layer is exposed}} - \overbrace{\Gamma_{RGAsp}}^{\text{RG sputtering}} - \overbrace{\Gamma_{It}\gamma_{KnockRGAfromCOMP}\theta_t^1\left(1-\theta_t^N\right)}^{\text{RG knocking}} \quad . \end{aligned} \qquad (4.37)$$

Here, n_{st} is the surface density of the adsorption sites for compound formation on the target surface, $x_{RGAinCOMP}$ is the number of reactive-gas atoms per one compound molecule, $\alpha_{RGMtoMEt}$ is the sticking coefficient of the reactive-gas molecules on the metallic part of the target surface, $\alpha_{MEtoCOMP}$ denotes the sticking coefficient of metallic particles on the compound part of the surface, $\gamma_{KnockRGAfromCOMP}$ is the "sputtering" yield of the reactive-gas atoms from the compound in the direction towards the target bottom and Γ_{ME} stands for the flux of thermalized metallic atoms (which is to be evaluated in the same way as Γ_{RGA} employing Eq. 4.31 [p. 56]).

(ix) The composition of the target's "middle" layers, i.e. the layers numbered as j = 2..N-1, is supposed to be given just by the transport of the target-material from the subsurface regions towards the surface due to the target erosion. In accordance with the assumption **(viii)** (p. 58), the target erosion is assumed to be given by the sputtering of the topmost target layer, see Eq. 4.35 (p. 57).

$$n_{st}\dot{\theta}_t^j = \Gamma_{MEsp}\left(\theta_t^{j+1} - \theta_t^j\right) \quad . \qquad (4.38)$$

(x) The composition of the bottommost layer is modeled via these processes: 1) the ionized reactive-gas molecules are supposed to be implanted into this layer with probability $\left(1-\theta_t^N\right)$, otherwise they are not embedded into the target at all and they contribute only to the target sputtering. In addition to

this, 2) the reactive-gas molecules that were "knocked" from the topmost layer contribute to the compound formation in the N-th layer and 3) as target erosion continues the bulk target-material "moves" towards the surface and is being incorporated into the bottommost layer, see the parallel to Eq. 4.38 (p. 58). These three processes are modeled as:

$$n_{st} x_{RGAinCOMP} \dot{\theta}_t^N = \overbrace{\Gamma_{It} \gamma_{KnockRGAfromCOMP} \theta_t^1 \left(1-\theta_t^N\right)}^{\text{RG knocking}} + \overbrace{\Gamma_{RGAft}\left(1-\theta_t^N\right)}^{\text{RG direct implantation}} - \overbrace{\Gamma_{MEsp} x_{RGAinCOMP} \theta_t^N}^{\text{Target erosion}} \quad (4.39)$$

Summing up the fluxes of RG atoms as introduced in the Eqs. 4.37 – 4.39 results in the overall consumption of RG atoms by the target, Q_t, to be

$$Q_t = A_t \left(\overbrace{\Gamma_{RGA} \alpha_{RGMtoMEt} \left(1-\theta_t^1\right)}^{\text{RG sticking}} + \overbrace{\Gamma_{RGAft}\left(1-\theta_t^N\right)}^{\text{RG direct implantation}} - \overbrace{\Gamma_{RGAsp}}^{\text{RG sputtering}} \right) . \quad (4.40)$$

(xi) On the collecting areas, it is supposed that 1) the neutral reactive-gas molecules and the sputtered reactive-gas atoms are adsorbed only at the metallic fraction of the surface and 2) sputtered metallic species are adsorbed on the entire surface, see the assumption **(viii)** (p. 58). Similarly to the target erosion zone, the collecting areas are treated as a homogeneous surface with no spatial variations in the elemental composition and in particle fluxes on it. So, the dynamics of the elemental composition of the collecting areas, $\dot{\theta}_c$, is modeled via the equation

$$n_{sc} x_{RGAinCOMP} \dot{\theta}_c = \overbrace{\Gamma_{RGA} \alpha_{RGMtoMEc} \left(1-\theta_c\right)}^{\text{RG sticking}} + \overbrace{\Gamma_{RGAsp} \frac{A_t}{A_c} \alpha_{RGAsptoMEc} \left(1-\theta_c\right)}^{\text{sticking of sputtered RG}} - \overbrace{\Gamma_{ME} \alpha_{MEtoCOMP} x_{RGAinCOMP} \theta_c}^{\text{sticking of thermalized Me}} - \overbrace{\Gamma_{MEsp} \frac{A_t}{A_c} \alpha_{MEtoCOMP} x_{RGAinCOMP} \theta_c}^{\text{sticking of sputtered Me}} , \quad (4.41)$$

where n_{sc} is the surface density of the adsorption sites for compound formation on the collecting surfaces, $\alpha_{RGMtoMEc}$ and $\alpha_{RGAsptoMEc}$ are the sticking coefficients of the "slow" reactive-gas molecules (i.e. molecules moving with the velocities corresponding to the thermal energies given by the system temperature) and "fast" (i.e. sputtered) reactive-gas atoms, respectively, on the collecting areas. In analogy to Eq. 4.40 (p. 59), the consumption of reactive-gas atoms on the collecting areas, Q_c, is

$$Q_c = A_c \left(\overbrace{\Gamma_{RGA} \alpha_{RGMtoMEc} \left(1-\theta_c\right)}^{\text{RG sticking}} + \overbrace{\Gamma_{RGAsp} \frac{A_t}{A_c} \alpha_{RGAsptoMEc} \left(1-\theta_c\right)}^{\text{sputtered RG adsorption}} \right) , \quad (4.42)$$

Having the equations describing the flux of RG 1) through the gas inlet (Eq. 4.30 [p. 56]) 2) through the pumping outlet (Eq. 4.32 [p. 56]) 3) onto the target (Eq. 4.40 [p. 59]) and 4) onto the collecting areas (Eq. 4.42, [p. 59]), the overall balance equation for reactive-gas atoms is:

$$\dot{N}_{RGA} = Q_f - Q_p - Q_t - Q_c \quad . \tag{4.43}$$

and the balance equation for metallic atoms, N_{ME}:

$$\begin{aligned}\dot{N}_{ME} = {} & \overbrace{A_t \Gamma_{MEsp}}^{\text{Me sputtering}} \overbrace{- A_c \Gamma_{MEsp} \frac{A_t}{A_c}\left(\theta_c \alpha_{MEtoCOMP} + (1-\theta_c)\alpha_{MEtoME}\right)}^{\text{sticking of fast sputtered Me to collecting areas}} - \overbrace{A_p \Gamma_{ME}}^{\text{pumping of thermalized Me}} \\ & \underbrace{- A_t \Gamma_{ME}\left(\theta_t^1 \alpha_{MEtoCOMP} + (1-\theta_t^1)\alpha_{MEtoME}\right)}_{\text{sticking of thermalized Me to target}} \underbrace{- A_c \Gamma_{ME}\left(\theta_c \alpha_{MEtoCOMP} + (1-\theta_c)\alpha_{MEtoME}\right)}_{\text{sticking of thermalized Me to collecting areas}} \quad .\end{aligned} \tag{4.44}$$

At this point, given the flow rate, Q_f, and discharge current, I_d, the set of equations is complete to evaluate all the variables defining the system state, i.e. compound fractions, $\theta_t^{1..N}$, θ_c, the number of reactive-gas atoms in the vessel, N_{RGA}, and the number of thermalized target-material atoms, N_{ME}, therein. The sticking coefficients α_{MEtoME} and $\alpha_{MEtoCOMP}$ were assumed to be equal to unity. As a result, the sum of the first two terms in Eq. 4.44 (p. 60) equals to zero, meaning that all sputtered target-material atoms are adsorbed on the collecting areas. So the value of N_{ME} also equals to zero, and thus, Γ_{ME} was neglected to simplify further calculations.

Solving the set of equations listed above, some additional discharge parameters can be evaluated to investigate the deposition process in more detail. Particularly, the target erosion rate was evaluated as

$$a_E = \overbrace{\Gamma_{MEsp} \frac{1}{n_{sb}}}^{\text{layers sputtered}} \underbrace{\frac{1}{n_{sb}^{0.5}}}_{\text{layer thickness}} \tag{4.45}$$

and used as a measure of deposition rate, a_D. Here, n_{sb} is the surface density of atoms calculated from the target-material's bulk density, ρ, and from the mass, m, of the corresponding ME atom

$$n_{sb} = \left(\frac{\rho}{m}\right)^{2/3} \quad . \tag{4.46}$$

Nevertheless, to explore the behavior of controlled reactive sputtering process, as introduced in Sec. 4.3.3 (p. 51), a coupling of the system state, discharge current and reactive-gas flow must be provided. To do so, an additional assumption was employed:

(xii) The discharge current is influenced by the presence of the compound within the target surface and subsurface layers as follows:

$$I_d = I_d^0 \left(1 + \Delta I_d^{surf} \frac{1}{s} \sum_{j=1}^{s} \theta_t^j + \Delta I_d^{below} \frac{1}{b-s} \sum_{j=s+1}^{b} \theta_t^j \right) \quad . \qquad (4.47)$$

Here, I_d^0 is the discharge current on the "clean" target, i.e. on the target free of any compound. ΔI_d^{surf} and ΔI_d^{below} describe the influence of poisoning of the target's s topmost layers (layers numbered as j = 1..s) and the layers deeper under the target surface (numbered as j = s+1..b; b ≤ N) on the discharge current.

The gas flow control was implemented via the same algorithm as in the case of the real control system, which was depicted in Sec. 4.3.3 (p. 51).

Model of the reactive sputtering process in the steady state

The model of reactive sputtering process was reduced to a steady-state one in order to investigate the performance of the employed control system (described in the preceding paragraphs and in Sec. 4.3.3 [p 51]) and the theoretical performance of the ideal control system that stabilizes the reactive sputtering process in a steady state (I_d and Q_f do not vary throughout the deposition). Then, the respective time-averaged and steady-state values of p_{RG}, θ_c and a_E were compared.

To simplify the analytical solution of the set of model-defining equations, the discharge current I_d was fixed and used as a parameter. So, the steady-state solution of the governing equations is done in the following way:

In the equations defining the process dynamics, i.e. in equations for θ_t^j, j = 1..N, θ_c and N_{RGA}, the time derivatives of the respective variables were set to zero. From the Eq. 4.38 (p. 58) it follows that $\theta_t^j = \theta_t^N$ for j = 2..N-1. Eq. 4.37 (p. 58), i.e. the poisoning of the topmost monolayer on the target's surface, results in

$$\begin{aligned}
0 &= \Gamma_{RGA}\alpha_{RGMtoMEt}\left(1-\theta_t^1\right) + \Gamma_{MEsp} x_{RGAinCOMP}\theta_t^N - \Gamma_{RGAsp} - \Gamma_{It}\gamma_{KnockRGAfromCOMP}\theta_t^1\left(1-\theta_t^N\right) \\
&= \Gamma_{RGA}\alpha_{RGMtoMEt}\left(1-\theta_t^1\right) + \Gamma_{It}\left(\gamma_{MEfromME} + \left(\gamma_{MEfromCOMP} - \gamma_{MEfromME}\right)\theta_t^1\right)x_{RGAinCOMP}\theta_t^N \\
&\quad - \Gamma_{It}\gamma_{RGAfromCOMP}\theta_t^1 - \Gamma_{It}\gamma_{KnockRGAfromCOMP}\theta_t^1\left(1-\theta_t^N\right) \\
&= \Gamma_{RGA}\alpha_{RGMtoMEt} \\
&\quad - \left(\Gamma_{RGA}\alpha_{RGMtoMEt} + \Gamma_{It}\gamma_{RGAfromCOMP} + \Gamma_{It}\gamma_{KnockRGAfromCOMP}\right)\theta_t^1 \\
&\quad + \Gamma_{It}\gamma_{MEfromME} x_{RGAinCOMP}\theta_t^N \\
&\quad + \Gamma_{It}\left(\left(\gamma_{MEfromCOMP} - \gamma_{MEfromME}\right)x_{RGAinCOMP} + \gamma_{KnockRGAfromCOMP}\right)\theta_t^1\theta_t^N \quad .
\end{aligned} \qquad (4.48)$$

and Eq. 4.39 (p. 59),i.e. the poisoning of the N-th layer on the target's surface takes the form

$$\begin{aligned}
0 &= \Gamma_{It}\gamma_{KnockRGAfromCOMP}\theta_t^1\left(1-\theta_t^N\right)+\Gamma_{RGAft}\left(1-\theta_t^N\right)-\Gamma_{MEsp}x_{RGAinCOMP}\theta_t^N \\
&= \Gamma_{It}\gamma_{KnockRGAfromCOMP}\theta_t^1\left(1-\theta_t^N\right)+\Gamma_{RGAft}\left(1-\theta_t^N\right) \\
&\quad -\Gamma_{It}\left(\gamma_{MEfromME}+\left(\gamma_{MEfromCOMP}-\gamma_{MEfromME}\right)\theta_t^1\right)x_{RGAinCOMP}\theta_t^N \\
&= \Gamma_{RGAft}+\Gamma_{It}\gamma_{KnockRGAfromCOMP}\theta_t^1 \\
&\quad -\left(\Gamma_{RGft}+\Gamma_{It}\gamma_{MEfromME}x_{RGAinCOMP}\right)\theta_t^N \\
&\quad -\Gamma_{It}\left(\left(\gamma_{MEfromCOMP}-\gamma_{MEfromME}\right)x_{RGAinCOMP}+\gamma_{KnockRGAfromCOMP}\right)\theta_t^1\theta_t^N
\end{aligned} \quad (4.49)$$

Clearly, Eq. 4.48 (p. 61) and Eq. 4.49 (p. 62) can be used to evaluate θ_t^j, j = 1..N, values as functions of Γ_{RGA} and I_d. Since Γ_{RGA}, N_{RG}, p_{RG} are coupled, see Eq. 4.31 (p. 56), the target poisoning is a function of p_{RG} and I_d. Adding Eq. 4.48 (p. 61) and Eq. 4.49 (p. 62) provides

$$0=\Gamma_{RGAft}+\Gamma_{RGA}\alpha_{RGMtoMEt}-\left(\Gamma_{RGA}\alpha_{RGMtoMEt}+\Gamma_{It}\gamma_{RGAfromCOMP}\right)\theta_t^1-\Gamma_{RGAft}\theta_t^N \quad , \quad (4.50)$$

which can be rearranged as

$$0=\Gamma_{RGA}\alpha_{RGMtoMEt}\left(1-\theta_t^1\right)+\Gamma_{RGAft}\left(1-\theta_t^N\right)-\Gamma_{It}\gamma_{RGAfromCOMP}\theta_t^1 \quad , \quad (4.51)$$

describing the target balance in the steady state, see Eq. 4.40 (p. 59). In other words, Eq. 4.51 (p. 62) is a particular example of a general claim – in the steady state, the number of RG atoms that are being incorporated into the target (in the form of neutral molecules, molecular ions etc.) and the number of RG atoms leaving it (in the form of sputtered neutral atoms, ions etc.) are the same. Solving Eq. 4.51 (p. 62) for θ_t^1 gives

$$\theta_t^1=\frac{\Gamma_{RGAft}+\Gamma_{RGA}^{RG}\alpha_{RGMtoMEt}-\Gamma_{RGAft}\theta_t^N}{\Gamma_{RGA}\alpha_{RGMtoMEt}+\Gamma_{It}\gamma_{RGAfromCOMP}} \quad . \quad (4.52)$$

Denoting

$$
\begin{aligned}
K_1 &= \frac{\Gamma_{RGAft} + \Gamma_{RGA}\alpha_{RGMtoMEt}}{\Gamma_{RGA}\alpha_{RGMtoMEt} + \Gamma_{It}\gamma_{RGAfromCOMP}} \\
K_2 &= \frac{\Gamma_{RGAft}}{\Gamma_{RGA}\alpha_{RGMtoMEt} + \Gamma_{It}\gamma_{RGAfromCOMP}} \\
K_3 &= \Gamma_{RGAft} \\
K_4 &= \Gamma_{It}\gamma_{KnockRGAfromCOMP} \\
K_5 &= \Gamma_{RGAft} + \Gamma_{It}\gamma_{MEfromME}\, x_{RGAinCOMP} \\
K_6 &= \Gamma_{It}\left(\gamma_{KnockRGAfromCOMP} + \left(\gamma_{MEfromCOMP} - \gamma_{MEfromME}\right)x_{RGAinCOMP}\right)
\end{aligned}
\tag{4.53}
$$

allows us to write Eq. 4.52 (p. 62) and Eq. 4.49 (p. 62) as

$$
\begin{aligned}
\theta_t^1 &= K_1 - K_2\theta_t^N \\
0 &= K_3 + K_4\theta_t^1 - K_5\theta_t^N - K_6\theta_t^1\theta_t^N \quad .
\end{aligned}
\tag{4.54}
$$

After substituting for θ_t^1, the quadratic equation for θ_t^N

$$
0 = K_3 + K_1K_4 - \left(K_2K_4 + K_5 + K_1K_6\right)\theta_t^N + K_2K_6\theta_t^N\theta_t^N \quad , \tag{4.55}
$$

is solved and, subsequently, θ_t^1 is evaluated. Note that the θ_t^N and θ_t^1 are functions of p_{RG}, see Eq. 4.31 (p. 56), and I_d, i.e. $\theta_t^1(p_{RG}, I_d)$ and $\theta_t^N(p_{RG}, I_d)$.

In the same way, Eq. 4.41 (p. 59) in a steady state

$$
\begin{aligned}
0 = {} & \Gamma_{RGA}\alpha_{RGMtoMEc}\left(1-\theta_c\right) + \Gamma_{RGAsp}\frac{A_t}{A_c}\alpha_{RGAsptoMEc}\left(1-\theta_c\right) \\
& - \Gamma_{MEsp}\frac{A_t}{A_c}\alpha_{MEtoCOMP}\, x_{RGAinCOMP}\,\theta_c \quad ,
\end{aligned}
\tag{4.56}
$$

is solved for θ_c resulting in

$$
\theta_c = \frac{\Gamma_{RGA}\alpha_{RGMtoMEc} + \Gamma_{RGAsp}\frac{A_t}{A_c}\alpha_{RGAsptoMEc}}{\Gamma_{RGA}\alpha_{RGMtoMEc} + \Gamma_{RGAsp}\frac{A_t}{A_c}\alpha_{RGAsptoMEc} + \Gamma_{MEsp}\frac{A_t}{A_c}\alpha_{MEtoCOMP}\, x_{RGAinCOMP}} \quad , \tag{4.57}
$$

where Γ_{RGAsp} and Γ_{MEsp} are both functions of I_d and θ_t^1, i.e. $\theta_c(p_{RG}, I_d)$.

At this point, θ_t^1, θ_t^N ($\theta_t^j = \theta_t^N$, for j = 2..N-1) and Θ_c are expressed as functions of p_{RG} and I_d. Knowing Θ_c, the consumption of the reactive gas on the collecting areas, Q_c, is calculated from Eq. 4.42 (p. 59) and the reactive-gas flow rate into the chamber, Q_f, is evaluated using the steady-state form of Eq. 4.43 (p. 60). In the steady state, the net consumption of the reactive gas by the target surface, Q_t, is zero, see the Eq. 4.51 (p. 62). The pumping speed, Q_p, is given just by the reactive-gas pressure, p_{RG}, and the area of the pumping outlet, A_p. Recapitulating all these interdependencies, Q_f is a function of p_{RG} and I_d

$$Q_f = Q_c(I_d, p_{RG}) + Q_p(p_{RG}) \quad . \tag{4.58}$$

In practice, it is advantageous to present the p_{RG}, θ_t^1, θ_t^N, Θ_c, Q_c and Q_p as functions of Q_f for Q_f is the only independent parameter used to control the sputtering process (I_d is a fixed parameter of the model). The transformation of all the above mentioned variables, $f(p_{RG}) \rightarrow f(Q_f)$, was done by solving the Eqs. in this sequence – Eq. 4.55 (p. 63), Eq. 4.52 (p. 62), Eq. 4.57 (p. 63) and Eq. 4.58 (p. 64) for the set of particular values of p_{RG}. So, the vectors of solutions θ_t^1, θ_t^N, θ_c, Q_c and Q_f are obtained corresponding to particular values of the input parameter, p_{RG}. Subsequently, the values of Q_f were used to substitute the corresponding values of p_{RG} when presenting the values of θ_t^1, θ_t^N, θ_c and Q_c.

4.6.2 Setting the parameters of the model

The input parameters of the model can be divided into several groups:

Geometry of the deposition system

The volume of the vacuum chamber, V, was readily calculated knowing the system dimensions. The area of collecting surfaces, A_c was assumed to be smaller than the inner surface of the chamber because the flux of sputtered atoms is not homogeneous causing only a part of collecting areas to be exposed to the flux of the sputtered target-material. Target area, A_t, was estimated to be the area of the target erosion zone. The area of the pumping outlet, A_p, was evaluated using the balance between the flow rate of the BG, $Q_f(Ar)$, into the chamber and the pumping speed of the BG, $Q_p(Ar)$. Combining the Eq. 4.30 (p. 56), Eq. 4.31 (p. 56) and Eq. 4.32 (p. 56) results in:

$$A_p = \frac{Q_p}{\Gamma_{BG}} = \frac{Q_f}{\Gamma_{BG}} = \frac{q_f}{p_{BG}} k_{qsccm} (2\pi k T m_{BG})^{0.5} \quad , \tag{4.59}$$

where q_f is the flow rate of the BG into the vacuum vessel in the units of sccm and p_{BG} is the partial pressure.

Sputtering yields

The sputtering yield of the target-material (Zr) from the metallic part of the target, $\gamma_{MEfromME}$, was calculated for several values of the energy of the incident ion (Ar^+ or Zr^+) using the TRIM code, see Fig. 5.12 (p. 86). Taking into account the backward flux of ionized sputtered species, the value of $\gamma_{MEfromME}$ was set to be 50% of the calculated one. The sputtering yield of the target-material atoms from the compound fraction of the target, $\gamma_{MEfromCOMP}$, and the "knocking" of the reactive-gas atoms deeper into the target, $\gamma_{KnockRGAfromCOMP}$, were considered to be lower of factor of 10 as compared to $\gamma_{MEfromME}$. The sputtering yield of reactive-gas atoms from the compound, $\gamma_{RGAfromCOMP}$, was estimated to be 40% of $\gamma_{MEfromME}$.

Surface properties

All the particle-surface interactions (including the compound formation) were modeled via respective sticking coefficients, α, ranging from 0 to 1, meaning that the sticking coefficient equal to 1 represents 100% sticking probability or 100% probability of a chemical reaction to run. Sticking coefficients of metallic particles to metallic surfaces, α_{MEtoME}, and compound surfaces, $\alpha_{MEtoCOMP}$, were set equal to 1 as well as the sticking coefficient of sputtered reactive-gas atoms on the metallic parts of the collecting areas, $\alpha_{RGAsptoMEc}$. On the other hand, the adherence of the reactive-gas species to the metallic part of the target, $\alpha_{RGMtoMEt}$, and collecting areas $\alpha_{RGMtoMEc}$ were assumed to be lower and the sticking of reactive-gas species to the compound fractions of the surfaces is neglected at all.

As the dynamics of the system was investigated, the surface densities of the adsorption sites on the target surface, n_{st}, and on the collecting surfaces, n_{sc}, were revealed to play crucial role. The surface density of atoms, n_{sb}, as evaluated in Eq. 4.46 (p. 60) using the bulk properties of the target-material, served as a rough estimation of the minima of both n_{st} and n_{sc}. Nevertheless, the experiment described below was performed to make the estimation of n_{st} and n_{sc} more precise.

Consider a vacuum chamber with an inner active surface, A, covered by adsorption sites of surface density n_s. Then, the number of the adsorption sites is $N_s = n_s A$. As the compound-free target is being sputtered in non-reactive atmosphere, the number of non-reacted, i.e. "free", adsorption sites, N_{sf}, attains the value of N_s according to the equation

$$\dot{N}_{sf} = \frac{N_s - N_{sf}}{N_s} \times \frac{I_d \gamma_{MeFromMe}}{e} \quad . \tag{4.60}$$

Here, e , $e > 0$, is the elementary charge. Solving the Eq. 4.60 for $N_{sf}(t)$ and setting $N_{sf}(0) = 0$ (meaning that the collecting areas are fully covered in the time the sputtering starts) provides:

$$N_{sf}(t_{sp}) = N_s \left(1 - \exp\left(-\frac{I_d \gamma_{MeFromMe}}{eN_s} t_{sp}\right)\right) \quad . \tag{4.61}$$

Knowing the discharge current, I_d, sputtering time, t_{sp}, and the sputtering yield, $\gamma_{MEfromME}$, the number of adsorption sites, N_s, remains the only parameter in Eq. 4.61. As the sputtering is stopped and the reactive gas is introduced into the chamber at a flow rate of Q_f , it takes some time, t_{delay}, to detect a pressure increase since the sputtered metal getters the reactive gas. Apparently, the number of covered adsorption sites is

$$N_{sf}(t_{sp}) = Q_f t_{delay} \quad , \tag{4.62}$$

which was utilized to make a numerical fit of N_s using Eq. 4.61 (p. 66). Practically, the sputtering cycle was repeated several times for different t_{sp} and the corresponding values of t_{delay} were recorded, see Fig. 5.28 (p. 109). After that, the best fit of N_s was assessed, see Fig. 5.29 (p. 109).

Particle properties

The ionization probabilities of particular gaseous species, β_{RG} and β_{BG}, are to be set to evaluate the magnitudes of ionic fluxes of respective species onto the target, see Eq. 4.34 (p. 57). Since these are only relative values, the probability of ionization of reactive gas was set to be 3 times higher than that of the background gas.

Discharge properties

In the model, $\Delta I_d^{surf} < 0$ and $\Delta I_d^{below} > 0$ were used, see Eq. 4.47 (p. 61), which means that (i) the presence of the oxygen within the topmost target layers causes a decrease in I_d through the cumulative effect of ion- and electron-induced electron emission and reflection of electrons from the target surface, (ii) I_d is increased as a consequence of the presence of the oxygen within the subsurface regions of the target [81-84,86]. The layers indexed as 1 and 2 were considered to be the "surface" ones and the layers indexed as 3 – 5 were set to be the "subsurface" ones. So, the parameters s and b in Eq. 4.47 (p. 61) were 2 and 5, respectively.

5 Results and discussion

In this chapter, the results of the deposition experiments, diagnostics and mathematical modeling of high-power impulse magnetron sputtering (HiPIMS) of zirconium (Zr) and controlled reactive HiPIMS of zirconium oxides (ZrO_x) are presented. The sputter-deposition process of Zr was investigated by analyzing the influence of the target power density on the discharge characteristics and deposition characteristics. Furthermore, ion fluxes at the substrate position were explored by mass spectrometry. Then, the phenomenological model of the deposition process was employed to support the elucidation of the results (Sec. 5.1 [p. 67]). The reactive sputter-deposition process was studied by the same means (i.e. investigation of discharge characteristics, deposition characteristics and substrate ion fluxes), but the target power density was fixed and the influence of the controller settings on the above mentioned properties and on the properties of deposited ZrO_x films were explored (Sec. 5.2 [p. 93]). After that, ZrO_x films were deposited under various conditions and the film properties were analyzed in detail (Sec. 5.3 [p. 102]). Finally, the mathematical model was used to help to clarify the complicated deposition processes and to investigate the performance of the controller used to operate the reactive sputtering process (Sec. 5.4 [p. 107]).

5.1 HiPIMS depositions of zirconium

To deepen the understanding of the HiPIMS deposition of pure metallic films, four sets of sputtering experiments in argon gas were performed: **(i)** the average target power density in a period was increased ($\overline{S}_d$ = 5 – 103 Wcm^{-2}) at a constant high-power pulse duration t_1 = 200 μs, **(ii)** target power density was increased (S_{da} = 900 – 2240 Wcm^{-2}) in shortened pulses (from 200 μs to 80 μs) at a constant average target power density in a period $\overline{S}_d$ = 100 ± 3 Wcm^{-2}, **(iii)** target power density was increased (S_{da} = 458 – 3405 Wcm^{-2}) in shortened pulses (from 200 μs to 20 μs) at a constant average target power density in a period $\overline{S}_d$ = 45 ± 5 Wcm^{-2} and **(iv)** the pulse duration was shortened (from 100 μs to 10 μs) at a constant discharge voltage in a pulse U_{da} = 910 ± 15 V.

We investigated the effect of all of the above mentioned changes on **(i)** the discharge characteristics (Fig. 5.1 [p. 68], Fig. 5.2 [p. 69], Fig. 5.3 [p. 70] and Fig. 5.4 [p. 73]), **(ii)** ion energy distributions (Fig. 5.5 [p. 75] and Fig. 5.8 [p. 82]) **(iii)** ion flux compositions (Fig. 5.6 [p. 76], Fig. 5.7 [p. 79], Fig. 5.9 [p. 83], Table 5.1 [p. 80], Table 5.2 [p. 81] and Table 5.3 [p. 83]). In the case of the first two sets of experiments (increasing $\overline{S}_d$ at constant t_1 and increasing S_{da} at constant $\overline{S}_d$), also the deposition characteristics were studied (Fig. 5.10 [p. 84]). Moreover, we carried out model calculations to explain the particular stages of the complicated deposition processes (Fig. 5.11 [p. 86], Fig. 5.12 [p. 86], Fig. 5.13 [p. 87], Fig. 5.14 [p. 88], Fig. 5.15 [p. 90] and Fig. 5.16 [p. 91]). Note that the pulse repetition frequency was 500 Hz in all the experiments and that the value of the average pulse target power density S_{da} = 35 Wcm^{-2}, corresponding to the minimum value of $\overline{S}_d$ = 5 Wcm^{-2} used in this work, is relatively close to the values of the target power density applied in conventional DC magnetron sputtering discharges.

5.1.1 Discharge characteristics

In this section, the time evolutions (waveforms) of the magnetron voltage, $U_d(t)$, the target current density, $J_t(t)$, and the substrate current density, $J_s(t)$, are discussed since they provide information on the absorption of energy and the efficiency of the ionization processes in the discharge plasma, and on the transfer of the arising ions to the target and to the substrate in the strongly unbalanced magnetron system used.

Fig. 5.1 (p. 68) shows the waveforms of U_d, J_t and J_s for the preset average target power densities in a period $\overline{S}_d$ = 5 Wcm^{-2} and 103 Wcm^{-2} at a voltage pulse duration t_1 = 200 μs with the corresponding average pulse target power densities S_{da} = 35 Wcm^{-2} and 970 Wcm^{-2}, respectively, and $\overline{S}_d$ = 103 Wcm^{-2} at t_1 = 80 μs with the corresponding value S_{da} = 2.22 kWcm^{-2}. The maximum target power density was about 2.70 kWcm^{-2} for $\overline{S}_d$ = 103 Wcm^{-2} and t_1 = 80 μs, i.e., for the duty cycle t_1/T = 4%. Note that the target current density, J_t, decreased under 0.02 Acm^{-2} in the times of 15 μs to 45 μs after termination of the high-power pulse for all the pulses investigated (all the discharge regimes are listed in Table 5.1 [p. 80], Table 5.2 [p. 81] and Table 5.3 [p. 83]).

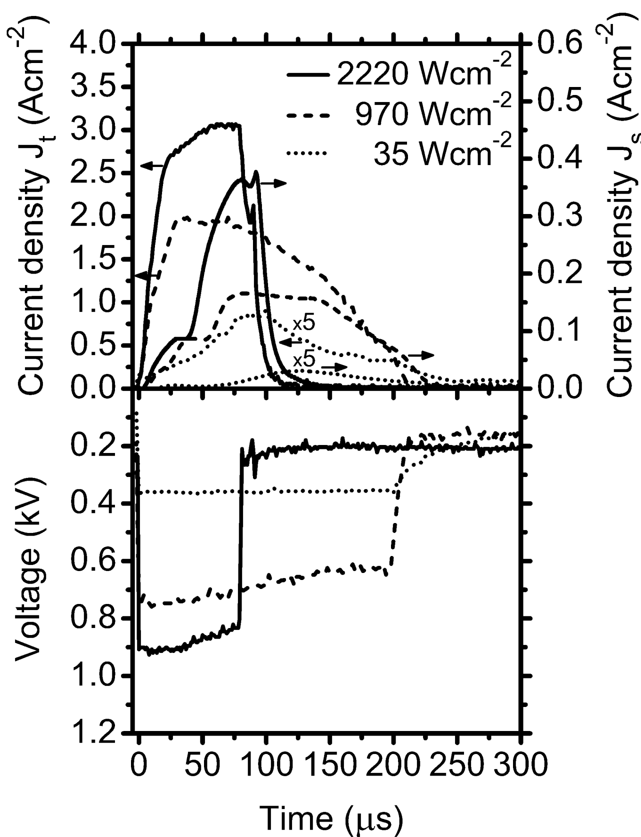

Fig. 5.1
Waveforms of the magnetron voltage, U_d, the target current density, J_t, and the substrate current density, J_s, for the preset average target power densities in a period $\overline{S}_d$ = 5 Wcm^{-2} and 103 Wcm^{-2} at a voltage pulse duration t_1 = 200 μs with the corresponding average pulse target power densities S_{da} = 35 Wcm^{-2} and 970 Wcm^{-2}, respectively, and $\overline{S}_d$ = 103 Wcm^{-2} at t_1 = 80 μs with the corresponding value of S_{da} = 2220 Wcm^{-2}. The substrate was at a distance of d = 100 mm.
Experimental conditions: pulsed DC discharge, repetition frequency f_r = 500 Hz, argon process-gas pressure p = 1 Pa, target-to-substrate distance d = 100 mm. See Table 5.1 (p. 80).

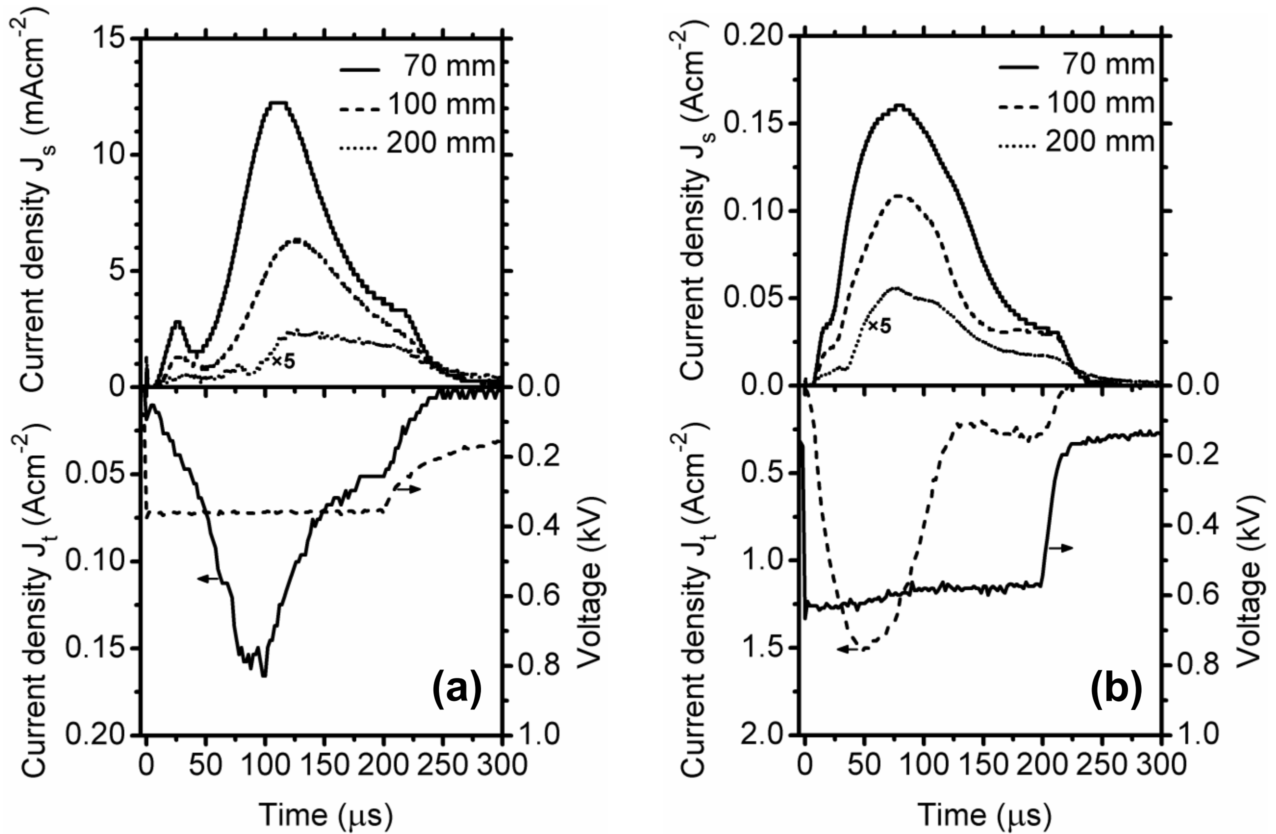

Fig. 5.2

Waveforms of the magnetron voltage, U_d, the target current density, J_t, and the substrate current density, J_s, for a preset average target power densities in a period **(a)** $\overline{S}_d$ = 5 Wcm^{-2} (S_{da} = 35 ± 2 Wcm^{-2}) and **(b)** $\overline{S}_d$ = 50 Wcm^{-2} (S_{da} = 440 ± 10 Wcm^{-2}) at a voltage pulse duration t_1 = 200 μs, see Table 5.1 (p. 80). The slope of the J_t waveform was higher for the regime with higher S_{da} and the maximum in J_t was attained 50 μs after the pulse startup in the cases of $S_{da} \approx$ 440 Wcm^{-2} and 100 μs in the cases of $S_{da} \approx$ 35 Wcm^{-2} as the value of U_{da} rose from approx. 380 V to 590 V. The ionic flux was increased by more than factor of 10 as the $\overline{S}_d$ value increased from 5 Wcm^{-2} to 50 Wcm^{-2}.

Experimental conditions: pulsed DC discharge, repetition frequency f_r = 500 Hz, argon process-gas pressure p = 1 Pa.

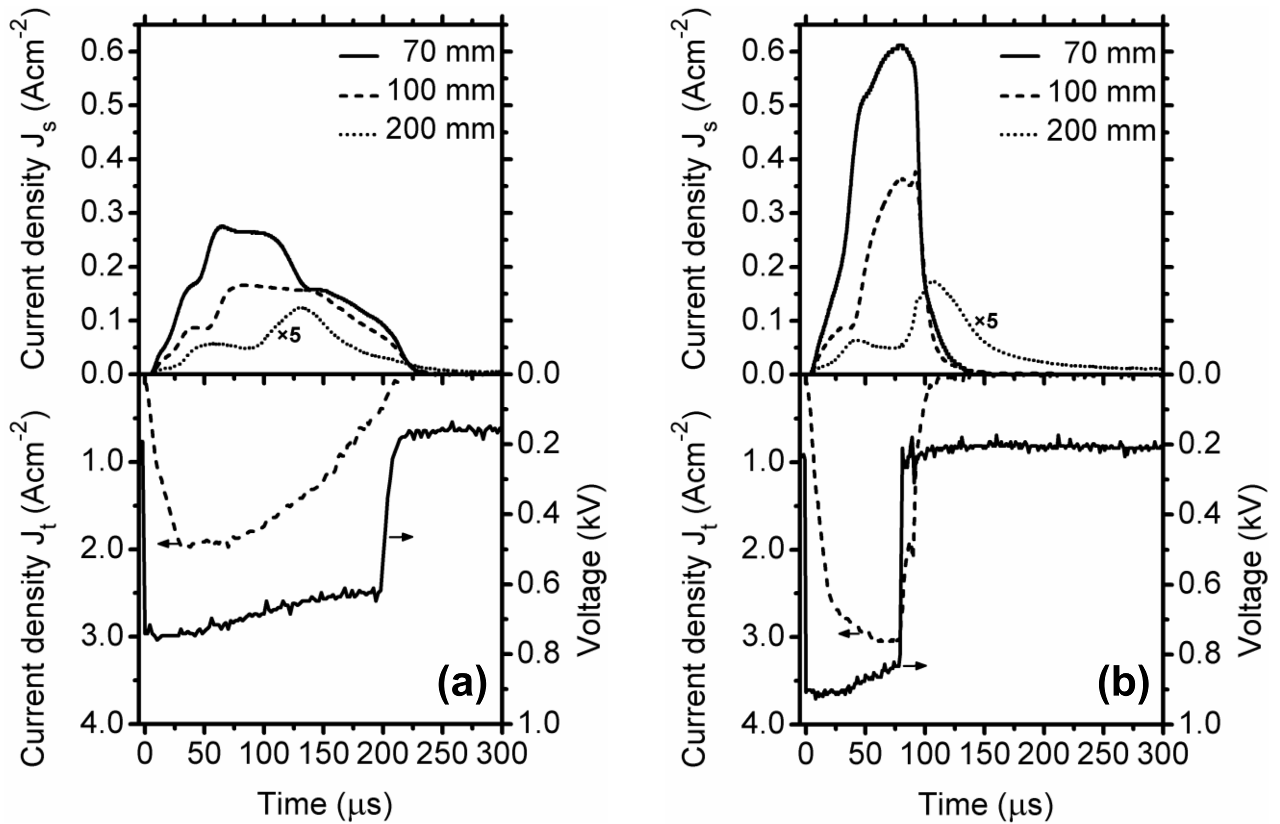

Fig. 5.3

Waveforms of the magnetron voltage, U_d, the target current density, J_t, and the substrate current density, J_s, for a preset average target power density in a period $\overline{S}_d$ = 100 Wcm^{-2} and at a voltage pulse duration **(a)** t_1 = 200 µs (S_{da} = 960 ± 10 Wcm^{-2}) and **(b)** t_1 = 80 µs (S_{da} = 2220 ± 10 Wcm^{-2}), see Table 5.1 (p. 80). The maximum in J_t was attained 50 µs after the pulse startup for both pulse durations. The waveform of J_s reached its maxima at different times for different distances from the target, as opposed to the regime with $\overline{S}_d$ = 50 Wcm^{-2} (Fig. 5.2(b) [p. 69]), indicating that the mechanism of propagation of ions in the direction from the target changed with rising S_{da}.

Experimental conditions: pulsed DC discharge, repetition frequency f_r = 500 Hz, argon process-gas pressure p = 1 Pa.

In Fig. 5.2 (p. 69), the information on substrate currents at distances of 70 mm, 100 mm and 200 mm from the target is presented for two discharge regimes (a) $\overline{S}_d$ = 5 Wcm^{-2} (S_{da} = 35 ± 2 Wcm^{-2}) and (b) $\overline{S}_d$ = 50 Wcm^{-2}, (S_{da} = 440 ± 10 Wcm^{-2}), see Table 5.1 (p. 80). Apparently, the slope of J_t waveform was much higher for the regime with higher S_{da} and the maximum in J_t was attained earlier after the pulse startup (50 µs in the cases of S_{da} ≈ 440 Wcm^{-2}, 100 µs in the cases of S_{da} ≈ 35 Wcm^{-2}) as the value of U_{da} rose from approx. 380 V to 590 V. As expected, the ionic flux was increased by more than factor of 10 as the $\overline{S}_d$ value increased from 5 to 50 Wcm^{-2}. Nevertheless the main peak of the substrate current density, J_s, occured almost in the same time in all distances for both the regimes. In the regime with S_{da} = 450 Wcm^{-2}, Fig. 5.2(b) (p. 69), J_t exhibits a two-peak shape indicating that a steady state of the discharge is not attained after 200 µs from the pulse beginning as well as in the regime with S_{da} = 35 Wcm^{-2}, Fig. 5.2(a) (p. 69) [4,34,36].

The effect of an increased $\overline{S}_d$ from 50 to 100 Wcm^{-2} at a constant t_l = 200 µs is expressed by comparison of Fig. 5.3(a) (p. 70) and Fig. 5.2(b) (p. 69). For the S_{da} = 960 ± 10 Wcm^{-2} regime, Fig. 5.3(a) (p. 70), the waveform of J_s became more complicated and J_s reached its maxima at different times for different distances from the target, indicating that the mechanism of propagation of ions in the direction from the target changed with rising S_{da}. Shortening the pulse-on time from 200 µs to 80 µs at a constant $\overline{S}_d$ = 103 Wcm^{-2}, as shown in the Fig. 5.3(b) (p. 70), caused no new effects as far as the J_t and J_s waveforms are considered.

Some general features in the waveforms of J_t and J_s are to be found. Considering J_t and pulse-on times exceeding 100 µs a rapid rise in J_t is followed by a decrease in its magnitude. There are multiple causes for such a behavior: (i) U_d slightly decreases throughout the pulse due to limited power supply capabilities, (ii) the process gas in front of the magnetron is rarefied due to the 'sputtering wind' phenomena, as mentioned in Sec. 2.1 (p. 8) and in Refs. [35-37,121], (iii) the losses of charged particles from the region adjacent to the erosion zone are rising as J_t increases [62,76], (iv) the sputtered metallic particles, having lower excitation and ionization potentials in comparison with the Ar process-gas atoms, cause the "cooling" of the electrons resulting in a decrease in ionization efficiency, (v) the magnetron target itself acts as an "ion pump" reducing the background-gas number density in front of it.

The latter entry in the preceeding list is to be explained as follows: Ionized species are attracted towards the magnetron target. They are of high velocity and some of them are "knocked" into the target surface. Subsequently, some of the gas species that were "knocked" are sputtered. The velocity of sputtered particles is much higher than the thermal velocity of gas species. As a result, the number density of gas species is reduced in front of the target.

The effect of gas rarefaction due to the ‘sputtering wind’ can be quantified by the probability, P, of the gas species not to be hit by the sputtered species within the time interval of duration t. The formula

$$P = \exp\left(-\Gamma_{sp}\sigma t\right) \qquad (5.1)$$

was used. Here σ is the cross-section for the elastic collision of process-gas molecule and sputtered metallic atom, and Γ_{sp} is the flux of sputtered particles which was assessed as $\Gamma_{sp} = \gamma_{sp}\Gamma_{It} = \gamma_{sp} I_d/(eA_{er})$, where Γ_{It} is the flux of ions onto the target, e, $e > 0$, is the elementary charge, γ_{sp} is the sputtering yield of the target-material and A_{er} is the area of the target erosion zone, see Eq. 4.33 (p. 57). Then, the mean time between the collision of the process-gas molecule and the sputtered metallic atom is $t_{coll} = \dfrac{eA_{er}}{I_d \gamma_{sp} \sigma}$.

The dilution of the process gas by the “target pumping” can be assessed by evaluating the time, t_{pump}, required to “pump” the process-gas from the volume, V_t, above the target erosion zone. Employing the formula

$$t_{pump} = \frac{\overbrace{n_{BG} V_t}^{\text{number of BG species in the volume Vt}}}{\underbrace{\Gamma_{It} A_{er}}_{\text{magnetron "pumping" of BG}} - \underbrace{\Gamma_{BG} A_{er}}_{\text{thermal flux of BG into the volume Vt}}} = \frac{p_{BG} V_t}{kT\left(\dfrac{I_d}{eA_{er}} - \dfrac{1}{4} n_{BG} \bar{v}_{BG}\right) A_{er}} = \frac{p_{BG} V_t}{\left(I_d \dfrac{kT}{e} - p_{BG}\left(\dfrac{kT}{2\pi m_{BG}}\right)^{0.5} A_{er}\right)}, \qquad (5.2)$$

where p_{BG}, n_{BG}, Γ_{BG}, $\bar{v}_{BG}$ and m_{BG} stand for the pressure, number density, flux density, mean thermal velocity and the mass of the process-gas species. Note that an influence of the flux of the ionized sputtered target-material atoms was neglected.

Setting A_{er} = 50 cm^2, σ = 3×10^{-16} cm^2, γ_{sp} = 0.7, V_t = 50 cm^3, p_{BG} = 1Pa, m_{BG} = 40 u, T = 400 K, I_d = 100 A, one obtains $t_{coll} \approx$ 40 µs and $t_{pump} \approx$ 20 µs, giving time scales which are in a good agreement with the measured data. However, for the discharge regimes with $I_d \approx$ 10 A, the calculations predict longer time scales than observed, indicating that a more detailed study of the ionization and particle loss mechanisms is needed.

Regarding J_s, the change in the slopes of the respective waveforms is observed at all the discharge regimes after approximately 30 µs after the startup of the U_d pulse. As S_{da} rises to values higher than

approximately 1 $kWcm^{-2}$, the time delay of maxima in J_s after the maxima in J_t is reached becomes longer with increasing target-to-probe distance (compare the respective waveforms of J_s in Fig. 5.2 [p. 69] and in Fig. 5.3 [p. 70]).

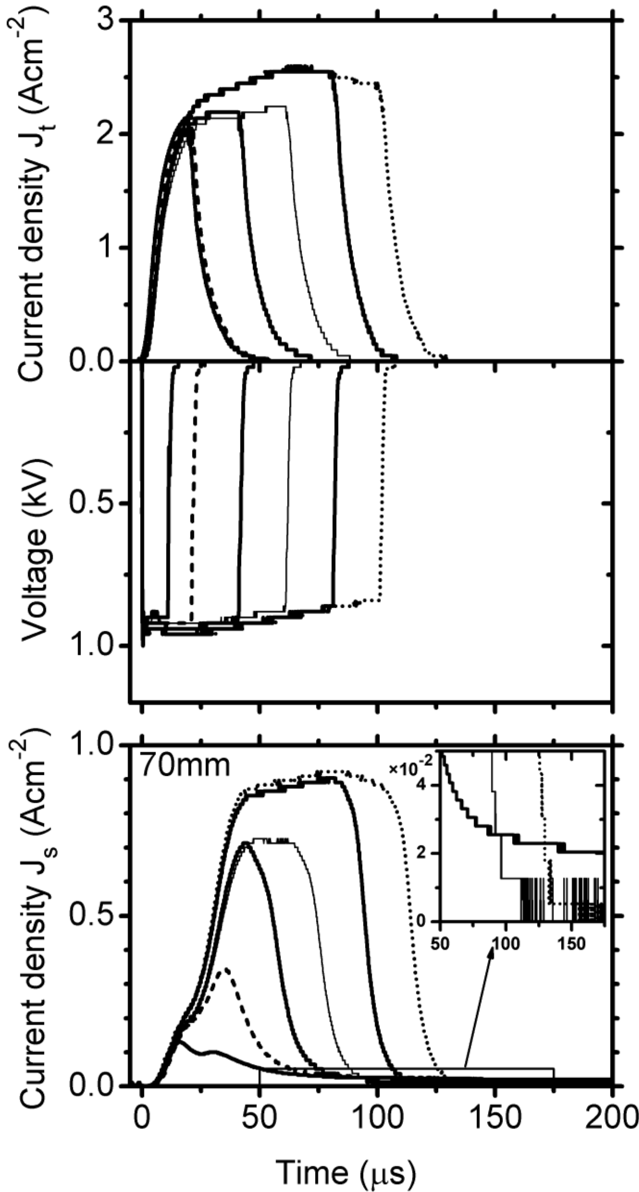

Fig. 5.4
Shortening the pulse-on time at fixed value of discharge voltage, U_{da}. The value of U_{da} was set to 910 ± 15 V to attain average target power density in a period, $\overline{S}_d$ = 103 Wcm^{-2} at t_l = 100 μs and kept constant, while the pulse was shortened down to t_l = 10 μs (Table 5.3 [p. 83]). The waveforms of target current density, J_t, exhibited a rapid rise and for $t_l \geq 40$ μs a plateau in J_t was reached. Selection in upper right hand corner of the bottommost figure shows that the decay of the substrate current density, J_s, is slower for the regimes with shorter t_l
Experimental conditions: Pulsed DC discharge, repetition frequency f_r = 500 Hz, argon process-gas pressure p = 1 Pa, target-to-probe distance d = 70 mm. See Table 5.3 (p. 83).

Shortening the pulse-on time at a constant value of U_{da} provides information on the time evolution of J_t and J_s and on the composition of the ion flux onto the target within a pulse. Discharge characteristics of such an experiment are presented in Fig. 5.4 (p. 73). The value of U_{da} was set to 910 ± 15 V to attain the $\overline{S}_d$ = 103 Wcm^{-2} at t_l = 100 μs and kept constant, while the pulse was shortened down to t_l = 10 μs (Table 5.3 [p. 83]). The waveforms of J_t exhibited a rapid rise and for $t_l \geq 40$ μs a plateau in J_t was reached. However, similarly to the other discharge regimes investigated, even the time t_l = 100 μs is not

long enough to reach a steady state of the sputtering discharge. A closer look at J_s waveforms in Fig. 5.4 (p. 73) reveals that the decay of J_s is slower for the regimes with shorter t_1. Putting all these facts together with the information on IEDFs (Fig. 5.5 [p. 75] and Fig. 5.8 [p. 82]) and on the composition of the total ion flux (Fig. 5.9 [p. 83] and Table 5.3 [p. 83]) it can be stated that as the value of U_{da} was fixed, decreasing t_1 (i) lowered the fraction of Zr ions in the total ion flux on the probe located in the distance of 70 mm from the target, (ii) lowered the average kinetic energy of ions and (iii) lowered the rarefaction of the gas in the region between the target and the probe resulting in higher scattering and possibly higher amount of Ar ions in this space domain (Ar ions are assumed to effectively ionize the Zr atoms via charge-exchange processes, see the discussion in Sec. 5.1.2 [p. 74]). Then, we can claim that for a shorter t_1 the ions striking the substrate are (i) of lower velocity, (ii) more scattered and (iii) ionized also in the afterglow phase of the discharge. These three points can explain the slower decay of J_s for a shorter t_1.

5.1.2 Ion energies and compositions of total ion fluxes

Fig. 5.5 (p. 75) and Fig. 5.8 (p. 82) show the time-averaged energy distributions of Zr^+, Zr^{2+}, Ar^+ and Ar^{2+} ions measured at the substrate positions of 100 mm (Fig. 5.5 [p. 75]) and 70 mm from the target (Fig. 5.8 [p. 82]). It should be mentioned that the corresponding contributions from Zr^{3+} ions were approximately 500 times lower compared with the Zr^{2+} ions. The maxima of all the energy distributions in Fig. 5.5 (p. 75) and Fig. 5.8 (p. 82) are related to thermalized ions produced at the plasma potential [122]. Therefore, the corresponding energies (measured with respect to the ground potential) for the doubly charged ions are two times higher than for the singly charged ions. The plasma potential is close to the ground potential due to the strong unbalance of the magnetron used, prolonging a residence time of electrons in the discharge plasma.

The ions detected with energies lower than 0 eV (Fig. 5.5 [p. 75] and Fig. 5.8 [p. 82]) may have originated by ionization at a negative potential in the plasma sheath adjacent to the extraction electrode of the mass spectrometer. Alternatively, these may be ions with a positive energy which lose their kinetic energy in collisions after being accelerated in the plasma sheath by the extraction potential. For more details see Sec. 4.1.6 (p. 40) and Fig. 4.15 (p. 42). At the high value of $\overline{S}_d$ = 103 Wcm^{-2}, the ion energy distributions are extended to high energies (up to 100 eV relative to the ground potential). The high-energy tail of the ion energy distributions (shown only up to 50 eV in Fig. 5.5 [p. 75] and Fig. 5.8 [p. 82]) is more pronounced for the longer pulse duration t_1 = 200 μs. The fractions of the Zr^+ and Ar^+ ions with energies of 10 eV – 100 eV being 21% and 3%, respectively, for t_1 = 200 μs decreased 1.3 and 3.3 times, respectively, for t_1 = 80 μs. The respective fractions of the Zr^{2+} and Ar^{2+} ions with energies of 20 eV – 100 eV being 15% and 6% for t_1 = 200 μs decreased approximately 3 times for t_1 = 80 μs. Let us recall that a high occurrence of the metallic ions with an increased kinetic energy in the flux onto the substrate could provide beneficial effects on microstructure and properties of the films deposited even on a floating substrate, i.e. without a negative substrate bias [9].

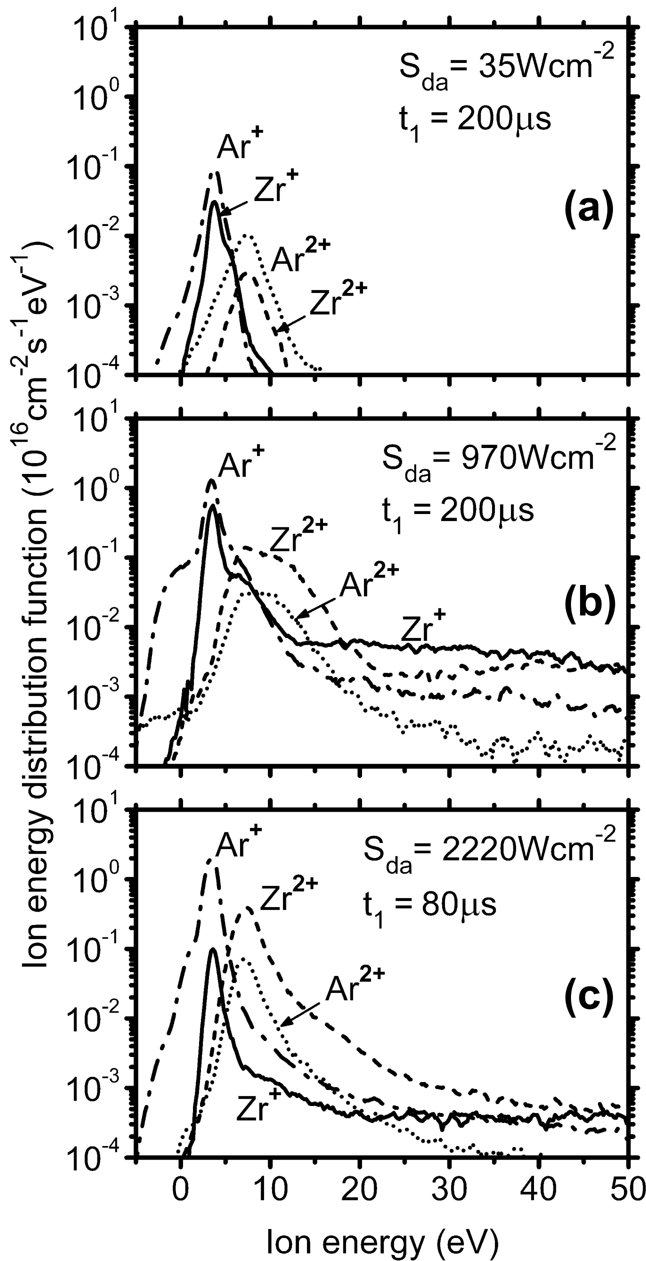

Fig. 5.5

Time-averaged energy distributions (IEDFs) of zirconium and argon ions at substrate position (target-to-orifice distance d = 100 mm) for the regimes with average target power densities **(a)** $\overline{S}_d$ = 5 Wcm^{-2}, **(b)** and **(c)** $\overline{S}_d$ = 100 Wcm^{-2}. The positions of peaks in the energy distributions are attributed to the values of respective plasma potential in the spectrometer's vicinity. The populations of ions with high energies (up to 100 eV) are significant for the regimes shown in panels **(b)** and **(c)**. Presented IEDFs are averaged from 5 measurements. High-energy tails are computationally smoothed.

Experimental conditions: pulsed DC discharge, repetition frequency f_r = 500 Hz, argon process-gas pressure p = 1 Pa. See Table 5.1 (p. 80).

The integral values of individual ion fluxes and compositions of the total ion fluxes at substrate distances d = 70 mm, 100 mm and 200 mm are given in Fig. 5.6 (p. 76), Fig. 5.7 (p. 79), Table 5.1 (p. 80), Table 5.2 (p. 81) and Table 5.3 (p. 83). As shown in Fig. 5.6 (p. 76), an increase in the values of $\overline{S}_d$ from 5 Wcm^{-2} to values close to 100 Wcm^{-2} at the same voltage pulse duration t_1 = 200 μs results in a rapid rise in the individual ion fluxes onto the substrate. A total fraction of the Zr^+ and Zr^{2+} ions in the ion flux (see Table 5.1 [p. 80]) increases from m_s = 23.7% for $\overline{S}_d$ = 5 Wcm^{-2} to m_s = 44.0% for $\overline{S}_d$ = 103 Wcm^{-2} at d = 100 mm, and from m_s = 28.1% for $\overline{S}_d$ = 5 Wcm^{-2} to m_s = 48.3% for $\overline{S}_d$ = 100 Wcm^{-2} at d = 200 mm. A rising average target power density S_{da} from 970 Wcm^{-2} (for d = 100 mm) or from 950 Wcm^{-2} (for d = 200 mm) to 2220 Wcm^{-2} in shortened pulses (from 200 μs to 80 μs) at a constant

average target power density in a period $\overline{S}_d$ = 100 ± 3 Wcm^{-2} leads to significant changes in the compositions of the total ion fluxes at all the substrate positions. For d = 70 mm and 100 mm, the Zr^{2+} ions become dominant metallic ions (30.9% — 34.1% and 21.3% — 31.5%, respectively) in the flux, while the flux of the Zr^{+} ions rapidly decreases (see Fig. 5.6 [p. 76]). The doubly charged Zr^{2+} ions become even strongly dominant (up to 62.5%) ionic species in the total ion flux onto the substrate at the distance d = 200 mm.

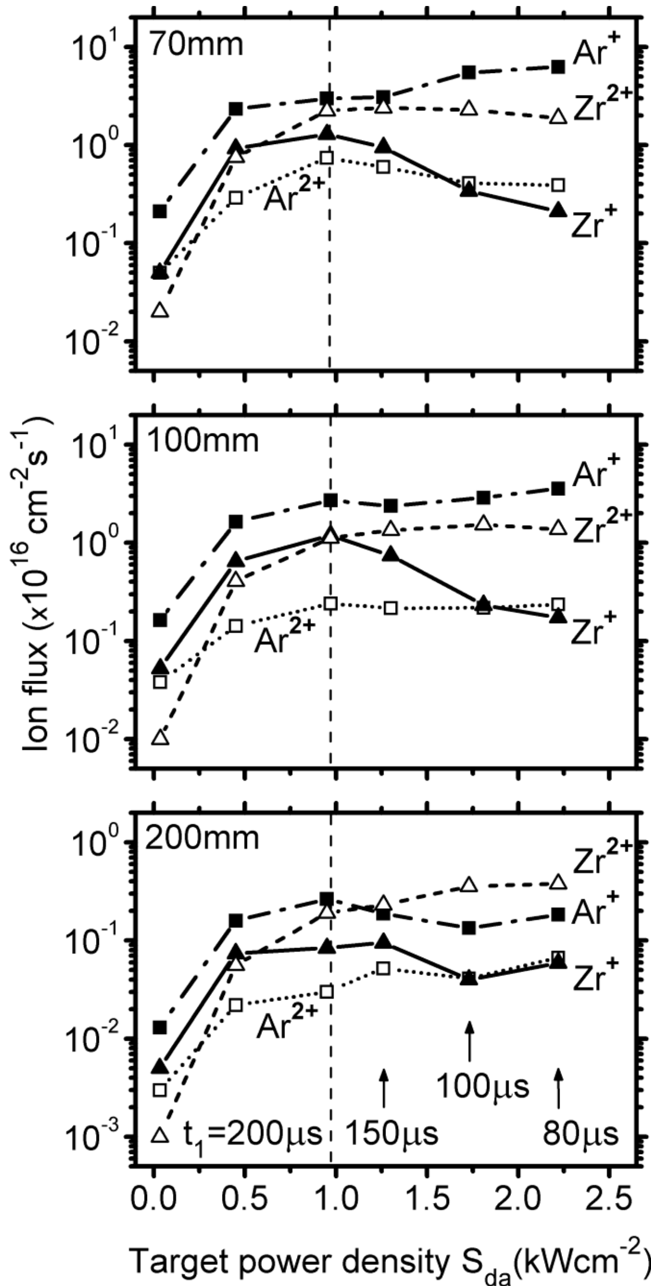

Fig. 5.6
Integral ion fluxes of the zirconium and argon ions at three substrate positions (d = 70 mm, 100 mm and 200 mm) as functions of the average pulse target power density, S_{da}. The preset average target power densities in a period, $\overline{S}_d$, ranged from 5 Wcm^{-2} to 103 Wcm^{-2} at a constant voltage pulse duration t_1 = 200 µs for $S_{da} \leq 970$ Wcm^{-2} (marked by the dashed vertical line), while the values of $\overline{S}_d$ were almost constant (100 ± 3 Wcm^{-2}) at decreasing values of t_1 from 200 µs to 80 µs for $S_{da} \geq 970$ Wcm^{-2} (see Table 5.1 [p. 80]).

Experimental conditions: pulsed DC discharge, repetition frequency f_r = 500 Hz, argon process-gas pressure p = 1 Pa.

Note that a high occurrence of the doubly charged metallic ions in the flux onto the substrate could be utilized in ion-assisted growth of films and in substrate-coating interface engineering as the same effects on microstructure of the films, and on composition, structure and thickness of an interfacial region between a pre-treated substrate and the coatings might be achieved at an approximately half negative substrate bias voltage needed for singly charged ions [9].

As seen in Fig. 5.6 (p. 76), the Ar^+ ions remain dominant in the total ion flux onto the substrate for d = 70 mm and 100 mm even at high values of target power loading. Given the significantly lower first ionization energy of Zr (6.63 eV) compared with both the ionization limits of Ar (15.76 eV and 15.94 eV), this can be mainly explained by relatively low sputtering yields of Zr (cf. the case of titanium [111]). For example, for the kinetic energy of singly charged ions of 600 eV the corresponding values of the sputtering yields are 0.92 for sputtering by Ar^+ ions and 0.65 for self-sputtering [118].

The noticeably increased S_{da} in the shortened pulses with $t_1 < 200$ µs results in significantly higher values of the electron number density, n_e, and the electron temperature, T_e, in a discharge plasma during the pulses (recall the relation $\Gamma_{ita} \propto n_e T_e^{0.5}$ valid for the corresponding average values in a pulse at the plasma-sheath interface [101]). This leads to substantially higher rates of the electron impact excitation and ionization (both direct and stepwise processes via highly populated excited states) of sputtered zirconium atoms and their ions. Let us note the very low second ionization energy of Zr (13.16 eV), being close to that of Ti (13.58 eV) but much lower compared with the values for many metals of practical interest, such as Ag (21.45 eV), Cu (20.29 eV), Al (18.83 eV), Cr (16.49 eV), Ta (15.55 eV) and Nb (14.30 eV) [124,125].

The much stronger ionization of Zr atoms compared with Ar atoms in the discharge plasma at distances z > 100 mm from the target is of key importance for prevalence (m_s up to 69.5%) of the zirconium ions in the total ion fluxes onto the substrate for d = 200 mm and $t_1 < 200$ µs (see Table 5.1 [p. 80]). The decreased values of m_s = 36.3% and 28.8% obtained at the distance d = 100 mm for the shortest voltage pulses with t_1 = 100 µs and 80 µs, respectively, (see Table 5.1 [p. 80] and Fig. 5.10 [p. 84]) are a consequence of the reduced sputtering rates (see Sec. 5.1.3 [p. 84]) and a stronger influence of the initial phases of the pulses with a prevailing ionization of argon atoms [30,122].

Taking into account the high occurrence of the Ar^+ ions in the discharge plasma (Fig. 5.6 [p. 76]) and the very low values of the first and second ionization energy of Zr, the following two collision processes should be considered, together with the dominant electron impact processes, in the production of the Zr^{2+} ions. These are the usual charge transfer reaction [102, 126-130]

$$Ar^+(1) + Zr(1) \rightarrow Ar(1) + Zr^+(p) + \Delta E \qquad (5.3)$$

and a possible charge transfer reaction

$$Ar^+(1) + Zr^+(1) \rightarrow Ar(1) + Zr^{2+}(q) + \Delta E \quad . \qquad (5.4)$$

Here, the level number 1 denotes the ground states of the corresponding atoms and singly charged ions, while p and q denote the excited states of the Zr^{+} ions and the Zr^{2+} ions, respectively. In Eq. 5.3, ΔE is the difference between the total excitation energy of the $Zr^{+}(p)$ state [with respect to the Zr(1) ground state] and the ionization energy of the Ar(1) ground state. In Eq. 5.4, ΔE is the difference between the excitation energy of the $Zr^{2+}(q)$ state [with respect to the $Zr^{+}(1)$ ground state] and the ionization energy of the Ar(1) ground state. For both reactions the condition $\Delta E \geq 0$ is required. Usually, the largest cross-sections for the charge transfer were found when ΔE was in the range 0.1 eV – 1.0 eV [129].

We assume that the charge transfer between the $Ar^{+}(1)$ ions and the Zr(1) atoms leads to the production of the highly excited $Zr^{+}(p)$ ions [being less than 4 eV from the $Zr^{2+}(1)$ ground state], which are easily ionized by the electron impact in the dense discharge plasma to form the doubly charged Zr^{2+} ions. In contrast with the decreasing efficiency of the electron impact processes in pulse-off times due to rapidly decreasing electron temperatures [59], particularly at larger distances from the target, the reactions presented in Eq. 5.3 (p. 77) and Eq. 5.4 (p. 77) remain effective in an afterglow plasma for much longer times [127].

In Fig. 5.7 (p. 79) and Table 5.2 (p. 81), the results of the experiment as t_1 was lowered from 200 μs down to 20 μs at fixed $\overline{S}_d$ = 45 ± 5 Wcm^{-2} and, correspondingly, S_{da} increased from 470 ± 15 Wcm^{-2} up to 3150 ± 250 Wcm^{-2} are presented. Clearly, there were analogous trends in the composition of total ion flux onto the substrate as compared to the experiment with shortening the t_1 from 200 μs to 80 μs at fixed $\overline{S}_d$ = 100 ± 3 Wcm^{-2}. The decrease in the fraction of Zr^{+} was observed with shortening the t_1 from 200 μs. Ar^{+} ions dominated in the flux at all the distances and the fluctuations in the fractions or Ar^{+} ions were almost identical to those detected in the previous experiment for corresponding target-to-probe distances and S_{da}. At the distance of 70 mm, the fraction of Ar^{+} ions steadily increased for S_{da} exceeding 1000 Wcm^{-2}, at the distances of 100 mm and 200 mm the rise in Ar^{+} fraction occurred for S_{da} higher than 1500 Wcm^{-2}. For S_{da} over 1000 Wcm^{-2}, Zr^{2+} ions dominated over Zr^{+} ions at all the distances and the total fraction of Zr ions started to drop significantly for pulse-on times shorter than 60 μs since (i) a significant amount of Ar process-gas is present in the plasma region for such a short pulses regardless of the rise in S_{da} up to 3405 Wcm^{-2} and (ii) the electron temperature attains significantly higher values for short pulse-on times promoting the electron-impact ionization processes of the species with high ionization potential [59,60]. Consequently, the Ar^{2+} ions prevailed over the Zr^{+} ions for t_1 shorter than 60 μs.

Taking into account the results of both experiments employing the shortening of t_1 at constant $\overline{S}_d$, it was found that the fraction of Zr^{2+} in the total ion flux on the substrate was maximized when t_1 was set long enough for the discharge to evolve from a process-gas dominated phase. Further prolonging of t_1 at fixed $\overline{S}_d$ resulted in a decrease of fraction of Zr^{2+} ions.

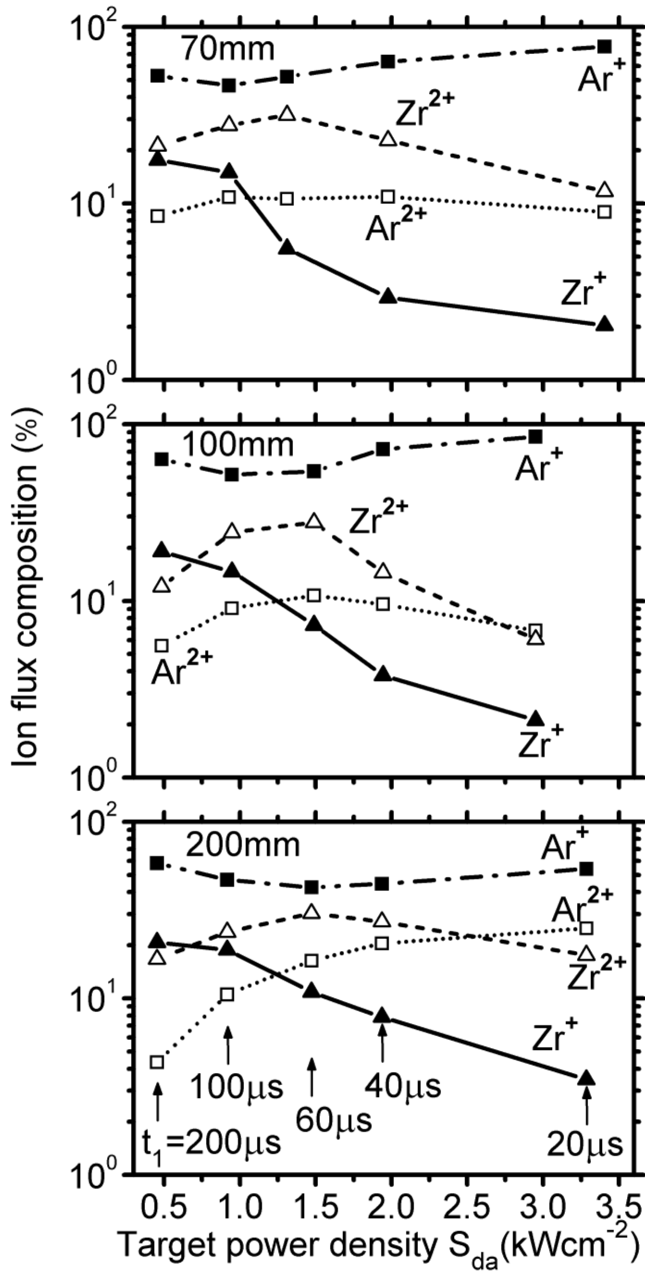

Fig. 5.7
Integral ion fluxes of the zirconium and argon ions at three substrate positions (d = 70 mm, 100 mm and 200 mm) as functions of the average pulse target power density, S_{da}. The preset average target power density in a period, $\overline{S}_d$, was fixed at 50 Wcm^{-2} and the pulse duration, t_1, was shortened from 200 μs down to 20 μs. The corresponding values of S_{da} increased from 470 ± 20 Wcm^{-2} to 3200 ± 200 Wcm^{-2} (see Table 5.2 [p. 81]).
Experimental conditions: pulsed DC discharge, repetition frequency f_r = 500 Hz, argon process-gas pressure p = 1 Pa.

Table 5.1

Discharge characteristics and compositions of total ion fluxes at three substrate positions (d = 70 mm, 100 mm and 200 mm). The preset average target power densities in a period, $\overline{S}_d$, ranged from 5 Wcm^{-2} to 103 Wcm^{-2} at a constant voltage pulse duration t_1 = 200 µs for $S_{da} \leq 970$ Wcm^{-2}, while the values of $\overline{S}_d$ were almost constant (100 ± 3 Wcm^{-2}) at decreasing values of t_1 from 200 µs to 80 µs for $S_{da} \geq 970$ Wcm^{-2}. Here, S_{da} is the average pulse target power density, U_{da} is the average pulse voltage and $\overline{Q}_{Is}$ is the mean ion charge state number in the flux to the substrate. Pulse repetition frequency was 500 Hz and argon process-gas pressure was 1 Pa.

Process parameters			Discharge characteristics				Composition of total ion flux (%)			
t_1 (µs)	$\overline{S}_d$ (Wcm^{-2})	d (mm)	S_{da} (Wcm^{-2})	U_{da} (V)	$\overline{J}_s$ (mAcm^{-2})	$\overline{Q}_{Is}$	Zr^+	Zr^{2+}	Ar^+	Ar^{2+}
200	4	70	36	380	0.7	1.19	15.2	5.0	65.7	14.1
200	43	70	430	575	9.4	1.24	21.4	17.5	54.4	6.7
200	97	70	957	672	17.9	1.41	17.8	30.9	41.2	10.2
150	93	70	1301	727	17.5	1.43	13.5	34.1	43.8	8.6
100	94	70	1829	794	19.7	1.32	4.0	26.8	64.4	4.8
80	92	70	2189	856	19.4	1.26	2.4	21.5	71.6	4.5
200	5	100	35	359	0.4	1.18	19.9	3.8	61.9	14.4
200	49	100	450	596	6.1	1.19	22.9	14.4	57.7	5.0
200	103	100	970	683	12.0	1.26	22.7	21.3	51.4	4.6
150	99	100	1300	707	11.1	1.33	15.9	28.8	50.7	4.6
100	100	100	1810	794	11.9	1.36	4.8	31.5	59.2	4.5
80	103	100	2220	881	10.0	1.30	3.2	25.6	66.8	4.4
200	5	200	33	386	0.05	1.17	23.5	4.6	59.3	12.6
200	50	200	450	596	0.7	1.25	23.9	18.1	51.0	7.0
200	100	200	950	672	1.4	1.39	14.8	33.5	46.4	5.3
150	103	200	1270	684	1.5	1.50	16.7	41.1	33.0	9.2
100	101	200	1740	755	1.7	1.70	7.0	62.5	23.3	7.2
80	99	200	2220	856	2.0	1.65	8.5	55.6	26.3	9.6

Table 5.2
Discharge characteristics and compositions of total ion fluxes at three substrate positions (d = 70 mm, 100 mm and 200 mm) for a preset average target power density in a period $\overline{S}_d$ = 45 ± 5 Wcm^{-2}, a voltage pulse duration, t_1, from 20 μs to 200 μs and a corresponding average pulse target power density, S_{da}, ranging from 470 ± 20 Wcm^{-2} to 3200 ± 200 Wcm^{-2}. Here, U_{da} is the average pulse voltage and $\overline{Q}_{Is}$ is the mean ion charge state number in the flux to the substrate. Pulse repetition frequency was 500 Hz and argon process-gas pressure was 1 Pa.

Process parameters			Discharge characteristics			Composition of total ion flux (%)			
t_1 (μs)	$\overline{S}_d$ (Wcm^{-2})	d (mm)	S_{da} (Wcm^{-2})	U_{da} (V)	$\overline{Q}_{Is}$	Zr^+	Zr^{2+}	Ar^+	Ar^{2+}
200	46	70	458	584	1.30	17.6	21.2	52.7	8.5
180	47	70	515	591	1.34	15.8	24.3	50.1	9.9
160	44	70	540	591	1.36	16.2	26.1	48.2	9.5
140	47	70	662	598	1.36	16.5	26.3	47.6	9.6
120	45	70	750	602	1.37	15.4	27.4	47.8	9.4
100	48	70	929	630	1.39	15.0	27.7	46.5	10.9
80	48	70	1150	682	1.35	10.4	25.2	54.9	9.6
60	42	70	1311	715	1.42	5.6	31.7	52.1	10.6
40	44	70	1977	840	1.34	2.9	22.8	63.4	10.9
20	44	70	3405	1124	1.21	2.0	11.7	77.3	9.0
200	49	100	484	610	1.18	19.0	12.1	63.3	5.6
180	45	100	491	592	1.22	19.1	16.0	58.9	5.9
160	48	100	589	605	1.28	15.8	18.2	56.1	10.0
140	45	100	629	605	1.28	15.0	18.4	56.9	9.7
120	45	100	734	611	1.30	13.9	21.1	56.0	9.0
100	50	100	948	656	1.34	14.6	24.4	51.9	9.1
80	47	100	1132	699	1.42	13.1	30.8	45.1	11.0
60	48	100	1489	761	1.39	7.3	27.8	54.1	10.8
40	44	100	1944	877	1.24	3.8	14.4	72.2	9.6
20	37	100	2950	1112	1.13	2.1	6.1	85.0	6.8
200	46	200	453	631	1.21	20.8	16.7	58.2	4.3
180	48	200	523	642	1.22	20.1	17.5	57.6	4.8
160	47	200	584	646	1.23	19.5	18.1	57.0	5.4
140	48	200	678	654	1.25	19.8	19.6	54.8	5.8
120	48	200	785	662	1.27	18.6	20.3	54.3	6.8
100	47	200	917	688	1.34	18.8	23.8	46.9	10.5
80	47	200	1117	746	1.40	15.8	26.0	44.6	13.6
60	47	200	1473	814	1.47	10.9	30.3	42.5	16.3
40	44	200	1937	947	1.48	7.9	27.2	44.5	20.5
20	41	200	3285	1296	1.42	3.5	17.6	54.0	24.9

In Fig. 5.8 (p. 82), Fig. 5.9 (p. 83) and in Table 5.3 (p. 83), the effect of shortening t_l at a fixed U_{da} (910 ± 15 V) is presented giving us a deeper understanding of the evolution of IEDFs and ion flux composition within the pulse-on time. All values were measured at the distance of 70 mm from the target. As shown in Fig. 5.8 (p. 82), longer t_l caused the IEDFs of all the measured ionic species to be extended to higher energies and, at the same time, the IEDFs started to exhibit a two-peak shape, which is clearly seen for the longest t_l = 100 μs, see Fig. 5.8(a) (p. 82). The IEDFs presented in Fig. 5.5(b) and (c) (p. 75) – regimes with t_l = 200 μs and 80 μs at fixed $\overline{S_d}$ = 100 ± 3 Wcm^{-2} exhibit the same behavior, i.e. shortening t_l caused the IEDFs to be narrower. Combining these findings, it can be stated that above certain level of S_{da} the shape of the IEDFs is given by the pulse-on time rather than by the value of S_{da}.

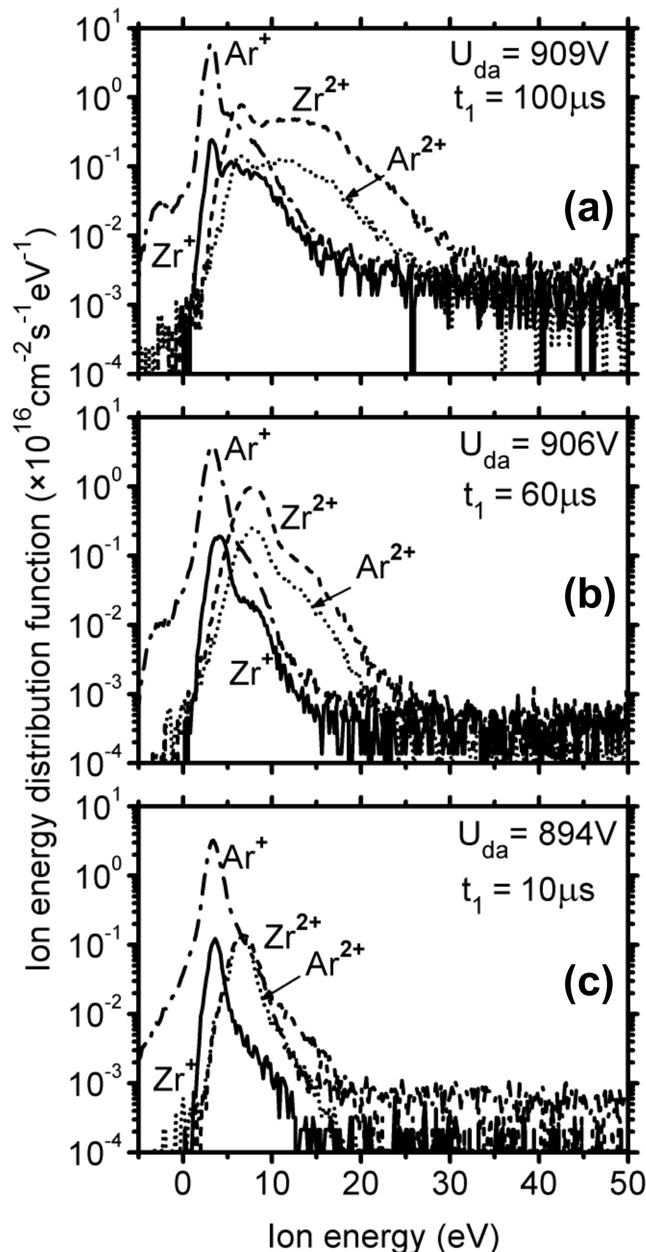

Fig. 5.8
Time-averaged energy distributions (IEDFs) of zirconium and argon ions at the substrate position for the regimes with average pulse discharge voltage U_{da} = 910 ± 15 V and different pulse durations **(a)** t_l = 100 μs ($\overline{S_d}$ = 103 Wcm^{-2}, S_{da} = 2011 Wcm^{-2}), **(b)** t_l = 60 μs, **(c)** t_l = 10 μs, see Table 5.3 (p. 83). Longer t_l times caused the IEDFs of all the ions to be extended to higher energies and, at the same time, the IEDFs started to exhibit a two-peak shape. The same effect was observed in the experiments presented in Fig. 5.5(b) and (c) (p. 75). Presented IEDFs are averaged from 5 measurements.

Experimental conditions: pulsed DC discharge, repetition frequency f_r = 500 Hz, argon process-gas pressure p = 1 Pa, target-to-orifice distance d = 70 mm.

In Fig. 5.9 (p. 83), the changes in the composition of total ion flux as a consequence of shortening t_1 are given. Prolonging t_1 resulted in rising fractions of Zr ions in the plasma due to a higher amount of the sputtered species in the discharge and as a result of process-gas rarefaction. For t_1 higher than 60 µs the trend in rising the fraction of Zr ions slackened indicating the timescale of termination of a process-gas dominated phase of the discharge.

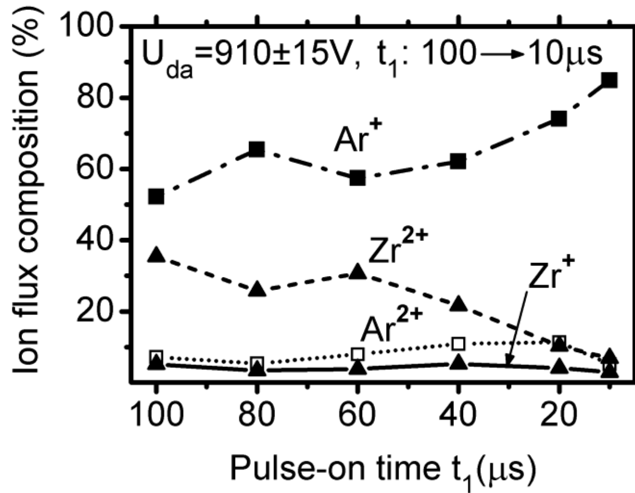

Fig. 5.9
Composition of total ion fluxes of the zirconium and argon ions. The average pulse discharge voltage was fixed at U_{da} = 910 ± 15 V and the pulse duration time, t_1, was shortened from 100 µs (the corresponding target power densities were $\overline{S}_d$ = 103 Wcm^{-2}, S_{da} = 2011 Wcm^{-2}) down to 10 µs, see Table 5.3 (p. 83).
Experimental conditions: pulsed DC discharge, repetition frequency f_r = 500 Hz, argon process-gas pressure p = 1 Pa, target-to-orifice distance d = 70 mm.

Table 5.3
Discharge characteristics and compositions of total ion fluxes in the distance d = 70 mm from the target for a preset average pulse voltage U_{da} = 910 ± 15 V and a voltage pulse duration, t_1, ranging from 100 µs to 10 µs. Here, $\overline{S}_d$ is the target power density in a period, S_{da} is the average pulse target power density and $\overline{Q}_{Is}$ is the mean ion charge state number in the flux to the substrate. Pulse repetition frequency was 500 Hz and argon process-gas pressure was 1 Pa.

Process parameters		Discharge characteristics				Composition of total ion flux (%)			
t_1 (µs)	U_{da} (V)	$\overline{S}_d$ (Wcm^{-2})	S_{da} (Wcm^{-2})	$\overline{J}_s$ (mAcm^{-2})	$\overline{Q}_{Is}$	Zr^+	Zr^{2+}	Ar^+	Ar^{2+}
100	909	103	2011	49	1.43	5.2	35.4	52.2	7.2
80	922	81	1977	45	1.31	3.4	25.8	65.4	5.4
60	906	51	1649	32	1.39	3.9	30.7	57.4	8.0
40	925	34	1583	27	1.33	5.3	21.7	62.1	10.9
20	911	14	1094	21	1.22	4.1	10.4	74.1	11.4
10	894	5	893	14	1.12	3.0	6.9	84.9	5.2

5.1.3 Deposition characteristics

Fig. 5.10 (p. 84) shows the fundamental deposition characteristics, namely the deposition rate of films, a_D, the deposition rate per average target power density in a period, $a_D/\overline{S}_d$, the fraction of target-material ions in the total ion flux onto the substrate, m_s, and the ionized fraction of target-material atoms in the flux onto the substrate, θ, as functions of the increasing average target power density in a pulse, S_{da}, for the substrate distance d = 100 mm. Here, it should be mentioned that the $a_D/\overline{S}_d$ ratio is an important parameter characterizing the efficiency of the magnetron sputtering and the transfer of the sputtered particles to the substrate. Therefore, a decrease in the $a_D/\overline{S}_d$ ratios caused only by the increasing values of the average pulse voltage, U_{da}, in the same way as in the conventional DC magnetron sputtering, is presented in Fig. 5.10 (p. 84) for comparison. The expression used, $a_D/\overline{S}_d = kU_{da}^{-0.5}$, where k is a constant, was obtained under the assumption that the Zr target is bombarded only by singly charged ions and that the scaling $\gamma_{sp} \propto (eU_{da})^{0.5}$ holds for the corresponding sputtering yield γ_{sp} [36,46,101,103].

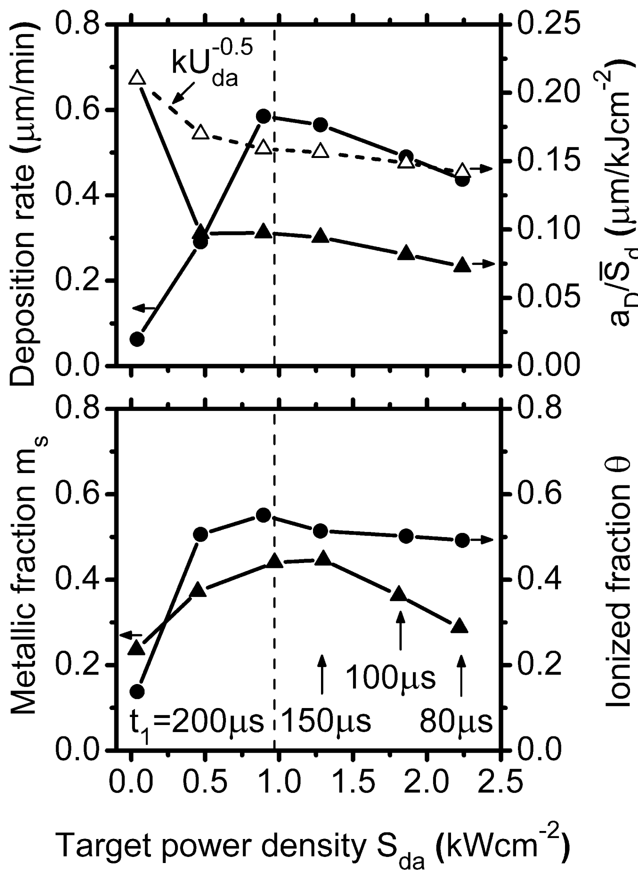

Fig. 5.10

Deposition rate, a_D, deposition rate per average target power density in a period, $a_D/\overline{S}_d$, fraction of the target material ions in the total ion flux onto the substrate, m_s, and the ionized fraction of the target material atoms in the flux onto the substrate, θ, as functions of the average pulse target power density S_{da}. Slight differences in the corresponding values of S_{da} were mainly caused by small changes in the target erosion depth since the deposition rates and the ion flux characteristics were measured independently. For comparison, the empty symbols represent the values predicted by the relation $a_D/\overline{S}_d = kU_{da}^{-0.5}$, where k is a constant.

Experimental conditions: pulsed DC discharge, repetition frequency f_r = 500 Hz, argon process-gas pressure p = 1 Pa, target-to-substrate distance d = 100 mm. See Table 5.1 (p. 80).

As seen in Fig. 5.10 (p. 84), an increase in the values of $\overline{S}_d$ from 5 Wcm^{-2} to 99 Wcm^{-2} at the same voltage pulse duration t_1 = 200 μs leads to a rapid rise in the deposition rate (up to a_D = 590 nm/min) and in the ionized fraction of Zr atoms in the flux onto the substrate (up to θ = 55% at the corresponding value of m_s = 44%, see also Table 5.1 [p. 80]). The $a_D/\overline{S}_d$ ratio decreased 2.2 times. This is mainly due to an enhanced redirection of the ionized sputtered atoms back to the target and their higher losses, compared with the sputtered neutrals, to chamber walls during their transfer to the substrate at the high values of S_{da} = 470 Wcm^{-2} and 900 Wcm^{-2} relating to $\overline{S}_d$ = 49 Wcm^{-2} and 99 Wcm^{-2}, respectively [103]. A rising average target power density S_{da} from 900 Wcm^{-2} to 2240 Wcm^{-2} in shortened pulses (from 200 μs to 80 μs) at a constant average target power density in a period $\overline{S}_d$ = 99 – 100 Wcm^{-2} resulted in a decrease in the deposition rate from 590 nm/min to 440 nm/min. This relatively small reduction (1.34 times) is in qualitative agreement with the relation $a_D/\overline{S}_d \propto \left(\overline{Q}_{It} U_{da}\right)^{-0.5}$ where $\overline{Q}_{It}$ is the mean ion charge state number in the flux to the target [44]. It is assumed (see non-increasing values of m_s in Fig. 5.10 [p. 84]) that the backward flux of the ionized Zr atoms to the target and their losses to chamber walls are not getting systematically higher with increasing values of S_{da} in the shortened pulses considered. Weakly decreasing values of θ from 55% to 49% were observed under these conditions. The shortening of the voltage pulses might result in a higher fraction of the sputtered Zr atoms (being sputtered in final phases of the voltage pulses before their rapid switch-off) which are not ionized during their flight through the afterglow plasma towards the substrate.

5.1.4 Efficiency of the magnetron sputtering and the transfer of sputtered particles to the substrate

The average total flux of the particles to be deposited onto the substrate per average target power density in a period, $\overline{\Gamma}_D/\overline{S}_d$, characterizes the efficiency of the magnetron sputtering and the transfer of the sputtered particles to the substrate. It can be written in the form

$$\frac{\overline{\Gamma}_D}{\overline{S}_d} = \frac{\overline{\Gamma}_{It}}{\overline{S}_d}\frac{\overline{\Gamma}_{sp}}{\overline{\Gamma}_{It}}\frac{\overline{\Gamma}_D}{\overline{\Gamma}_{sp}} \quad , \qquad (5.5)$$

where the ratios $\overline{\Gamma}_{It}/\overline{S}_d$, $\overline{\Gamma}_{sp}/\overline{\Gamma}_{It}$ and $\overline{\Gamma}_D/\overline{\Gamma}_{sp}$ characterize the three stages of the complicated deposition processes, namely (i) the ionization of the process-gas and target-material atoms in front of the target and the redirection of the arising ions back to the target, (ii) the sputtering of the target and (iii) the transport of sputtered particles to the substrate, respectively. The considered pathways of particles are delineated in Fig. 5.11 (p. 86) together with the quantities β and σ which denote the probabilities of the sputtered target-material atom to be ionized and redirected back to the target, respectively. It should be emphasized that the values of (i) $\overline{\Gamma}_{It}$ are derived from the measured values of $\overline{J}_t$, and assumed values of $\overline{F}_{It}^{n}$, (ii) $\overline{\Gamma}_{sp}$

are calculated based on the assumed values of $\overline{F}_{It}^{n}$ and on the computed values of γ_{sp}, (iii) $\overline{\Gamma}_{D}$ are derived from the respective deposition rates, a_{D}.

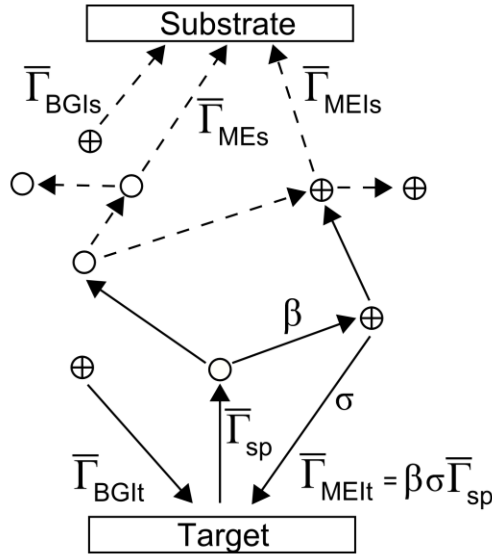

Fig. 5.11
Pathways of particles during the non-reactive sputtering process. Particle fluxes are denoted by the 'Γ' letter. The processes considered are: (i) target (t) sputtering by process-gas (BG, e.g. argon) ions (I) and target-material (ME, e.g. zirconium) ions, (ii) ionization of sputtered (sp) target material with probability β, (iii) backward flux of the ionized target material atoms to the target with probability σ, (iv) transport of BG ions (BGI) to the substrate (s) (v) deposition of sputtered target-material species on the substrate and (vi) their respective losses to the chamber walls.

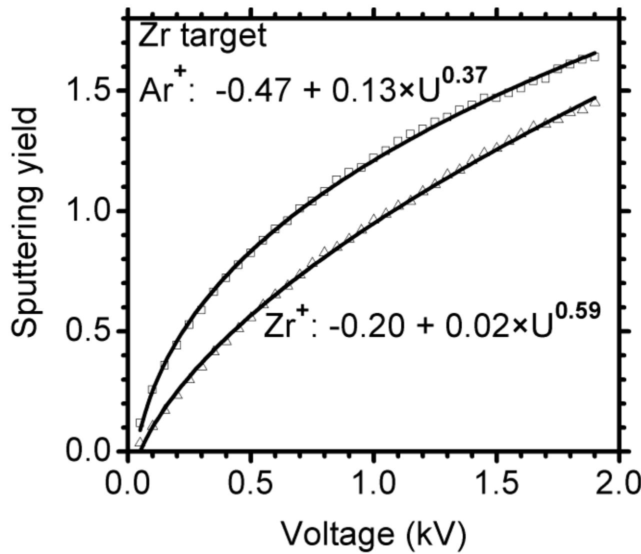

Fig. 5.12
Sputtering yield of the target material (Zr), γ_{sp}, as a function of the energy of the impinging particles for the particular case of sputtering by Ar+ and Zr+ ions. The sputtering yields are evaluated by the TRIM code (empty symbols) and formulae of the corresponding numerical fits (full lines) are given [118].

To evaluate these ratios under the conditions described in Table 5.1 (p. 80) for the substrate distance d = 100 mm, we used the corresponding measured values of $\overline{S}_{d}$, $\overline{J}_{t}$, U_{da} and $\overline{\Gamma}_{D}$. The flux of ions onto the target is assumed to be formed by target-material ions and process-gas ions, i.e., analogously to Eq. 4.26 (p. 53) and Eq. 4.27 (p. 54): $\overline{\Gamma}_{It} = \overline{\Gamma}_{It}(Zr) + \overline{\Gamma}_{It}(Ar)$, where $\overline{\Gamma}_{It}(Zr) = \overline{\Gamma}_{It}(Zr^{+}) + \overline{\Gamma}_{It}(Zr^{2+})$ and $\overline{\Gamma}_{It}(Ar) = \overline{\Gamma}_{It}(Ar^{+}) + \overline{\Gamma}_{It}(Ar^{2+})$. Note that the condition $\overline{\Gamma}_{It}(Zr) \leq \overline{\Gamma}_{sp}$,which is identical to the condition $\beta\sigma \leq 1$ imposes the limits on the composition of the ion flux onto the target, see the shadow area in Fig. 5.13 (p. 87). Since we do not know the values of the average fractions of particular ions in the total

ion flux onto the target, $\overline{F}_{It}^{n}$, in Eq. 4.23 (p. 52), Eq. 4.25 (p. 53) and Eq. 4.29 (p. 54) for $\overline{\Gamma}_{It}$ and $\overline{\Gamma}_{sp}$, respectively, our model calculations were carried out for the following hypothetical compositions of the total ion flux onto the target: 100% Ar^{+}, 100% Zr^{+}, 100% Zr^{2+} and the corresponding compositions of the total ion fluxes onto the substrate given in Table 5.1 (p. 80). Although a sustained self-sputtering process cannot be achieved with a Zr target bombarded by Zr^{+} ions at U_d < 1070 V and by Zr^{2+} ions at U_d < 535 V (because of γ_{sp}< 1 as shown in Fig. 5.12 [p. 86] and illustrated by shaded area in Fig. 5.13 [p. 87]), and a total predominance of the Zr^{2+} ions is unrealistic, the 100% fractions of the Zr^{+} ions or the Zr^{2+} ions in the total ion flux onto the target are considered to specify limits for the possible values of the quantities calculated (Fig. 5.14 [p. 88]). The fitting formulas given in Fig. 5.12 (p. 86) were used to evaluate the values of $\overline{\Gamma}_{sp}$ used in Fig. 5.14 (p. 88).

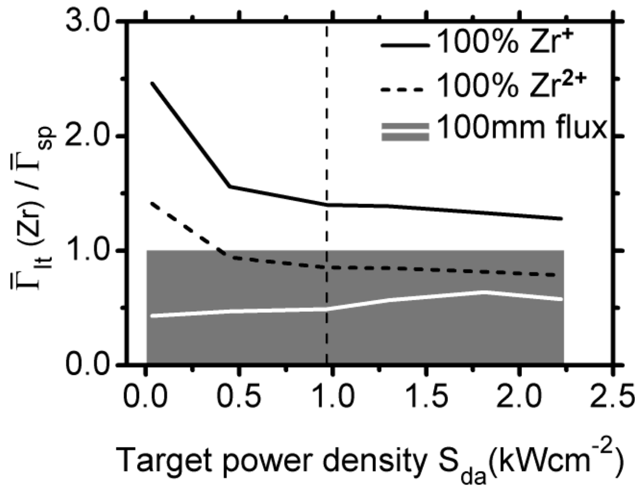

Fig. 5.13
Backward flux of sputtered and ionized Zr atoms to the target. The condition $\overline{\Gamma}_{It}(Zr) \leq \overline{\Gamma}_{sp}$ imposes the limits on the composition of the ion flux onto the target, see the shadow area. In the calculations, the same process parameters as in Table 5.1 (p. 80) were used. The calculations were carried out for the following compositions of the total ion flux onto the target: 100% Zr^{+} (full black line), 100% Zr^{2+} (dashed line) and the corresponding compositions of the total ion fluxes onto the substrate given in Table 5.1 (p. 80) (white line).
Experimental conditions: pulsed DC discharge, repetition frequency f_r = 500 Hz, argon process-gas pressure p = 1 Pa, target-to-substrate distance d = 100 mm.

To understand the dependencies obtained for the ratios $\overline{\Gamma}_{It}/\overline{S}_{d}$ and $\overline{\Gamma}_{sp}/\overline{\Gamma}_{It}$, the simplified relations $\overline{S}_{d} \cong S_{da} t_1/T$ and $\overline{\Gamma}_{It} \cong \Gamma_{Ita} t_1/T$ were used which neglect the small contributions (less than 7% except for $\overline{\Gamma}_{It}$ at t_1 = 100 µs and 80 µs with 9% and 14%, respectively) corresponding to the pulse-off times in Eq. 4.21 (p. 47) and Eq. 4.25 (p. 53). Assuming that $S_{da} \cong U_{da} J_{ta}$, $\overline{\Gamma}_{sp} \propto (\overline{Q}_{It} U_{da})^{0.5} \Gamma_{Ita} t_1/T$, and setting the secondary-electron recapture coefficient at the target surface r = 0.5, the two ratios can be written as

$$\frac{\overline{\Gamma}_{It}}{\overline{S}_d} \cong \frac{1}{e(\overline{Q}_{It} + 0.5\gamma_{se})U_{da}} \tag{5.6}$$

and

$$\frac{\overline{\Gamma}_{sp}}{\overline{\Gamma}_{It}} \propto \left(\overline{Q}_{It} U_{da}\right)^{0.5} \quad . \tag{5.7}$$

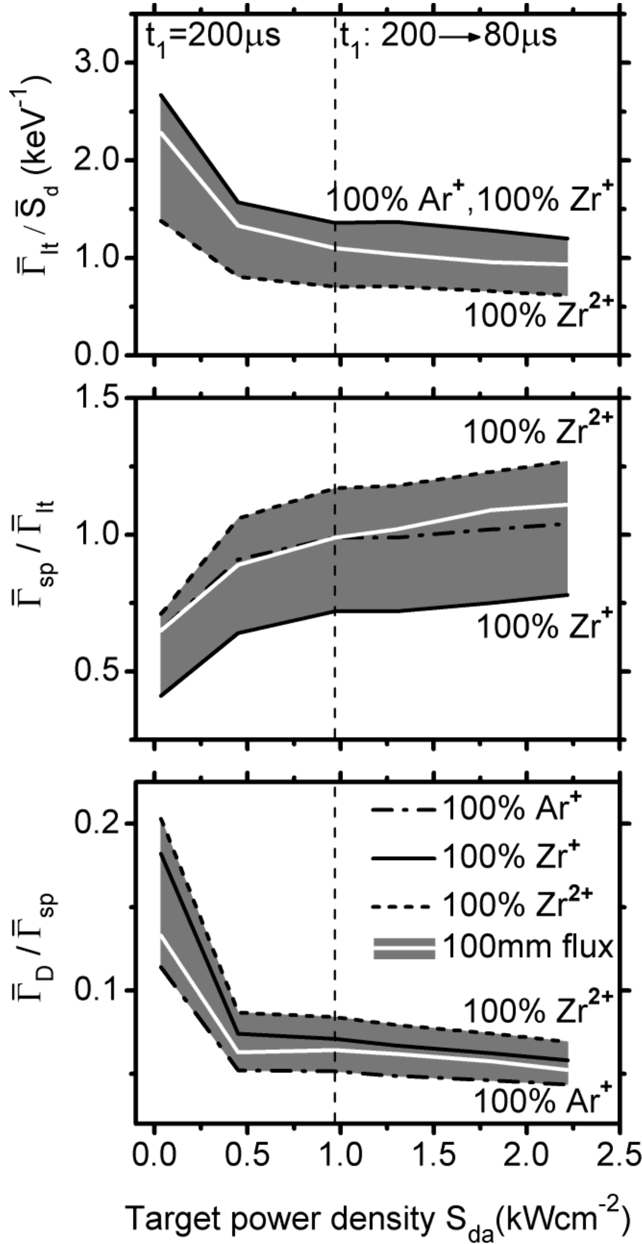

Fig. 5.14
The average total ion flux onto the target per average target power density in a period, $\overline{\Gamma}_{it}/\overline{S}_d$, the average flux of sputtered target atoms per average total ion flux onto the target, $\overline{\Gamma}_{sp}/\overline{\Gamma}_{It}$, and the average total flux of deposited particles onto the substrate per average flux of sputtered target atoms, $\overline{\Gamma}_D/\overline{\Gamma}_{sp}$, as functions of the average pulse target power density, S_{da}. The same process parameters as in Table 5.1 (p. 80) were used. The calculations were carried out for the following compositions of the total ion flux onto the target: 100 % Ar^+ (dashed-dotted line), 100% Zr^+ (full black line), 100% Zr^{2+} (dashed line) and the corresponding compositions of the total ion fluxes onto the substrate given in Table 5.1 (p. 80) (white line). Possible values of the calculated quantities can be found within the shaded areas.
Experimental conditions: pulsed DC discharge, repetition frequency f_r = 500 Hz, argon process-gas pressure p = 1 Pa, target-to-substrate distance d = 100 mm.

As seen in Fig. 5.14 (p. 88), the average total ion flux onto the target per average target power density in a period, $\overline{\Gamma}_{It}/\overline{S}_{d}$, decreases with an increasing target power density S_{da} caused by the higher values of U_{da} given in Table 5.1 (p. 80) and in probably higher values of $\overline{Q}_{It}$ (see the increase in $\overline{Q}_{Is}$). In contrast, the $\overline{\Gamma}_{sp}/\overline{\Gamma}_{It}$ ratio, that is, the average number of sputtered atoms per incident ion, increases under the same conditions.

The $\overline{\Gamma}_{D}/\overline{\Gamma}_{sp}$ ratio determines the fraction of sputtered atoms reaching the substrate as neutral or ionized particles. It provides information on losses of these particles during their transport to the substrate. As mentioned in Sec. 5.1.3 (p. 84), a strong decrease in the value of $\overline{\Gamma}_{D}/\overline{\Gamma}_{sp}$ when the average pulse target power density, S_{da}, raised from 35 Wcm^{-2} to 470 Wcm^{-2} at the same voltage pulse duration t_1 = 200 μs (see Fig. 5.14 [p. 88]) is mainly caused by an enhanced redirection of ionized sputtered atoms back to the target and by their higher losses, compared with sputtered neutrals, to the chamber walls [103]. It appears (see non-increasing values of m_s for d = 100 mm in Fig. 5.10 (p. 84) at the conversion of the singly charged into doubly charged zirconium ions in the discharge plasma) that an increase in the values of S_{da} from 970 Wcm^{-2} to 2220 Wcm^{-2} in shortened pulses does not lead to a rise in the fraction of the target-material ions in the total ion flux onto the target. As a result [103], the backward flux of the ionized zirconium atoms to the target and their losses to the chamber walls are almost the same under these conditions (Fig. 5.14 [p. 88]).

Recently, HiPIMS experiments employing titanium (Ti) and copper (Cu) targets were carried out at our department [111,123]. They utilized the same planar magnetron driven by a different pulsed DC power supply unit (MP 120, Rübig) capable of generating rectangular-shaped U_d waveforms. Pulse-on times, t_1, were set to 200 μs at a repetition frequency f_r = 1 kHz. All the experimental details are listed in Table 5.4 (p. 92). In the case of Ti target sputtering, $\overline{S}_{d}$ ranged from 5.6 Wcm^{-2} to 65.6 Wcm^{-2} and corresponding S_{da} values were 28 Wcm^{-2} and 328 Wcm^{-2}. Cu targets were sputtered under $\overline{S}_{d}$ ranging from 7.4 Wcm^{-2} to 108 Wcm^{-2} and respective values of S_{da} were within the limits of 37 Wcm^{-2} and 540 Wcm^{-2}. Here, the data published in these studies were used to analyze efficiency of the sputtering and the transfer of sputtered particles to the substrate as for the case of Zr sputtering (Fig. 5.13 [p. 87] and Fig. 5.14 [p. 88]).

In Fig. 5.15 (p. 90), the ratios of fluxes of Ti ions, $\overline{\Gamma}_{It}(Ti)$, and Cu ions, $\overline{\Gamma}_{It}(Cu)$, on the target to the respective fluxes of sputtered Ti and Cu atoms, $\overline{\Gamma}_{sp}$, are shown. Similarly to the case of Zr sputtering, the flux of ions on the target, $\overline{\Gamma}_{It}$, fully composed of Ti^{+} ions is not achievable because of low self-sputtering yield of Ti. On the other hand, the high self-sputtering yield of Cu does not impose any limitations on the composition of the respective $\overline{\Gamma}_{It}$ since the applied discharge voltages, U_{da}, were sufficiently high.

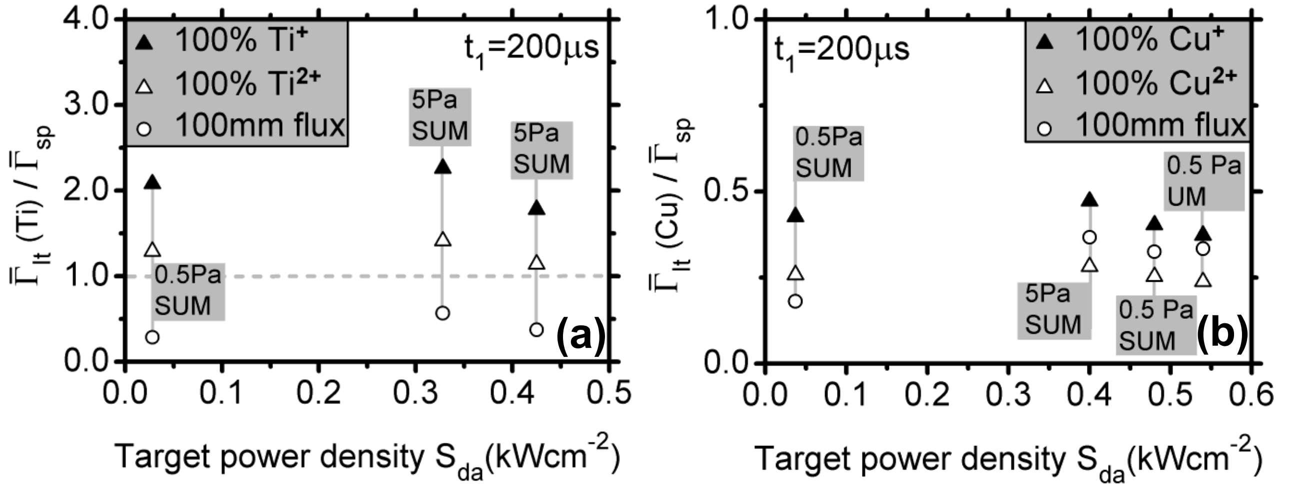

Fig. 5.15
Backward flux of sputtered and ionized metallic (ME) atoms to the target: **(a)** titanium, **(b)** copper. The condition $\overline{\Gamma}_{\mathrm{It}}(\mathrm{Me}) \leq \overline{\Gamma}_{\mathrm{sp}}$ imposes the limits on the composition of the ion flux onto the target, see the dashed line in the case **(a)** – titanium sputtering. In the calculations, the same process parameters as in Table 5.4 (p. 92) were used. The calculations were carried out for the following compositions of the total ion flux onto the target: 100% ME^{+} (full triangles), 100% ME^{2+} (open triangles) and the corresponding compositions of the total ion fluxes onto the substrate given in Table 5.4 (p. 92) (open circles). Calculations are based on data published in Refs. [111,123].

In Fig. 5.16 (p. 91), the ratios $\overline{\Gamma}_{\mathrm{It}}/\overline{S}_{\mathrm{d}}$, $\overline{\Gamma}_{\mathrm{sp}}/\overline{\Gamma}_{\mathrm{It}}$ and $\overline{\Gamma}_{\mathrm{D}}/\overline{\Gamma}_{\mathrm{sp}}$ are presented for Ti and Cu targets. The ionization efficiency attains the comparable values for both Ti and Cu targets, i.e. 2.2 keV^{-1} (Ti) and 1.6 keV^{-1} (Cu) per an ion striking the target when the $\overline{\Gamma}_{\mathrm{It}}$ is assumed to be composed of singly charged ions and the regimes with the lowest $\overline{S}_{\mathrm{d}}$ are considered. These values are in quantitative agreement with the ionization efficiency observed in the case of Zr sputtering (2.6 keV^{-1}) under the same assumptions and comparable experimental conditions: t_1 = 200 μs, S_{da} = 35 Wcm^{-2}. Rising S_{da} up to approximately 500 Wcm^{-2} caused a decrease in $\overline{\Gamma}_{\mathrm{It}}/\overline{S}_{\mathrm{d}}$ ratio of about 20% in the case of Ti and Cu discharges as opposed to 40% drop in the case of Zr. Nevertheless, at this elevated S_{da} level, all discharges exhibit the ionization efficiency close to 1.5 keV^{-1}. Note that the slight increase in the $\overline{\Gamma}_{\mathrm{It}}/\overline{S}_{\mathrm{d}}$ ratio for the case of Ti and Cu discharges at S_{da} = 328 Wcm^{-2} and 400 Wcm^{-2}, respectively, is caused by the higher pressure used, 5 Pa instead of 0.5 Pa.

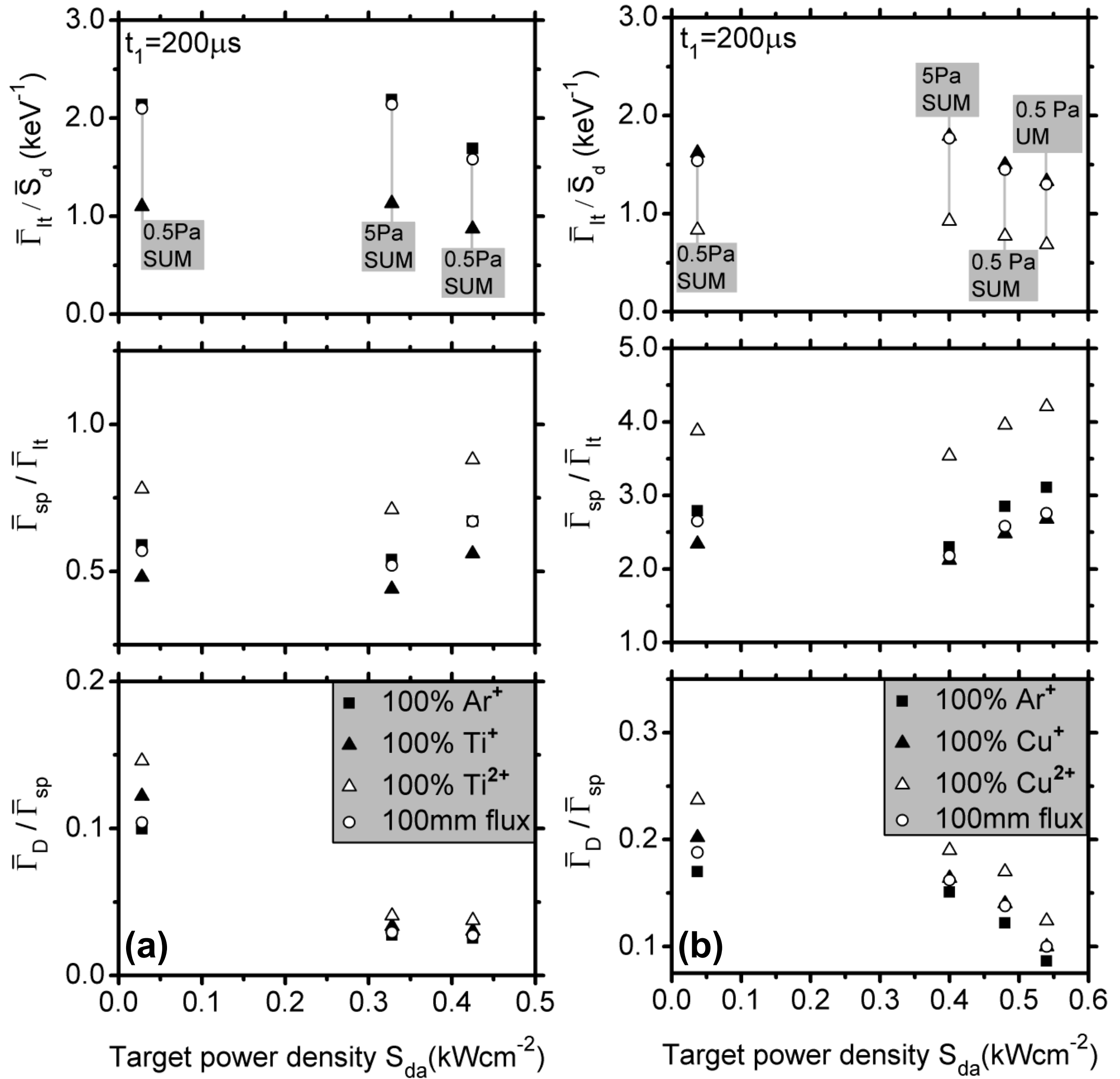

Fig. 5.16

The average total ion flux onto the target per average target power density in a period, $\overline{\Gamma}_{It}/\overline{S}_d$, the average flux of sputtered target atoms per average total ion flux onto the target, $\overline{\Gamma}_{sp}/\overline{\Gamma}_{It}$, and the average total flux of deposited particles onto the substrate per average flux of sputtered target atoms, $\overline{\Gamma}_D/\overline{\Gamma}_{sp}$, as functions of the average pulse target power density, S_{da}, for **(a)** titanium and **(b)** copper metallic (ME) targets. Process parameters are listed in Table 5.4 (p. 92). The calculations were carried out for the following compositions of the total ion flux onto the target: 100% Ar^+ (full squares), 100% ME^+ (full triangles), 100% ME^{2+} (open triangles) and the corresponding compositions of the total ion fluxes onto the substrate given in Table 5.4 (p. 92) (open circles). Calculations are based on data published in Refs. [111,123].

The sputtering efficiency given in Fig. 5.16 (p. 91) reflects the change in the process-gas and target-material sputtering yields and the variations of the discharge voltages, U_{da}. And, finally, the discernable fall in the efficiency of transport of sputtered target-material particles towards the substrate is observed for Ti and Cu targets as S_{da} was raised from approximately 30 Wcm^{-2} to 500 Wcm^{-2}. Such a drop in the $\overline{\Gamma}_D/\overline{\Gamma}_{sp}$ ratio, 75% and 50% in the case of Ti and Cu, respectively, is an indication that the loss mechanisms taking place in the HiPIMS of Ti and Cu are to be explained in the same way as the drop observed in the case of HiPIMS of Zr (decrease of 60%) as S_{da} raised from 35 Wcm^{-2} to 450 Wcm^{-2}. Note that the decrease in the $\overline{\Gamma}_D/\overline{\Gamma}_{sp}$ ratio was observed for several combinations of process-gas pressure and target-material and in two magnetron systems at approximately the same values of S_{da}, implying that the observed increase in the losses of sputtered particles are not dependent on the particular configuration of the deposition system but is more likely inherent to the HiPIMS mode of the discharge.

Table 5.4
Discharge characteristics and compositions of total ion fluxes at substrate located at a distance 100 mm from the target for titanium and copper targets. Preset average discharge current in a pulse, I_{da}, was set to 5 A and 60 A, argon process-gas pressures were 0.5 Pa and 5 Pa. In the case of copper sputtering experiments, an additional experiment employing a magnetron with a weaker magnetic field was used, see the bottommost row in the table. Here, $\overline{S}_d$ is the average target power density in a period, S_{da} is the average pulse target power density, U_{da} stands for the average pulse voltage and $\overline{Q}_{Is}$ is the mean ion charge state number in the flux to the substrate. Pulse repetition frequency was 1 kHz and pulse-on time was 200 µs. Data taken from Refs. [111,123].

Process parameters			Discharge characteristics					Composition of total ion flux (%)			
Me	I_{da} (A)	p (Pa)	$\overline{S}_d$ (Wcm^{-2})	S_{da} (Wcm^{-2})	U_{da} (V)	a_D (µm min^{-1})	$\overline{Q}_{Is}$	Me^+	Me^{2+}	Ar^+	Ar^{2+}
Ti	5	0.5	5.6	28	450	0.05	1.02	15.9	0.5	82.0	1.4
Ti	60	0.5	85.0	425	550	0.16	1.07	19.6	5.2	73.1	2.1
Ti	60	5.0	65.6	328	400	0.14	1.02	28.1	1.3	69.5	1.1
Cu	5	0.5	7.4	37	600	0.25	1.06	47.7	0.3	46.8	5.2
Cu	60	0.5	96.0	480	630	2.20	1.03	82.5	1.5	14.3	1.7
Cu	60	5.0	80.0	400	525	2.20	1.01	79.9	0.1	18.7	1.3
Cu	60	0.5	108.0	540	705	1.70	1.03	89.9	2.0	7.4	0.7

5.2 Diagnostics of reactive HiPIMS discharges

In this section, the properties of the HiPIMS reactive sputtering discharge are presented. The discharge was operated in two different modes. One mode led to the depositions of low transparent and the other one resulted in the depositions of highly transparent ZrO_x films. Discharge properties of interest were: time evolutions of the discharge current, discharge voltage and the time-averaged ion energy spectra (IESs) of particular ionic species. All these parameters were measured throughout the control cycle. In accordance with Sec. 4.3.3 (p. 51), the detailed description of the control system used for the reactive depositions is not provided in this section.

5.2.1 Control system settings

Even very slight differences in the settings of the control system (as introduced in Sec. 4.3.3 [p. 51]) parameters resulted in strong variations in deposition conditions and, consequently, in different properties of deposited films. Especially the optical characteristics were found to be sensitive to the particular deposition conditions. Thus, the optical extinction coefficient, k, served as a parameter distinguishing the films that exhibited 'low-transparency' ($k > 4\times10^{-3}$) from the ones that were of 'high-transparency'. Moreover, these two film characterizations were used to classify the corresponding modes of reactive sputtering discharges as 'more-metallic' and 'less-metallic'.

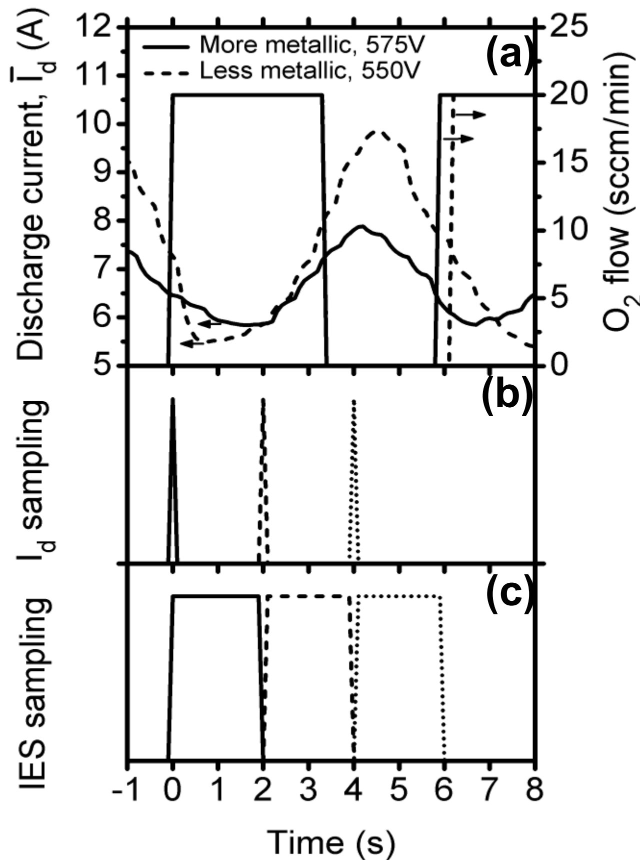

Fig. 5.17
(a) Time evolutions of the average discharge current in a period, $\bar{I}_d$, and oxygen (O_2) flow rates for a 'more-metallic' ('low-transparency' films) and a 'less-metallic' ('high-transparency' films) controlled reactive deposition processes. Average target power densities in a period, $\langle \bar{S}_d \rangle$, and average O_2 flow rates, $\langle Q \rangle$, were 49.4 Wcm^{-2}, 10.95 sccm ('more-metallic') and 51.3 Wcm^{-2}, 11.32 sccm ('less-metallic' regime) respectively.
(b) The time windows for sampling of waveforms of the discharge current, $I_d(t)$.
(c) Time windows for acquisition of ion energy spectra.
Deposition Conditions: pulsed DC discharge, repetition frequency f_r = 500 Hz, pulse duration t_1 = 200 μs, argon process-gas pressure p = 2 Pa at a flow rate of 30 sccm.

In order to identify the key quantities influencing the properties of the deposited films, two representative sets of controller settings leading to either 'more-metallic' or 'less-metallic' deposition process were used to set the deposition conditions. The values of pulse repetition frequency and pulse-on time were fixed at f_r = 500 Hz and t_1 = 200 µs. As mentioned in Sec. 4.3.3 (p. 51), the higher the flow, Q, of oxygen (O_2) into the chamber was, the more poisoned the target surface was leading to higher instantaneous values of $\bar{I}_d$ at a fixed value of U_d. Note that (i) $\bar{I}_d$, as defined Eq. 4.21 (p. 47), is the average value of the target current over the period T = 1/f_r, (ii) the value of $\bar{I}_d$ is directly measured by the power supply and transmitted to the controller and (iii) the waveforms of I_d are post-processed after the deposition. As the O_2 inlet valves were periodically switched on and off, the nominal of $\bar{I}_d$ varied significantly on the timescale of seconds, which is captured in Fig. 5.17 (p. 93). The oscillations of the magnitude of target power density, $\bar{S}_d$, were of the same order of magnitude as the oscillations in $\bar{I}_d$ because of a fixed U_d. To allow for a quantitative comparison of the process properties, the average target power density $\langle \bar{S}_d \rangle$, defined as

$$\langle \bar{S}_d \rangle = \frac{1}{t_{End} - t_{Start}} \int_{t_{Start}}^{t_{End}} U_d(t) \frac{I_d(t)}{A_t} dt \approx \frac{U_d}{t_{End} - t_{Start}} \int_{t_{Start}}^{t_{End}} \bar{I}_d(t) dt = \frac{U_d}{A_t} \langle \bar{I}_d \rangle \qquad (5.8)$$

was chosen as the parameter of the deposition process. Here, t_{Start} and t_{End} are the start and end times of the deposition and $\langle \bar{I}_d \rangle$ is the average discharge current. The same integral formula as Eq. 5.8 (p. 94) was employed to calculate the average flow rate of the reactive gas into the chamber, $\langle Q \rangle$. Because of principal limitations in a direct measurement of $\langle \bar{S}_d \rangle$, the sliding average of $\bar{S}_d$ over n control cycles, $\langle \bar{S}_d \rangle_n$, was evaluated each time a new 'control cycle' started and was used as a process parameter instead of $\langle \bar{S}_d \rangle$ that was computed after the deposition. The beginning of each control cycle was defined as the moment the reactive gas entered the system. For example in Fig. 5.17 (p. 93) the control cycle starts at time t = 0 s and finishes at time t ≈ 6 s. Furthermore, let T_i be the duration of i-th control cycle and L the index of the last control cycle (due to the system's dynamics, the time spans of a particular control cycles differed on the order of tenths of second). Then, $T_n = \sum_{i=L-n+1}^{L} T_i$ denotes the time span of the last n control cycles and $\langle \bar{S}_d \rangle_n$ is calculated via the formula

$$\langle \bar{S}_d \rangle_n = \frac{1}{T_n} \int_{t_L - T_n}^{t_L} U_d(t) I_d(t) dt \approx \frac{U_d}{T_n} \int_{t_L - T_n}^{t_L} \bar{I}_d(t) dt \quad . \qquad (5.9)$$

Here, t_L is the time of the end of the last complete control cycle. The calculation according to Eq. 5.9 (p. 94) was embedded into the control algorithm and used to evaluate the $\langle \overline{S}_d \rangle_n$ value from the last 10 control cycles. As mentioned above, in Fig. 5.17 (p. 93) apparently it is seen that the discharge characteristics, i.e. time evolutions of (i) the mean value of the discharge current, $\overline{I}_d$, and of (ii) the mean value of the target power density, $\overline{S}_d$, were very sensitive to the settings of the independent process parameters which were operated by the control system, see Sec. 4.3.3 (p. 51).

$\langle \overline{S}_d \rangle_n$ was chosen as a fixed process parameter. Therefore, series of experiments were necessary to identify an appropriate settings of the control system to allow for the deposition of the films with desired optical transparency at a particular value of $\langle \overline{S}_d \rangle$. $\langle \overline{S}_d \rangle$ was set to 50 Wcm^{-2}.

5.2.2 Discharge characteristics

'Low-transparency' films (i.e. 'more-metallic' process) and 'high-transparency' films ('less-metallic' process) were deposited at the corresponding values of $\langle \overline{S}_d \rangle$ equal to 49.4 Wcm^{-2} and 51.3 Wcm^{-2}, respectively (Fig. 5.17 [p. 93]). From Fig. 5.17 (p. 93) it is apparent that the oscillations in the magnitude of $\overline{I}_d$ were more pronounced for the 'less-metallic' process and the minimum values of $\overline{I}_d$ were lower than in the case of the 'more-metallic' process even though the maximum values of Q were the same for both regimes. This feature is caused by a lower U_d and by system's inertia (see a further decrease in $\overline{I}_d$ after the reactive gas was let in). The maxima in $\overline{I}_d$ reached higher values during the 'less-metallic' regime causing more profound changes in the chemical composition of the target surface that, in turn, influenced the current-voltage characteristics of the discharge and the effective sputtering yield of the target (i.e. the target sputter-cleaning). The same argumentation gives an explanation for a longer duration of the control cycle in the case of 'less-metallic' regime, which is also captured in Fig. 5.17 (p. 93).

To gain understanding of the time evolution of the discharge characteristics, the waveforms of I_d and U_d were sampled at times 0 s, 2 s and 4 s after the moment the reactive gas was let in the system, see Fig. 5.17(b) (p. 93) and Fig. 5.18 (p. 96). Comparing the shape and the magnitude of the waveforms measured during reactive HiPIMS sputtering of ZrO_x (Fig. 5.18 [p. 96]) with the waveforms captured during non-reactive HiPIMS of Zr at similar conditions, i.e. $\overline{S}_d$ = 50 Wcm^{-2}, f_r = 500 Hz and t_1 = 200 μs (Fig. 5.2 [p. 69]) it can be stated that: (i) the general shape of the waveforms remained unchanged, (ii) the magnitudes of the U_d waveforms ware relatively close and (iii) the magnitude of the I_d waveform varied significantly during reactive sputtering, particularly in the case of 'less-metallic' process. Evaluating the maximum values of J_t that were achieved during the reactive HiPIMS depositions gives J_t = 1.9 Acm^{-2} for the 'more-metallic' process and J_t = 3.2 Acm^{-2} for the 'less-metallic' process which is much higher than J_t = 1.5 Acm^{-2} attained in the case of a non-reactive deposition.

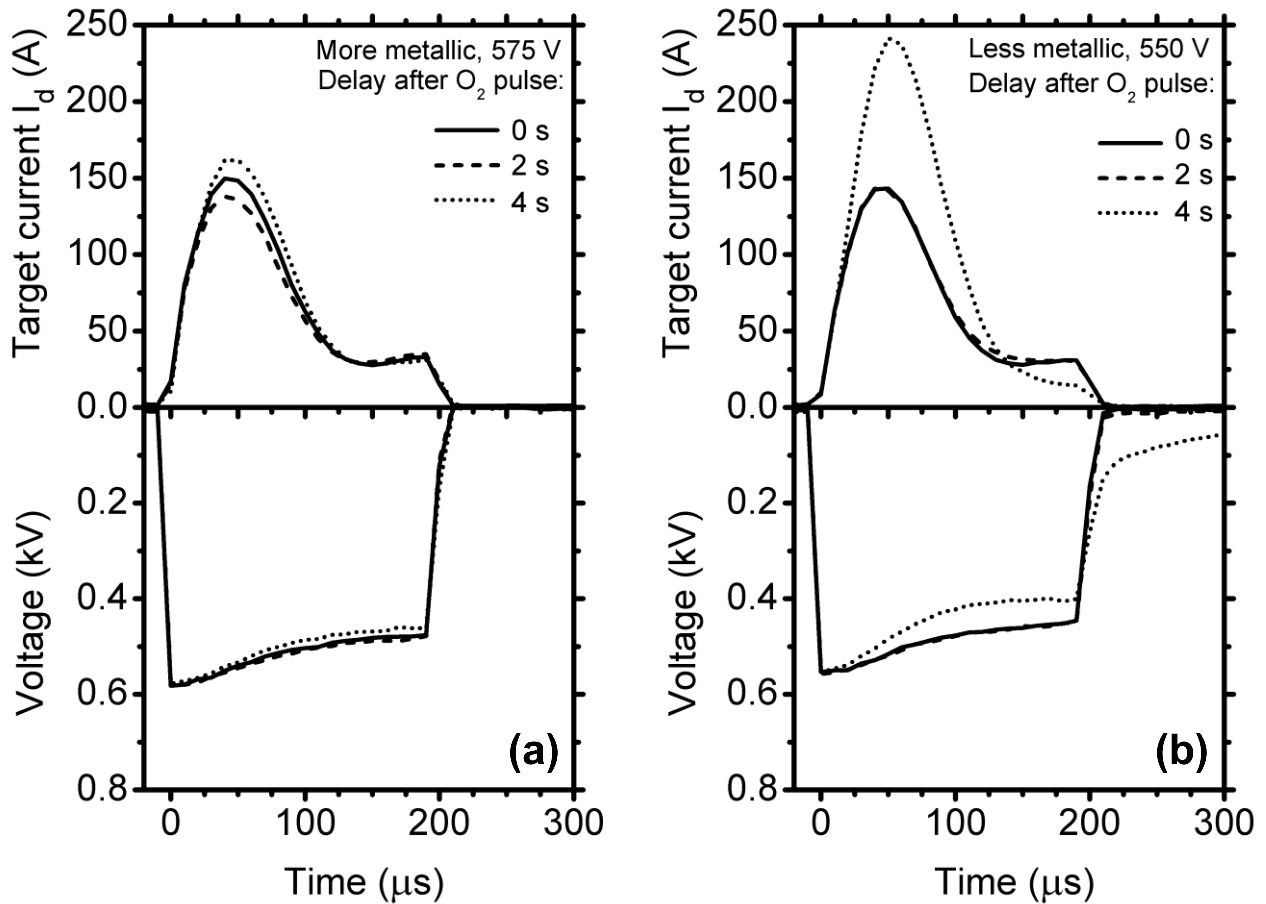

Fig. 5.18

Time evolutions of discharge current, I_d, and discharge voltage, U_d, sampled in the times 0 s, 2 s and 4 s after the moment the oxygen was let in the system, see Fig. 5.17 (p. 93). The maximum values of target current density, J_t, gives **(a)** 1.9 Acm^{-2} for 'more-metallic' mode and **(b)** 3.2 Acm^{-2} for 'less-metallic' regime which is much higher than J_t = 1.5 Acm^{-2} attained in the case of non-reactive deposition under the same value of average target power density $\overline{S}_d$ = 50 Wcm^{-2}. Presented waveforms are averaged over 10 measurements.

Experimental conditions: pulsed DC discharge, repetition frequency f_r = 500 Hz, argon process-gas pressure p = 2 Pa at a flow rate of 30 sccm.

Comparing the average oxygen flows into the system, $\langle Q \rangle$, which were 10.95 sccm when 'low-transparency' films were deposited and 11.32 sccm during the deposition of layers exhibiting 'high-transparency' demonstrates that the film properties are very sensitive to this parameter. Even such a minor variation in the value of $\langle Q \rangle$ (3.7%) is to be achieved by changing some of the control system's parameters significantly (the magnitude of the crucial parameters of the control system varied by 15%) making it possible to set the deposition conditions in an accurate way. Nevertheless, the dynamics of the

system varied on the order of minutes, mainly because of (i) a continuing target poisoning and (ii) the disappearing anode effect taking place in the single magnetron system used [89]. Employing a dual magnetron system would be beneficial from the point of view of the process stability. The oscillations of the O_2 partial pressure during the reactive deposition were lower than 0.1 Pa which was the resolution of the employed capacitive gauge under the conditions of a strong signal interference caused by the discharge current variations and by unavoidable arcing at the surface of the target.

5.2.3 Ion energies and compositions of total ion fluxes

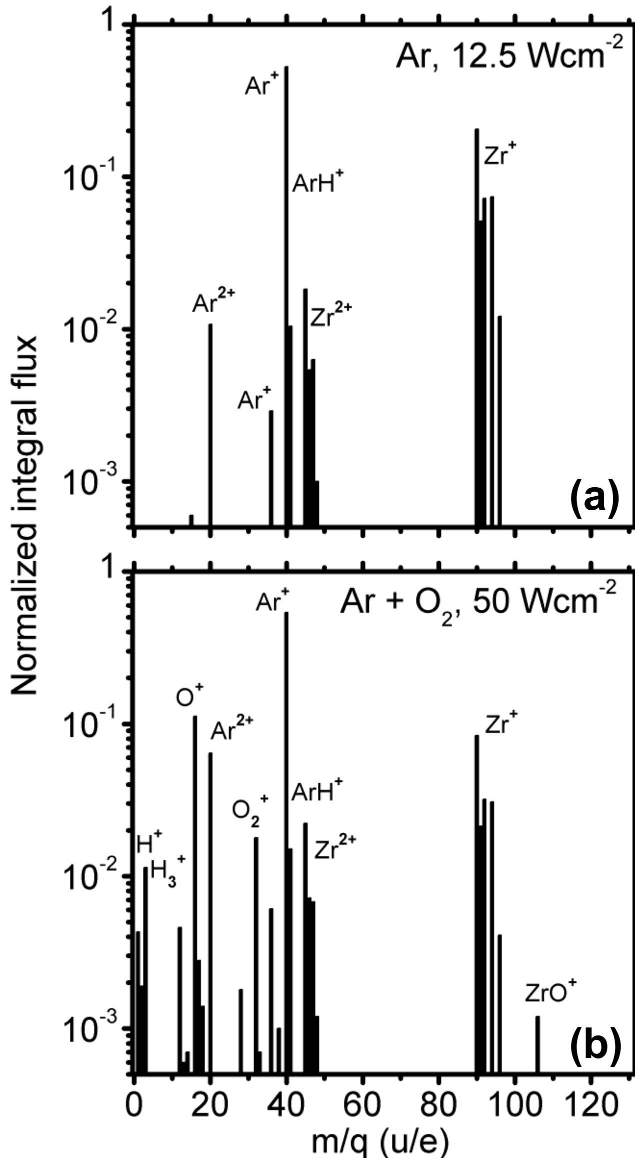

Fig. 5.19
Normalized integral fluxes of positive ions with kinetic energies in the range from -2 eV to 20 eV.
(a) Zirconium target sputtered in argon process gas at an average target power density $\overline{S}_d$ = 12.5 Wcm^{-2}. Note the substantial fraction of ArH^+ molecular ion complex.
(b) Zirconium target sputtered under the conditions of a 'less-metallic' regime (films exhibiting 'high-transparency'), $\overline{S}_d$ = 50 Wcm^{-2}, average oxygen flow rate $\langle Q \rangle$ = 10.0 sccm.
Presented data are averaged over 10 measurements.
Experimental Conditions: pulsed DC discharge, repetition frequency f_r = 500 Hz, pulse duration t_1 = 200 μs, argon process-gas pressure p = 2 Pa at a flow rate of 30 sccm, target-to-orifice distance d = 100 mm.

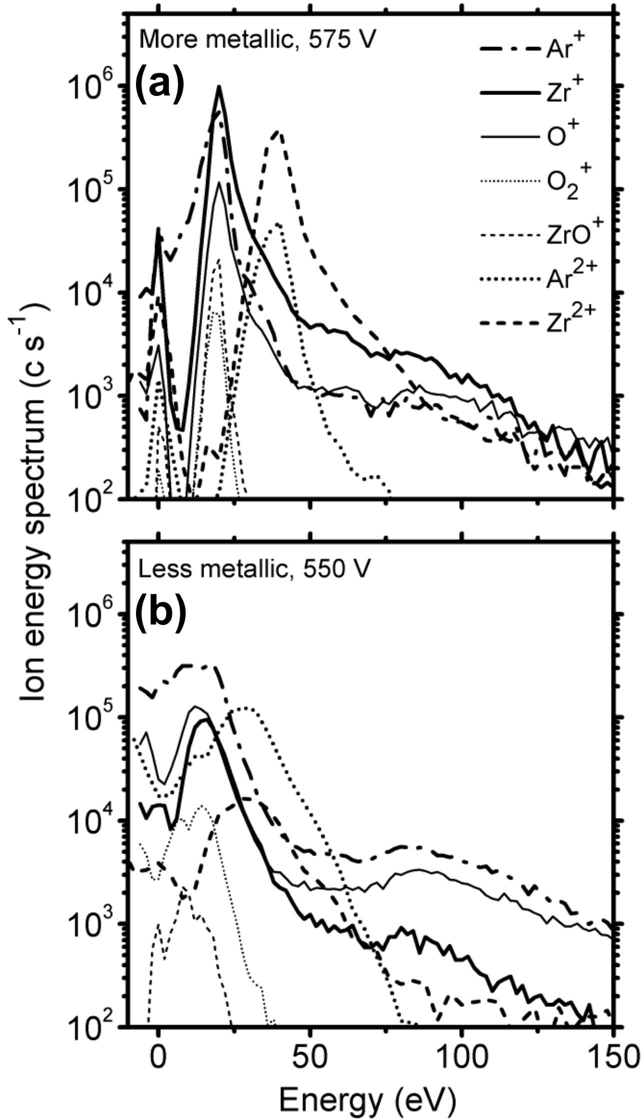

Fig. 5.20
Time-averaged ion energy spectra (IESs) of selected ionic species at the substrate position (target-to-orifice distance d = 100 mm). Respective values of average power density in a period, $\langle \overline{S}_d \rangle$, and average oxygen flow rate, $\langle Q \rangle$, were (see Fig. 5.17 [p. 93]):

(a) 'More-metallic' regime ('less transparent' films) $\langle \overline{S}_d \rangle$ = 49.4 Wcm^{-2}, $\langle Q \rangle$ = 10.95 sccm

(b) 'Less-metallic' regime ('highly transparent' films) $\langle \overline{S}_d \rangle$ = 51.3 Wcm^{-2}, $\langle Q \rangle$ = 11.32 sccm

Presented data are averaged over 20 measurements. **Experimental conditions**: pulsed DC discharge, repetition frequency f_r = 500 Hz, pulse duration t_1 = 200 μs, argon process-gas pressure p = 2 Pa at a flow rate of 30 sccm.

Prior to the measurements of the energy spectra (IESs) of a particular ionic species, the overall composition of the background atmosphere and the composition of the flux of positively charged ionic species were investigated to determine the system's contamination and to identify the most abundant ionic species (i.e., the spectrometer was operated in the RGA and the SIMS modes, respectively, see Sec. 4.1.1 [p. 21]). The results of the measurements of the neutral gas species are presented in Fig. 4.13 (p. 38) and the main contaminants were identified as H_2, C, H_2O, N_2 and CO_2. The relatively high H_2O signal is a common feature of the vacuum systems operating in the pressure range used because of a strong adsorption of H_2O molecules to the surfaces of the deposition system (Fig. 4.11 [p. 36]) [131]. As the Zr target is being sputtered in Ar process gas of a total pressure of 2 Pa at $\overline{S}_d$ = 12.5 Wcm^{-2}, see Fig. 5.19(a) (p. 97), the ionic flux at the substrate position is composed mostly of the Ar and Zr ions and of a substantial fraction of ArH^+ molecular ion complex. Performing the same scan under the conditions of a 'less-metallic' regime, as defined in the preceding text ($\langle \overline{S}_d \rangle$ = 50 Wcm^{-2}), the flux of reactive-gas ions

(O_2^+, O^+) and target-material-reactive-gas molecular ions (ZrO^+) were detected, see Fig. 5.19(b) (p. 97). The fluxes of H^+, H_2^+, H_3^+, C^+, OH^+ and H_2O^+ ions detected under these conditions are to be explained by (i) lower gettering of contaminating species by sputtered target-material due to its consumption by the reaction with the reactive gas and by (ii) elevated thermal loading of the system resulting in its additional bake-out. Note that during the depositions the system pumping speed is lowered to reach the necessary pressures of working atmosphere and, therefore, possible leakages which are present in the vacuum system can play a role.

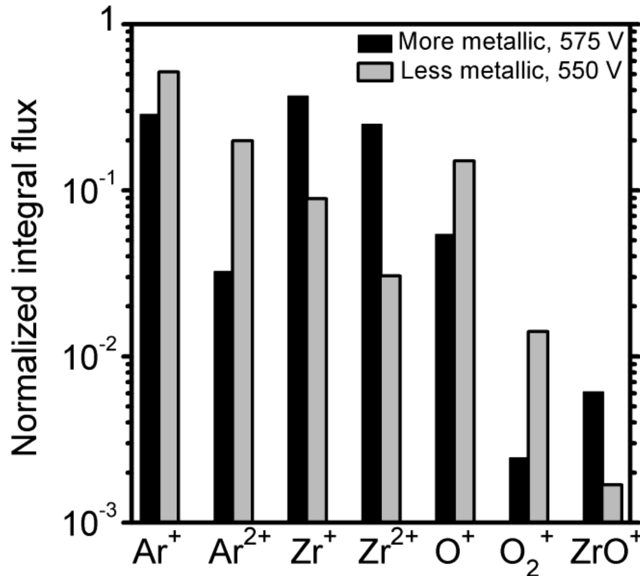

Fig. 5.21
Integral fluxes of selected ionic species with energies in the range from -5 eV to 150 eV (see Fig. 5.20 [p. 98]) at the substrate position (target-to-orifice distance d = 100 mm). Respective values of average target power densities, $\langle \overline{S}_d \rangle$, and average oxygen flow rates, $\langle Q \rangle$, were (Fig. 5.17 [p. 93]): $\langle \overline{S}_d \rangle$ = 49.4 Wcm^{-2}, $\langle Q \rangle$ = 10.95 sccm in the 'more-metallic' regime 'low-transparency' films) and $\langle \overline{S}_d \rangle$ = 51.3 Wcm^{-2}, $\langle Q \rangle$ = 11.32 sccm in the 'less-metallic' regime 'high-transparency' films). Presented data are averaged over 20 measurements. **Experimental conditions**: pulsed DC discharge, repetition frequency f_r = 500 Hz, pulse duration t_1 = 200 μs, argon process-gas pressure p = 2 Pa at a flow rate of 30 sccm.

The IESs of the ionic species of major interest (Ar^+, Ar^{2+}, Zr^+, Zr^{2+}, O^+, O_2^+, ZrO^+) were measured in a time-averaging mode, see Fig. 5.20 (p. 98), and in time-resolving mode, meaning that the spectra acquisition procedure was running throughout the entire control cycle (time-averaging) and also throughout three particular time intervals (time-resolving), as indicated in Fig. 5.17(c) (p. 93). Since no remarkable variations in the shape of the IESs were detected in time-resolving mode, only the information on the time-averaged IESs is presented here. Comparing these IESs to the IEDFs acquired during non-reactive HiPIMS of Zr, see Fig. 5.5 (p. 75) and Fig. 5.8 (p. 82), it is apparent that the maxima in corresponding spectra were shifted towards higher energies during the reactive sputtering process. In the case of non-reactive sputtering, the maxima were detected at approximately 4 eV for singly charged ions and 8 eV for doubly charged ions, which are much lower values than the 20 eV and 40 eV, respectively,

measured in the case of reactive HiPIMS. This observation indicates a shift in the value of plasma potential at the distance of 100 mm from the target, where the spectrometer's orifice was located, and is to be qualitatively explained via the 'disappearing anode' effect as follows.

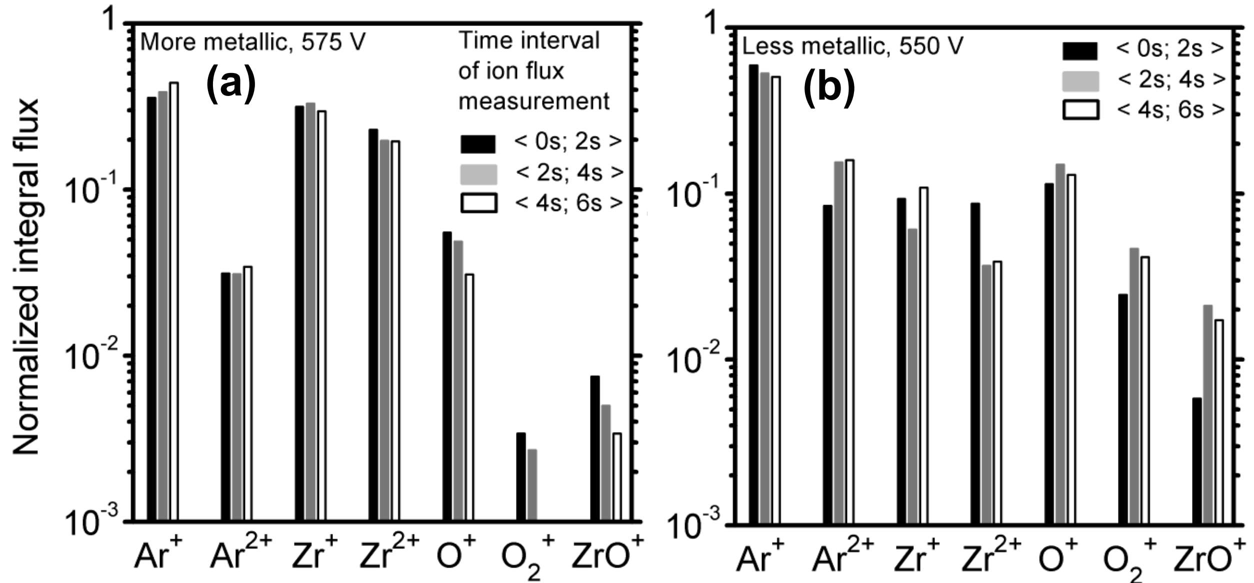

Fig. 5.22
Integral fluxes of selected ionic species with energies ranging from -5 eV to 150 eV at the substrate position (target-to-orifice distance d = 100 mm). Ion fluxes were measured in three different 2 s lasting time windows starting after the moment the oxygen was let in the system, Fig. 5.17 (p. 93). Respective values of the average target power density in a period, $\langle \overline{S}_d \rangle$, and average oxygen flow rate, $\langle Q \rangle$, were **(a)** $\langle \overline{S}_d \rangle$ = 49.4 Wcm^{-2}, $\langle Q \rangle$ = 10.95 sccm in the 'more-metallic' regime ('low-transparency' films) and **(b)** $\langle \overline{S}_d \rangle$ = 51.3 Wcm^{-2}, $\langle Q \rangle$ = 11.32 sccm in the 'less-metallic' regime ('high-transparency' films). Presented data are averaged over 5 measurements. The magnitudes of respective ion energy distributions exhibited large variations ranging from 40% in the case of Ar^+ up to 90% in the case of ZrO^+ ions.
Experimental conditions: pulsed DC discharge, repetition frequency f_r = 500 Hz, pulse duration t_1 = 200 μs, argon process-gas pressure p = 2 Pa at a flow rate of 30 sccm.

On the surfaces within the chamber, the insulating layer of ZrO_x is formed which impedes the electric current to be drawn from the plasma. As a result, the impedance of the respective circuit rises and the electric potential is changed in a space domain close to the substrate causing a shift in a potential difference between the grounded sampling orifice of the spectrometer and the plasma. From these measurements it follows that the spatial distribution of the plasma potential is different for reactive and

non-reactive sputtering processes and may have an impact on the kinetic energy of the ions striking the substrate and the target.

After measuring the IESs (see Fig. 5.20 [p. 98]), the total ion fluxes were evaluated and these are shown in Fig. 5.21 (p. 99) and in Fig. 5.22 (p. 100). In the case of the 'more-metallic' process, the ionic flux is formed predominantly by the Zr ions and, on the other hand, during the 'less-metallic' mode, the most abundant ions were Ar and oxygen ions. In both cases the flux of oxygen ions was dominated by O^+ ions showing a strong dissociation of O_2 molecules that was even more profound in the 'more-metallic' mode. Regarding the ZrO^+ ions, the data presented in Fig. 5.21 (p. 99) may seem to be contrary to those shown in Fig. 5.22 (p. 100). Performing the time-averaging scan, the relative flux of ZrO^+ ions was found to be higher in the 'more-metallic' mode and, on the other hand, the time-resolving scans indicate the higher relative flux of ZrO^+ ions in the 'less-metallic' mode. To explain this contradiction, it must be stated that variations that were not reproducible were observed in time-resolving IESs for each of the 2 s lasting acquisition intervals. In addition to that, the individual IESs in both time-averaging and time-resolving acquisition modes were detected. These were the main reasons for not present the time-resolving IESs and for scanning IESs more times and a subsequent averaging.

Nevertheless, the strong scatter in the total ion fluxes of all ionic species was unavoidable due to the limited number of measured IESs. To quantify this scatter, the measured signal (in the units of counts per second, cs^{-1}) was summed for each IES (meaning that the total ionic fluxes were evaluated) and the relative value of standard deviation of the respective set of IESs was calculated for each ionic specie. This procedure provided the following results: (i) the sets of 20 time-averaged scans exhibited a 20% deviation in the signal of Ar^+ ions, 30% deviation in the signal of Ar^{2+}, Zr^+ and Zr^{2+} ions, 60% deviation in the signal of O^+ ions and up to 90% deviation in the signal of O^{2+} and ZrO^+ ions, (ii) the sets of 5 time-resolved scans (5 scans for each 2 s acquisition interval and for each ionic specie, see Fig. 5.17 [p. 93]) exhibited 40% deviations in the signal of Ar^{1+} ions, up to 70% deviations in the signal of Ar^{2+}, Zr^+, Zr^{2+}, O^+ and O^{2+} ions and, again, even 90% deviations in the signal of ZrO^+ ions. These strong variations in individual IESs were attributed to the long-term evolution of the properties of the deposition system and to unavoidable arcing events at the target surface. Comparing the magnitude of the scatter in the measured IESs and the fluctuations in the composition of the total ionic fluxes, see Fig. 5.22 p. (100), it can be stated that no reproducible trend in the composition of the total ionic flux within the control cycle was detected at the substrate position.

Note that the total ion fluxes are presented in the normalized form since the substrate current density, J_s, was not measured and, thus, total flux of the ions onto the substrate were unknown. Consequently, the comparison of the magnitudes of particular ion fluxes for the cases of the 'more-metallic' and the 'less-metallic' regimes at the distance of 100 mm from the target should be done carefully. Moreover, as far as time-resolved measurements are considered, the varying magnitudes of $\bar{I}_d$ (and corresponding variations in the magnitudes of ionic fluxes) in different phases of the control cycle must be taken into account.

5.3 Reactive HiPIMS depositions of zirconium-oxide films

In this section, the results of experiments on controlled reactive HiPIMS depositions of zirconium-oxide (ZrO_x) films are presented. Then, properties of deposited films are discussed. The discharge was operated for several values of the target power density and pulse-on times in the system of geometry introduced in Sec. 4.3 (p. 46) employing the control system described therein.

5.3.1 Discharge characteristics

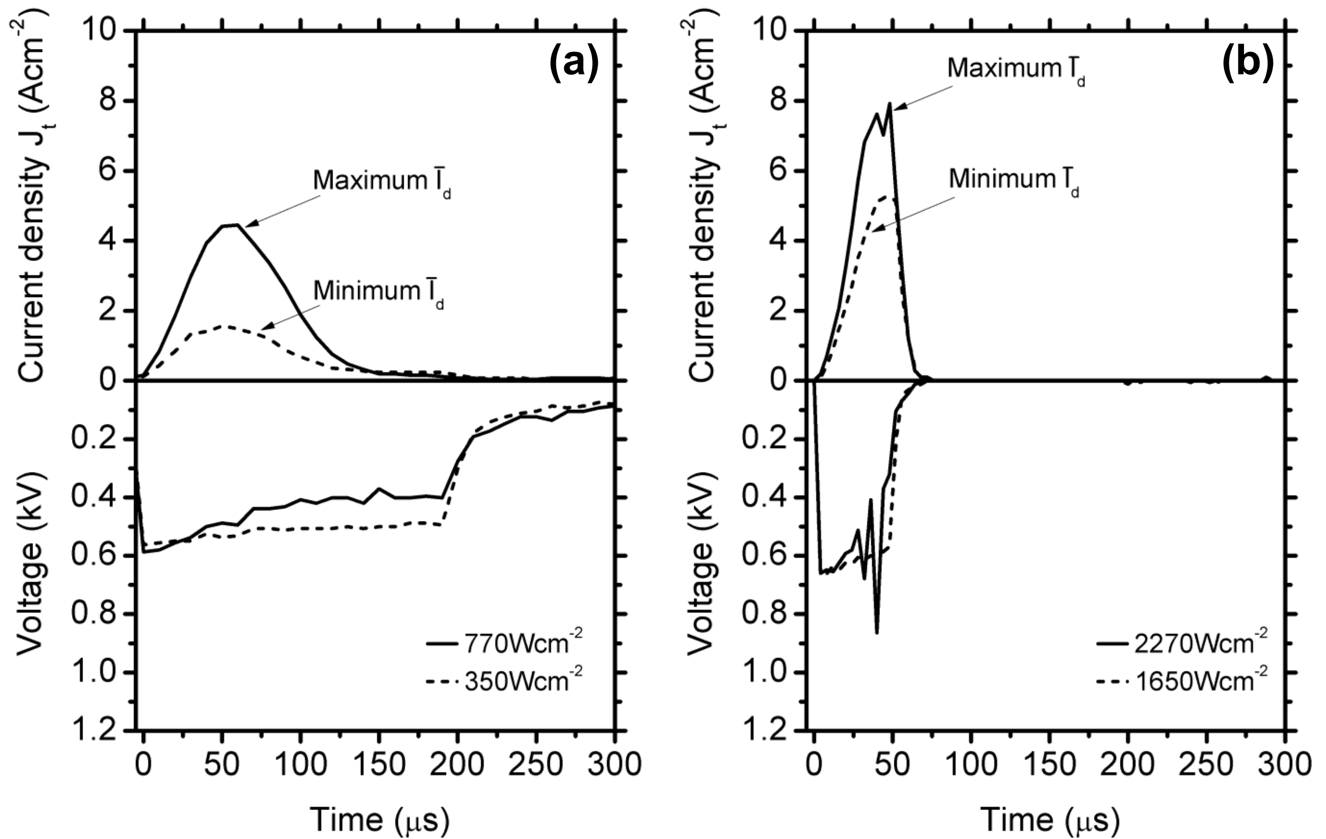

Fig. 5.23
Waveforms of the magnetron voltage, U_d, and the target current density, J_t, for the preset average target power density in a period $\langle \bar{S}_d \rangle$ = 50W cm^{-2} and a voltage pulse duration **(a)** t_1 = 200 μs with the average pulse target power densities S_{da} = 350 Wcm^{-2} and 770 Wcm^{-2}, **(b)** t_1 = 50 μs with S_{da} = 1650 Wcm^{-2} and 2270 Wcm^{-2}, corresponding to the minimum and maximum discharge current, $\bar{I}_d$, respectively, during a controlled high-rate reactive deposition of highly transparent zirconium dioxide films.
Experimental conditions: repetition frequency f_r = 500 Hz, argon process-gas pressure p = 2 Pa at a flow rate of 30 sccm.

Analogously to the non-reactive HiPIMS depositions of Zr (Sec. 5.1 [p. 67]), reactive depositions of ZrO_x films were performed changing the process parameters in two steps. Firstly, the pulse-on time, t_1, was fixed at 200 μs (10% duty cycle) and the average target power density in a period, $\langle \overline{S}_d \rangle$, was raised from approximately 5 Wcm^{-2} to 100 Wcm^{-2}. Secondly, $\langle \overline{S}_d \rangle$ was fixed at approximately 50 Wcm^{-2} and t_1 was shortened from 200 μs down to 50 μs (2.5% duty cycle). It should be recalled that the measurement and control of the exact value of $\langle \overline{S}_d \rangle$ was more complicated than in the case of non-reactive HiPIMS, see Sec. 5.2.1 (p. 93).

The time evolutions (waveforms) of the magnetron voltage, U_d, and the target current density, J_t, were similar to those measured in the case of non-reactive depositions performed under corresponding conditions (see Sec. 5.1.1 [p. 68]). Therefore, it is sufficient to present representative evolutions of U_d and J_t during pulses at a preset average target power density in a period $\langle \overline{S}_d \rangle$ = 50 Wcm^{-2}. In Fig. 5.23 (p. 102), the respective time evolutions are shown for voltage pulse-on durations t_1 = 200 μs and 50 μs. The corresponding ranges of the average pulse target power densities S_{da} = 350 – 770 Wcm^{-2} and S_{da} = 1650 – 2270 Wcm^{-2} for the corresponding controlled reactive depositions of 'high-transparency' ZrO_2 films are also given.

5.3.2 Deposition rates and optical properties of zirconium-oxide films

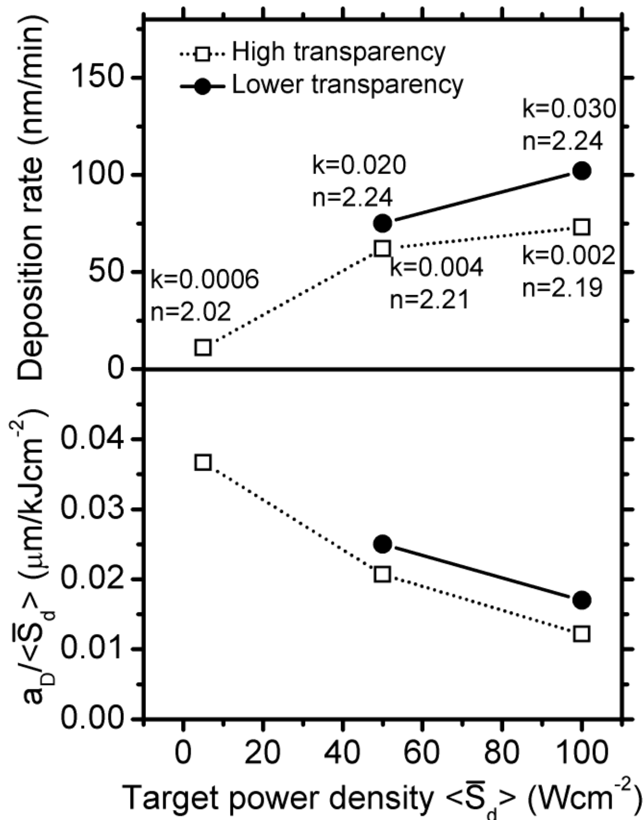

Fig. 5.24

Deposition rate, a_D, and deposition rate per average target power density in a period, $a_D/\langle \overline{S}_d \rangle$, as functions of the $\langle \overline{S}_d \rangle$ value for a voltage pulse duration t_1 = 200 μs and a target-to-substrate distance d = 100 mm. The extinction coefficient, k, and the refractive index, n, measured at λ = 550 nm, for the corresponding 'high-' and 'low-transparency' zirconium-oxide films are also given.

Experimental conditions: pulsed DC discharge, repetition frequency f_r = 500 Hz, argon process-gas pressure p = 2 Pa at a flow rate of 30 sccm.

Fig. 5.24 (p. 103) shows that an increase in $\langle \overline{S}_d \rangle$ from 5 Wcm^{-2} to 100 Wcm^{-2} at the same duty cycle of 10% resulted in a rapid rise in the deposition rate, a_D, of 'high-transparency' ZrO_2 film from 11 nm/min to 73 nm/min. However, the deposition rate per average target power density in a period decreased 3 times for these films. The density of the 'high-transparency' ZrO_2 films increased with the $\langle \overline{S}_d \rangle$ value from 5.1 gcm^{-3} to about 5.86 gcm^{-3}, being the density of the monoclinic bulk ZrO_2 material. As expected, systematically higher deposition rates were achieved for the corresponding 'low-transparency' (see the higher extinction coefficients, k) ZrO_x films. Their density was approximately 6.2 gcm^{-3}.

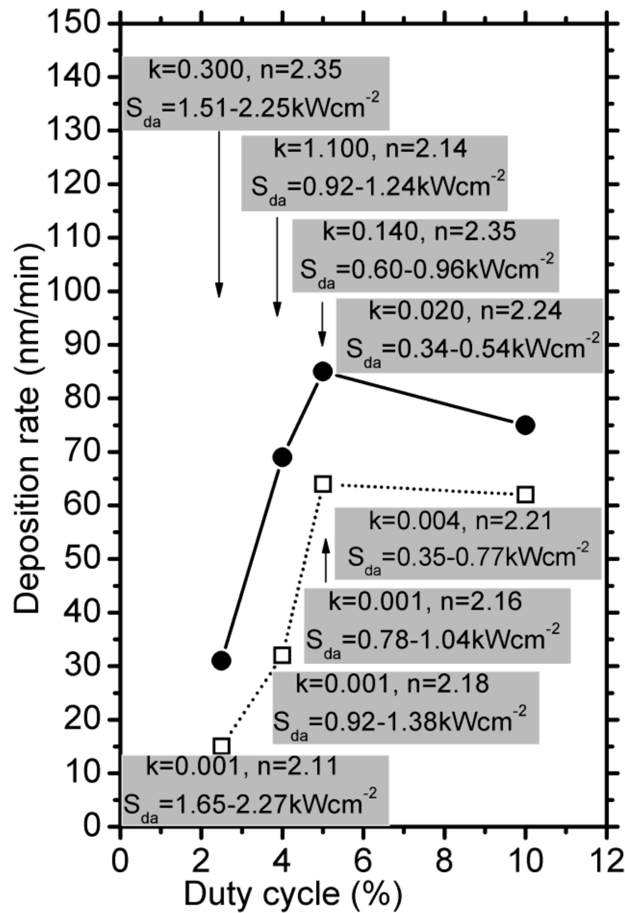

Fig. 5.25
Deposition rate, a_D, as a function of the duty cycle for the preset average target power density in a period $\langle \overline{S}_d \rangle$ = 50 Wcm^{-2} at increasing voltage pulse durations, t_1, from 50 µs to 200 µ at the target-to-substrate distance d = 100 mm. The extinction coefficient, k, and the refractive index, n, measured at λ = 550 nm, for the corresponding 'high-' (empty symbols) and 'low-' (full symbols) transparency zirconium-oxide films prepared at the average pulse target power densities, U_d, in the ranges denoted are also given.
Experimental conditions: pulsed DC discharge, repetition frequency f_r = 500 Hz, argon process-gas pressure p = 2 Pa at a flow rate of 30 sccm.

As can be seen in Fig. 5.25 (p. 104), an increased target power density S_{da} in shortened voltage pulses (the duty cycle decreased from 5% to 2.5%) at the same $\langle \overline{S}_d \rangle$ = 50 Wcm^{-2} led to a reduced a_D of the 'high-transparency' ZrO_2 films from 64 nm/min to 15 nm/min. Their density was close to that of the monoclinic bulk ZrO_2 material for t_l/T = 4% – 10%, while it was 5.1 gcm^{-3} for t_l/T = 2.5%. A similar dependence of the a_D on the duty cycle, but with systematically higher a_D values, was obtained for the

corresponding 'low-transparency' (see the higher extinction coefficients) ZrO_x films with the density of about 6.2 gcm^{-3}.

5.3.3 Elemental composition and structure of zirconium-oxide films

Taking into account the 5 – 7 at.% accuracy of the measurements, we can conclude that the stoichiometric ZrO_2 composition was achieved for the 'high-transparency' films with $k \leq 4\times10^{-3}$ (see Fig. 5.26 [p. 105]). They exhibited a crystalline structure with a predominant monoclinic phase (see Fig. 5.27 [p. 106]). For the most energetic pulses at t_1 = 50 μs and $\langle \overline{S_d} \rangle$ = 50 Wcm^{-2} (see Fig. 5.25 [p. 104]), they were found to be nanocrystalline with a higher contribution of the tetragonal ZrO_2 phase. Their hardness was between 10 GPa and 15 GPa.

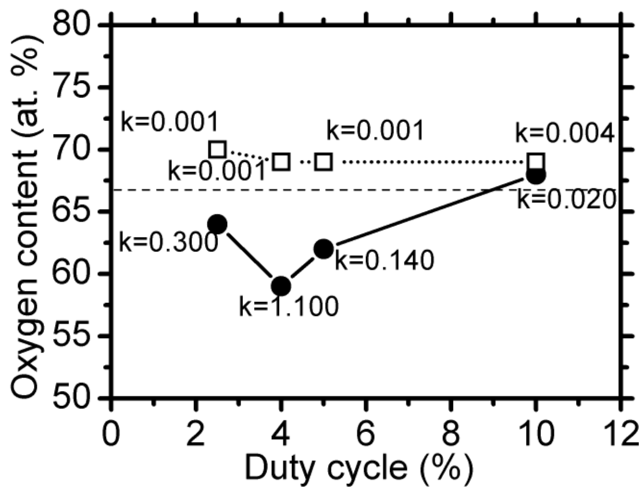

Fig. 5.26
Elemental composition and the extinction coefficient, k, measured at λ = 550 nm, for the corresponding 'high-' (empty symbols) and 'low-' (full symbols) transparency zirconium-oxide films.
Deposition conditions: pulsed DC discharge, repetition frequency f_r = 500 Hz, target power density in a period $\langle \overline{S_d} \rangle$ = 50 Wcm^{-2}, target power densities, S_{da} , are given in Fig. 5.25 (p. 104), target-to-substrate distance d = 100 mm, argon process-gas pressure p = 2 Pa at a flow rate of 30 sccm.

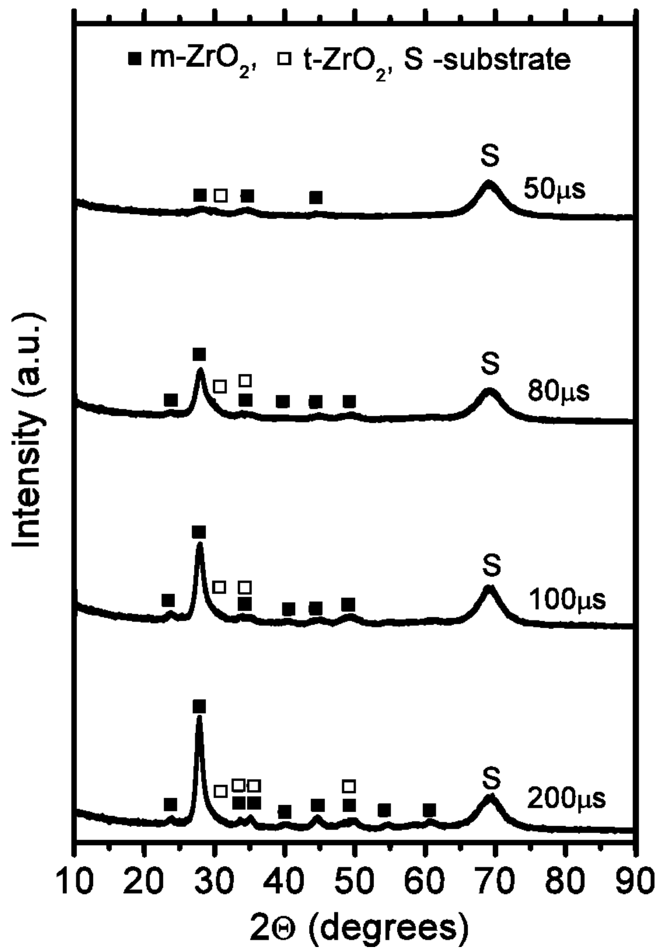

Fig. 5.27
X-ray diffraction patterns taken from the highly transparent zirconium dioxide films.
Deposition conditions: target power density in a period $\langle \overline{S}_d \rangle$ = 50 Wcm^{-2}, target power densities, S_{da} , are given in Fig. 5.25 (p. 104), target-to-substrate distance d = 100 mm, argon process-gas pressure p = 2 Pa at a flow rate of 30 sccm.

5.4 Mathematical modeling of controlled reactive HiPIMS depositions of zirconium oxides

The model assumptions and governing equations are introduced in Sec. 4.6 (p. 55). In this section, the results of the mathematical model of the reactive magnetron sputtering processes are presented. The steady-state model of reactive deposition and model of the dynamics of the controlled deposition were employed to simulate the sputtering process. Then, the performance and capabilities of the applied control method, see Sec. 4.3.3 (p. 51), are discussed in light of these results.

5.4.1 Parameters of the model

The list of the model parameters and their respective values are given in Table 5.5 (p. 108). As described in Sec. 4.6.2 (p. 64), the only parameters of the applied mathematical model that were assessed experimentally were the pumping outlet area, A_p, and the number of adsorption sites, Ns, for oxygen molecules (O_2). The former was evaluated as 3.3×10^{-4} m^2 setting q_f = 30 sccm and p_{RG} = 2 Pa in Eq. 4.59 (p. 64). The latter, Ns, was fitted using the Eq. 4.61 (p. 66) and Eq. 4.62 (p. 66) making use of HiPIMS discharge, f_r = 500 Hz, t_l = 200 µs, U_d = 450 V, I_d = 3.5 A, p = 2 Pa of Ar process gas, q_f = 20 sccm of O_2 reactive gas (Fig. 5.28 [p. 109]) and setting $\gamma_{MEfromME}$ = 0.25. The sputtering experiment was repeated four times for t_{sp} = 10 s, 30 s, 60 s and 180 s. The corresponding t_{delay} were 2.5 s, 4.0 s, 8.0 s and 12.5 s, which resulted in the numerical fit N_s = 1.1×10^{20} (Fig. 5.29 [p. 109]). Setting the surface of collecting area A_c = 0.2 m^2, the surface density of adsorption sites for O_2 molecules was calculated as n_s = 5.5×10^{20} m^{-2}, which is approximately 50 times higher than the n_{sb} value calculated from bulk properties of Zr, see Eq. 4.46 (p. 60). Then, n_s gives a base rough estimate of the surface densities of adsorption sites for O_2 molecules on the target surface, n_{st} and collecting area surfaces, n_{sc}, see Fig. 5.29 (p. 109) and Table 5.5 (p. 108).

The values of sputtering yields were estimated based on the sputtering yields of the target material by the Ar^+ and Zr^+ ions, see Fig. 5.12 (p. 86), taking into consideration the reduced sputtering yields from the compound and the backward flux of ionized sputtered species towards the target. The ionization probabilities of the process-gas species (Eq. 4.34 [p. 57]) and the properties describing the interdependencies between target poisoning and the discharge current (Eq. 4.47 [p. 61]) were set based on the literature data and to fit the simulated and measured time evolutions of the discharge current, $\bar{I}_d$ [81-87,104]. For the particular cases of 'more-metallic' and 'less-metallic' regimes ('low-' and 'high-transparency' films) the values of I_d^0 = 4.8 A and 4.7 A were set, see Eq. 4.47 (p. 61).

Table 5.5

Parameters of the mathematical model used for simulations of the reactive sputtering process. See Sec. 4.6 (p. 55) for the exact meaning of the properties listed in the table.

			Deposition system geometry
V	0.2	(m^3)	Vacuum chamber volume
A_t	55.0	(cm^2)	Area of the target erosion zone
A_c	0.2	(m^2)	Area of the collecting surfaces
A_p	3.3	(cm^2)	Pumping aperture area
			Working atmosphere
p_{BG}	2.00	(Pa)	Background-gas pressure
β_{BG}	0.25		Relative ionization probability of the background-gas molecule
β_{RG}	0.75		Relative ionization probability of the reactive-gas molecule
			Sputtering yields
$\gamma_{MEfromME}$	0.250		Metallic atoms sputtered from metallic part of the target
$\gamma_{MEfromCOMP}$	0.025		Metallic atoms sputtered from compound part of the target
$\gamma_{RGAfromCOMP}$	0.100		Reactive-gas atoms sputtered from the target
$\gamma_{KnockRGAfromCOMP}$	0.030		Reactive-gas atoms "knocked" into the subsurface parts of the target
			Surface properties
n_{st}	3.7×10^{20}	(m^{-2})	Surface density of adsorption sites at the target area
n_{sc}	5.5×10^{20}	(m^{-2})	Surface density of adsorption sites at the collecting area
ΔI_d^{surf}	-0.9		Relative change of the discharge current due to compound formation on the target surface
ΔI_d^{below}	4.2		Relative change of the discharge current due to compound formation below the target surface
s	2		Number of monomolecular target layers treated as suface ones
b	5		Number of monomolecular target layers considered to influence the discharge current
			Sticking coefficients
α_{MEtoME}	1.0		Metallic atoms to metallic part of the surface
$\alpha_{MEtoCOMP}$	1.0		Metallic atoms to compound part of the surface
$\alpha_{RGAsptoMEc}$	1.0		Sputtered reactive-gas atoms to metallic part of the collecting area
$\alpha_{RGMtoMEt}$	0.3		Reactive-gas molecules to metallic part of the target
$\alpha_{RGMtoMEc}$	0.3		Reactive-gas molecules to metallic part of the collecting area

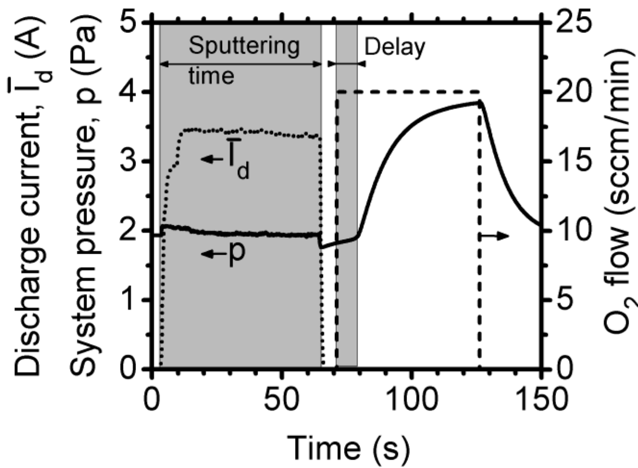

Fig. 5.28
Assessing the number of adsorption sites for oxygen molecules (O_2) in the deposition system. A zirconium target was sputtered in a pure-argon atmosphere. After the discharge was switched off, the O_2 reactive gas was let in the system and the 'delay' between the moment of the O_2 introduction and the moment of the pressure rise was detected providing information on the number of O_2 molecules adsorbed at the surfaces (Eq. 4.62 [p. 66]). The experiment was repeated four times for different values of 'sputtering time'.

Experimental conditions: pulsed DC discharge, discharge voltage U_d = 450 V, pulse repetition frequency f_r = 500 Hz, pulse duration t_1 = 200 μs, argon process-gas pressure p = 2 Pa at a flow rate of 20 sccm, O_2 flow rate q_f = 20 sccm.

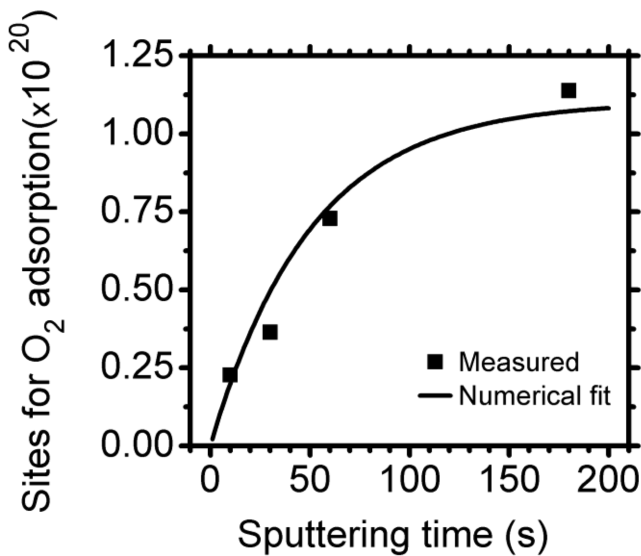

Fig. 5.29
Assessing the number of adsorption sites for oxygen molecules (O_2). For experimental details see Fig. 5.28 (p. 109). A zirconium target was sputtered in pure-argon atmosphere for 'sputtering time'. After the discharge was switched off, O_2 was introduced into the system. Then, a pressure increase was detected after 'delay' time. The number of adsorption sites for O_2 molecules was evaluated employing Eq. 4.62 (p. 66) (square symbols) and Eq. 4.61 (p. 66) was used to fit the data measured (full line).

5.4.2 Model results - process parameters and film stoichiometry

From the standpoint of the applicability of the model, it was of a primary interest to test the model's capability to simulate a real deposition process. Hence, the model parameters describing the physical properties of the deposition system were set as described in Sec. 5.4.1 (p. 107) and the parameters of the modeled controller were set identical to those used for real depositions, see Sec. 5.2.1 (p. 93) and Fig. 5.30 (p. 110). Some of the phenomena the model does not take into account are: (i) the 'sputtering wind', (ii) gas density reduction due to the 'pumping effect' of the magnetron target (see the discussion in Sec. 5.1.1 [p. 68]), (iii) non-homogeneity of the deposition flux, (iv) influence of the magnetic field on the flux of the charged particles and (v) a non-homogeneous distribution of the reactive gas within the chamber.

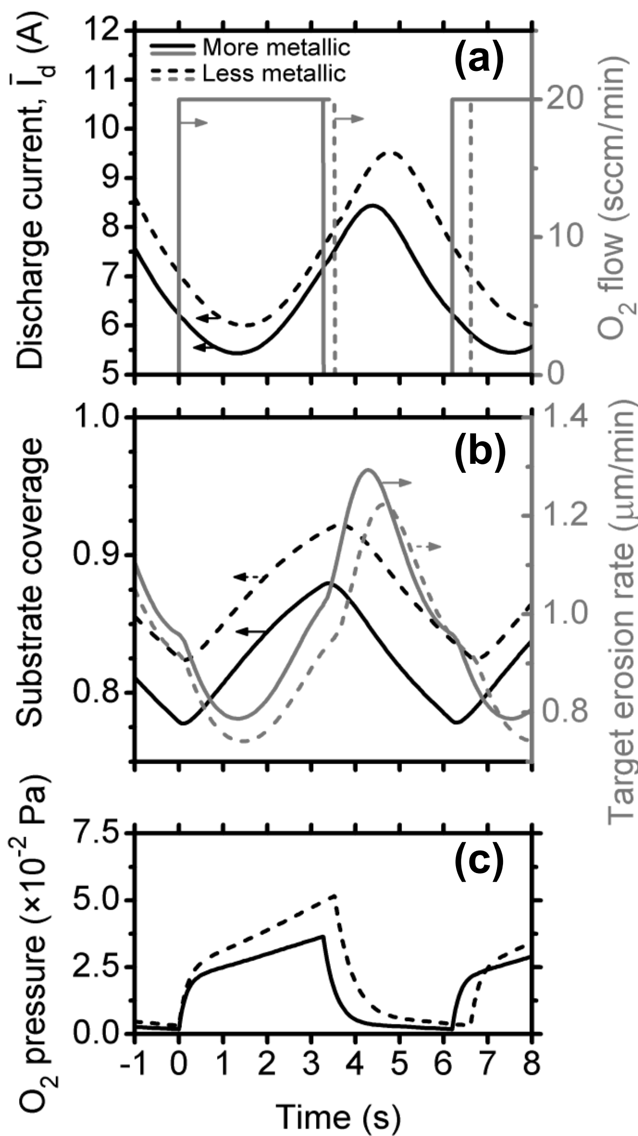

Fig. 5.30
Outputs of the mathematical model of the controlled reactive deposition processes. The controller settings were identical to those used in experiments (Fig. 5.17 [p. 93]). The outputs pertaining to the 'more-metallic' regime ('low-transparency' films, I_d^0 = 4.8 A, see Eq. 4.47, [p. 61]) are marked by full lines and the ones referring to the 'less-metallic' regime ('high-transparency' films, I_d^0 = 4.7 A, see Eq. 4.47, [p. 61]) are marked by dashed lines.
(a) Time evolution of the average discharge current in a period, $\bar{I}_d$, and the oxygen flow rate, Q. The mean values of the respective properties (see Eq. 5.8 [p. 94]), i.e. $\langle \bar{I}_d \rangle$ and $\langle Q \rangle$ were 6.7 A, 10.68 sccm for the 'more-metallic' and 7.5 A, 10.74 sccm for the 'less-metallic' regime.
(b) Time evolutions of substrate coverage, θ_c, as defined in Sec. 4.6.1 (p. 55) (film stoichiometry indicator) and target erosion rate (deposition rate indicator).
(c) Time evolutions of the oxygen partial pressure.
The parameters of the model were set as stated in Table 5.5 (p. 108).

Comparing the measured and modeled evolutions of the discharge current, $\bar{I}_d$, and the duration of the control cycle T_c, see Fig. 5.17(a) (p. 93) and Fig. 5.30(a) (p. 110), indicates that despite its simplicity the model is capable of predicting the system's behavior with a reasonable accuracy. Especially the system's inertia is captured as observed during real depositions, see (i) the decrease of $\bar{I}_d$ shortly after the reactive gas was let in the chamber and (ii) the longer duration of the control cycle, T_c,for the 'less-metallic' deposition. The surface densities of sites for reactive-gas adsorption, n_{st}, n_{sc}, and sputtering yields $\gamma_{MEfromCOMP}$, $\gamma_{MEfromME}$, $\gamma_{RGAfromCOMP}$, $\gamma_{KnockRGAfromCOMP}$ were identified as parameters having a substantial impact on the value of T_c. On the other hand, settings of the parameters of the $\bar{I}_d$ calculation (Eq. 4.47 [p. 61]), i.e. influence of the surface and subsurface target poisoning on the magnitude of the $\bar{I}_d$, was found to determine primarily the shape of the $\bar{I}_d$ waveform.

To assess the value of the deposition rate, a_D, the target erosion rate was evaluated using Eq. 4.45 (p. 60). In Fig. 5.30 (p. 110), the target erosion is provided in the units of µm/min. Then, assuming a homogeneous deposition of Zr sputtered from the target of area 55 cm^2 onto the collecting area of 0.2 m^2 and considering the deposited layer being formed from ZrO_2 (density 5680 kgm^{-3}) resulted in the ratio between a_D and target erosion rate to be 0.032. Consequently, considering the oscillating target erosion rates as shown in Fig. 5.30 (p. 110) resulted in a_D ranging from 25 nm/min to 42 nm/min which are values close to the measured ones. For the average a_D of 35 nm/min, approximately 12 monolayers of ZrO_2 are formed within one 6 s lasting control cycle.

The actual stoichiometry of the film that is formed on the collecting areas is modeled by the θ_c parameter as presented in Fig. 5.30 (p. 110). Here, it must be noted that the adsorption of the oxygen on the poisoned areas is not taken into account. Therefore, θ_c is always underestimated causing the modeled value of average flow rate of O_2, $\langle Q \rangle$, to be lower than the measured one. Due to a high affinity of oxygen to Zr, see the respective sticking coefficients (Table 5.5 [p. 108]), the modeled value of the partial pressure of O_2 remains in the range of 10^{-2} Pa which is consistent with the fact that no significant changes in the value of the total system pressure were detected by the capacitive gauge used, see Fig. 5.30 (p. 110) and Sec. 5.2.2 (p. 95).

In Fig. 5.31 (p. 112), the results of steady-state and dynamical models of the controlled reactive depositions are compared. It should be remembered, see Sec. 4.6.1 (p. 55), that in the steady-state model, the value of discharge current, $\bar{I}_d$, was fixed to serve as a parameter instead of being dependent on the actual target poisoning. Using the steady-state model, the attainable values of O_2 partial pressure and target erosion rate, both as functions of the O_2 flow rate, were calculated and presented as hatched areas in Fig. 5.31(a) (p. 112). The limiting values of $\bar{I}_d$ were set to 5 A and 10 A for these are close to the minima and maxima of $\bar{I}_d$ attained during the controlled deposition process, see Fig. 5.17(a) (p. 93) and Fig. 5.30 (p. 110). Typical 'S-curves' are obtained, showing (i) a slow increase of the O_2 partial pressure and a slow

decrease of the target erosion as the O_2 flow into the system is increased, (ii) a gradual transition from the metallic to the poisoned target state starting at a certain level of the O_2 flow rate (depending on the magnitude of $\bar{I}_d$) imposing the need of reduction of the O_2 flow rate in order to achieve the desired value of the O_2 partial pressure. In practice, the deposition conditions corresponding to the negatively slopped part of the 'S-curve' are not achievable unless a fast feedback control system is employed.

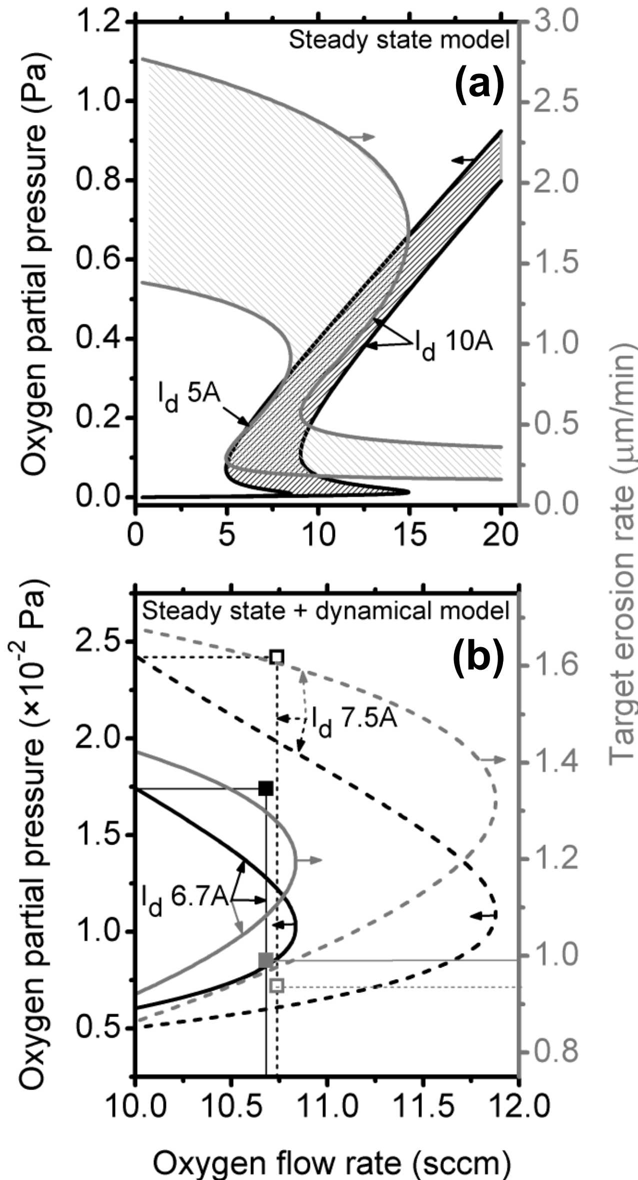

Fig. 5.31
(a) Outputs of the mathematical model of the reactive deposition process in the steady state. The discharge current, $\bar{I}_d$, was fixed to allow for a comparison of the steady-state model and the dynamical model of the controlled deposition. The values of $\bar{I}_d$ = 5 A and 10 A were chosen (see fluctuations of $\bar{I}_d$ in Fig. 5.30 [p. 110]) to mark the attainable values of the oxygen partial pressure (grey hatched area) and target erosion rate (black hatched area) as functions of the oxygen flow rate.
(b) Comparison of the outputs of the steady-state model (lines) and time-averaged outputs of the dynamical model of the controlled deposition process (squares). In the latter case, the mean values of the modeled discharge current, $\langle \bar{I}_d \rangle$, and the oxygen flow rate, $\langle Q \rangle$, were 6.7 A, 10.68 sccm for the 'more-metallic' regime (full squares) and 7.5 A, 10.74 sccm for the 'less-metallic' regime (empty squares). The outputs of the steady-state model for the corresponding values of $\bar{I}_d$ are given. In the case of the model of a dynamically controlled deposition, oxygen partial pressures are higher and the target erosion rates are lower than in the case of the corresponding steady-state model solutions.
The parameters of the model were set as stated in Table 5.5 (p. 108).

The mean values of the modeled discharge current, $\langle \bar{I}_d \rangle$, and the O_2 flow rate, $\langle Q \rangle$, were 6.7 A, 10.68 sccm for a 'more-metallic' and 7.5 A, 10.74 sccm for a 'less-metallic' regime respectively, which are values close to the measured ones, 6.8 A, 10.95 sccm and 7.2 A, 11.32 sccm respectively. These

results of the dynamical model of controlled depositions are delineated in Fig. 5.31(b) (p. 112). There, pertinent section of Fig. 5.31(a) (p. 112) is magnified to allow for the comparison of steady-state model solutions and time-averaged values of the dynamical model.

From a practitioner's perspective it is of key interest to fabricate films of defined stoichiometries at reasonable deposition rates. Thus, in the case of ZrO_x depositions, the target erosion rate and substrate coverage should both be maximized. However, as shown in Fig. 5.32 (p. 113), these properties are strongly intertwined imposing the limits on the a_D of the film of desired chemical composition. The results of the steady-state model are presented in the same manner as in Fig. 5.31 (p. 112). So, $\bar{I}_d$ was set as a parameter to visualize the area of attainable combinations of the target erosion rate and θ_c. Values of $\bar{I}_d$ bounding the hatched areas were set to 5 A and 10 A. Then, steady-state solutions for the $\bar{I}_d$ values corresponding to 'more-metallic' and 'less-metallic' processes are shown together with time-averaged values of the corresponding properties. Note that the time-averaged values are evaluated making use of results of the dynamical model that are presented in Fig. 5.30(b) (p. 110).

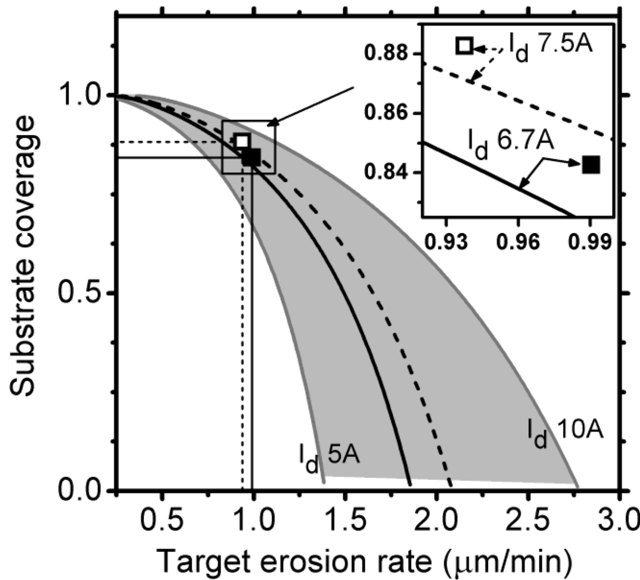

Fig. 5.32
Comparison of the outputs of the steady-state model (lines) and time-averaged outputs of the dynamical model of the controlled deposition process (squares). Regarding the steady-state model, the values of $\bar{I}_d$ = 5 A and 10 A were chosen (see fluctuations of $\bar{I}_d$ in Fig. 5.30 [p. 110]) to mark the attainable values of substrate coverage), θ_c, as defined in Sec. 4.6.1 (p. 55) (grey shaded area, film stoichiometry indicator) as functions of the target erosion rate (deposition rate indicator). In the case of dynamical model, the mean values of modeled discharge current were $\langle \bar{I}_d \rangle$ = 6.7 A and 7.5 A, the first value corresponding to the 'more-metallic' regime and the latter one to 'less-metallic' regime. The outputs of the steady-state model for the corresponding values of $\bar{I}_d$ are given. In the case of a dynamically controlled deposition, the substrate coverage is higher at the same value of the target erosion rate when compared to the steady-state solutions.
The parameters of the model were set as stated in Table 5.5 (p. 108).

It was clearly demonstrated that performing the deposition utilizing the proposed control method allowed to attain time-averaged values of the O_2 partial pressure, the target erosion rate and the substrate coverage that are close to the steady-state ones. Summing up the obtained results, it can be stated that the applied deposition control system that utilized the discharge impedance as an input parameter and operated the reactive-gas inlet valves (i) makes it possible to avoid the use of costly feedback control systems commonly used to stabilize the system at a particular point of the 'S-curve' and (ii) can be used to effectively control the reactive depositions of zirconium-oxide films.

6 Conclusions

This thesis focused on the diagnostics, control and modeling of high-power impulse magnetron sputtering (HiPIMS) discharge plasmas. In contrast to conventional pulsed direct current (pulsed DC) magnetron sputtering HiPIMS systems operate the magnetron targets with voltage pulses which (i) generate high target power densities in a pulse (on the order of $kWcm^{-2}$), (ii) are of low duty cycles (up to about 10%) and (iii) are applied at relatively low frequencies (50 Hz – 10kHz). In this work the HiPIMS technique was used to prepare zirconium and zirconium-oxide films. From the variety of diagnostic methods, energy-resolved mass spectroscopy was chosen as a principal technique because of its capability to directly inspect the fluxes of individual ions striking the substrate. For a deeper understanding of the non-reactive and reactive deposition processes, volume-averaged mathematical models were employed. The particular aims of the thesis were fulfilled as follows:

Mass spectroscopy

All the mass spectroscopy measurements were performed using a Hiden Analytical EQP 300 apparatus. The spectrometer functioning was described in detail (Sec. 4.1.1 [p. 21], 4.1.2 [p. 25] and 4.1.3 [p. 27]). To attain consistency of a large amount of mass spectrometry measurements, the methodology of spectrometer tuning (Sec. 4.1.4 [p. 31]), spectra acquisition (Sec. 4.1.5 [p. 35]) and interpretation (Sec. 4.1.6 [p. 40]) was developed and is presented herein.

The trajectories of multiply charged ions through the spectrometer were investigated in detail and corresponding corrections of the measured signal were performed (Sec. 4.1.2 [p. 25] and 4.1.6 [p. 40]). It was demonstrated that the energies of the higher charge-state ions, as measured by the spectrometer, must be multiplied by the corresponding charge state numbers in order to get the true kinetic energy of the ions striking the spectrometer. Finally, the procedure of spectra calibration which employs the measurements of electric current drawn from a plasma at the location of interest is presented (Sec. 4.2 [p. 42]).

HiPIMS depositions of zirconium films

In this work, the HiPIMS system comprising of an unbalanced circular magnetron equipped with a zirconium target driven by a unipolar pulsed DC power supply was investigated. The power supply provided rectangular voltage pulses and was operated at a frequency of 500 Hz (Sec. 4.3.1 [p. 46]) and duty cycles ranging from 4% to 10%. The average target power density in a pulse reached values of up to 2.22 $kWcm^{-2}$.

We explored the effect of increased target power densities applied during shortened voltage pulses on the (i) discharge characteristics (Sec. 5.1.1 [p. 68]), (ii) deposition characteristics (Sec. 5.1.3 [p. 84]) – the deposition rate of films, the deposition rate per average target power density in a period (i.e. the deposition rate divided by DC power equivalent), the ionized fraction of the sputtered target-material atoms in the flux of sputtered particles onto the substrate – and (iii) the ionic flux onto the substrate (Sec. 5.1.2 [p. 74]). The increased target power densities during the shortened voltage pulses resulted in a

reduced deposition rate of films from 590 nm/min to 440 nm/min and in a weakly decreasing ionized fraction (from 55% to 49%) of the sputtered zirconium atoms in the flux onto the substrate.

Particular attention was paid to the time-averaged mass spectroscopy performed at the substrate location. The spectrometer was placed at the target-to-substrate axis in a position directly facing the target surface. The ion energy distributions and compositions of total ion fluxes onto the substrate during HiPIMS of a zirconium target in the argon gas were investigated. The ionic flux was measured at several distances from the target (70 mm, 100 mm and 200 mm) and the temporal evolution of the ionic flux throughout the pulse was also investigated (Sec. 5.1.2 [p. 74]). The increase in the average target power density from 0.97 $kWcm^{-2}$ to 2.22 $kWcm^{-2}$ in shortened voltage pulses (from 200 µs to 80 µs) at an average target power density of 100 Wcm^{-2} in a period led to high fractions (21% – 32%) of doubly charged zirconium ions in total ion fluxes onto the substrate located 100 mm from the target. However, the respective fractions of singly charged zirconium ions decreased from 23% to 3%. It was observed that ion energy distributions were extended to high energies (up to 100 eV relative to the ground potential) under these conditions. The doubly charged zirconium ions became strongly predominant (up to 63%) in the total ion flux onto the substrate at the distance of 200 mm from the target. The results obtained could be used to optimize the operation parameters of the HiPIMS power supply in order to attain desired plasma properties and/or deposition efficiency.

As the discharge characteristics and the ion fluxes at the substrate position were evaluated, model calculations were carried out to explain the processes of target sputtering, sputtered target-material ionization and transport of target-material species to the substrate (Sec. 4.5 [p. 52] and 5.1.4 [p. 85]). In addition to that, the HiPIMS of titanium and copper targets which were performed employing different sputtering systems were explored in the same way. Similarly to the case of HiPIMS of zirconium target, the increase in the losses of sputtered particles as the average target power density in a pulse was increased was observed. This feature was attributed to the HiPIMS mode of the discharge since it was found to be independent of the configuration of the deposition system.

Reactive HiPIMS depositions of zirconium-oxide films

For the reactive depositions of zirconium-oxide films the identical magnetron system was further equipped with (i) reactive-gas inlet piping, (ii) ring-shaped anode located at the position of the substrate holder and (iii) computer-based control system. The depositions were performed in argon-oxygen gas mixtures at the argon pressure of 2 Pa. The repetition frequency was 500 Hz at duty cycles ranging from 2.5% to 10%. The controller utilized the discharge impedance as an input parameter and it operated the reactive-gas inlet valves. In addition to that, the reactive-gas inlet system was designed to govern target poisoning and to promote the compound formation on the substrate (Sec. 4.3.3 [p. 51] and 5.2.1 [p. 93]).

The substrate temperatures were less than 300°C during the depositions of films on a floating substrate at the distance of 100 mm from the target. The increase in the average target power density from 5 Wcm^{-2} to 100 Wcm^{-2} in a period at the same duty cycle of 10% resulted in a rapid rise in the deposition rate from 11 nm/min to 73 nm/min. However, the deposition rate per average target power density in a period decreased 3 times. The increased target power density in shortened voltage pulses (the duty cycle from 5%

to 2.5%) at an average target power density of 50 Wcm^{-2} in a period led to a reduced deposition rate from 64 nm/min to 15 nm/min. The zirconium dioxide films were found to be crystalline with a predominant monoclinic structure. Their extinction coefficient was between 6×10^{-4} and 4×10^{-3} (at 550 nm) and hardness between 10 GPa and 15 GPa (Sec. 5.3.2[p. 103] and 5.3.3 [p. 105]).

Time evolutions of the discharge current and voltage exhibited the same behavior as in the case of non-reactive sputtering of zirconium target exhibiting rapid rise (50 µs) in the discharge current to its maximum value followed by the gradual decrease (Sec. 5.2.2 [p. 95]). The employed control system induced the oscillations of the discharge power which were on the order of seconds. Correspondingly, for the case of the average target power density of 50 Wcm^{-2}, the average target power density in a pulse varied by -30% and +50% for 200 µs pulses and by -18% and +14% for 50 µs pulses with respect to its time-averaged value.

Time-averaged mass spectroscopy was carried out at the substrate position of 100 mm from the target (Sec. 5.2.3 [p. 97]). It was shown that in the case of depositions of transparent zirconium-oxide films (extinction coeffiecient lower than 4×10^{-3} at 550 nm) the ion flux at the substrate position was (i) dominated by the Ar^{+} and Ar^{2+} ions, (ii) oxygen ions prevailed over zirconium ions and (iii) flux O^{+} ions was at least 5 times higher than the flux of O^{2+} ions indicating high degree of dissociation of O_2 molecules.

A time-resolved model of the reactive sputtering process comprising a model of the magnetron sputtering apparatus and a model of the control system was implemented and used to investigate the performance of the employed control system (Sec. 4.6 [p. 55] and 5.4 [p. 107]). It was shown that the control system that utilizes the discharge impedance as the input parameter and operates the reactive-gas inlet valves can provide a feasible mean of control of the reactive depositions of zirconium-oxide films.

7 References

[1] Musil J, *Recent advances in magnetron sputtering technology*, Surface & Coatings Technology **100-101**, 280-286 (1998).

[2] Arnell R D, Kelly P J, *Recent advances in magnetron sputtering*, Surface & Coatings Technology **112**, 170–176 (1999).

[3] Arnell R D, Kelly P J, Bradley J W, *Recent developments in pulsed magnetron sputtering*, Surface & Coatings Technology **188–189**, 158–163 (2004).

[4] Anders A, *Discharge physics of high power impulse magnetron sputtering*, Surface & Coatings Technology **205**, S1-S9 (2011).

[5] Bogaerts A, Neyts E, Gijbels R, Mullen van der J, *Gas discharge plasmas and their applications*, Spectrochimica Acta Part B **57**, 609–658 (2002).

[6] Bräuer G, Szyszka B, Vergöhl M, Bandorf R, *Magnetron sputtering – Milestones of 30 years*, Vacuum **84**, 1354–1359 (2010).

[7] Safi I, *Recent aspects concerning DC reactive magnetron sputtering: a review*, Surface & Coatings Technology **127**, 203-219 (2000).

[8] Sproul W D, Christie D J, Carted D C, *Review: Control of reactive sputtering processes*, Thin Solid Films **491**, 1-17 (2005).

[9] Helmersson U, Lattemann M, Bohlmark J, Ehiasarian A P, Gudmundsson J T, *Ionized physical vapor deposition (IPVD): A review of technology and applications*, Thin Solid Films **513**, 1–24 (2006).

[10] Mattox D M, *The foundations of vacuum coating technology* (Noyes Publications / William Andrew Publishing, Norwich, 2003).

[11] Barna P B, Adamik M, *Fundamental structure forming phenomena of polycrystalline films and the structure zone models*, Thin Solid Films **317**, 27–33 (1998).

[12] Anders A, *A structure zone diagram including plasma-based deposition and ion etching*, Thin Solid Films **518**, 4087–4090 (2010).

[13] Mercs D, Perry F, A B, *Hot target sputtering: A new way for high-rate deposition of stoichiometric ceramic films*, Surface & Coatings Technology **201**, 2276-2281 (2006).

[14] Doerner R P, Krasheninnikov S I, Schmid K, *Particle-induced erosion of materials at elevated temperature*, Journal of Applied Physics **95** (8), 4471-4475 (2004).

[15] Fletcher J, *High-rate reactive sputter deposition of zirconium dioxide*, Journal of Vacuum Science and Technology A **6**, 3088-3097 (1988).

[16] Aijaz A, Lundin D, Larsson P, Petter Larsson , U, *Dual-magnetron open field sputtering system for sideways deposition of thin films*, Surface & Coatings Technology **204**, 2165–2169 (2010).

[17] Bohlmark J, Östbye M, Lattemann M, Ljungcrantz H, Rosell T, Helmersson U, *Guiding the deposition flux in an ionized magnetron discharge*, Thin Solid Films **515**, 1928– 1931 (2006).

[18] Poucques L d, Imbert J C, Boisse-Laporte C, Bretagne J, Ganciu M, Teulé-Gay L, Touzeau M, *Study of the transport of titanium neutrals and ions in the post-discharge of a high power pulsed magnetron sputtering device*, Plasma Sources Science and Technology **15**, 661–669 (2006).

[19] Yukimura K, Mieda R, Azuma K, Tamagaki H, Okimoto T, *Voltage–current characteristics of a high-power pulsed sputtering (HPPS) glow discharge and plasma density estimation*, Nuclear Instruments and Methods in Physics Research B **267**, 1692-1695 (2009).

[20] Bradley J W, Bäcker H, Aranda-Gonzalvo Y, Kelly P J, Arnell R, *The distribution of ion energies at the substrate in an asymmetric bi-polar pulsed DC magnetron discharge*, Plasma Sources Science and Technology **11**, 165-174 (2002).

[21] Mráz S, Schneider J M, *Influence of the negative oxygen ions on the structure evolution of transition metal oxide thin films*, Journal of Applied Physics **100**, 023503 (2006).

[22] Martin N, Santo A M E, Sanjinés R, Lévy F, *Energy distribution of ions bombarding TiO2 thin films during sputter deposition*, Surface and Coatings Technology **138**, 77-83 (2001).

[23] Rossnagel S M, Hopwood J, *Magnetron sputter deposition with high levels of metal ionization*, Applied Physics Letters **63**, 3285-3287 (1993).

[24] Kudláček P, Vlček J, Houška J, Han J G, Jung M J, Kim Y M, *Ion-bombardment characteristics during deposition of TiN films using a grid-assisted magnetron with enhanced plasma potential*, Vacuum **81**, 1109-1113 (2007).

[25] Alami J, Eklund P, Andersson J M, Lattemann M, Wallin E, Bohlmark J, Persson P, Helmersson U, *Phase tailoring of Ta thin films by highly ionized pulsed magnetron sputtering*, Thin Solid Films **515**, 3434– 3438 (2007).

[26] Boisse-Laporte C, Leroy O, de Poucques L, Agius B, Bretagne J, Hugon M C, Teulé-Gay L, Touzeau M, *New type of plasma reactor for thin film deposition: magnetron plasma process assisted by microwaves to ionise sputtered vapour*, Surface & Coatings Technology **179**, 176-181 (2004).

[27] Vergöhl M, Werner O, Bruns S, Wallendorf T, Mark G, *Superimposed MF-HiPIMS Processes for the Deposition of ZrO2 Thin Films*, 51st Annual Technical Conference Proceedings, Chicago, IL, 2008.

[28] Vergöhl M, Bruns S, Werner O, *Process Control and Thin Film Properties of Al2O3 Layers Deposited by High Power Impulse Magnetron Sputtering*, Proceedings of the 51st Annual Society of Vacuum Coaters (SVC) Technical Conference, Santa Clara, California, 2009.

[29] Kouznetsov V, Macák K, Schneider J M, Helmersson U, Petrov I, *A novel pulsed magnetron sputter technique utilizing very high target power densities*, Surface & Coatings Technology **122**, 290–293 (1999).

[30] Macák K, Kouznetsov V, Schneider J, Helmersson U, Petrov I, *Ionized sputter deposition using an extremely high plasma density pulsed magnetron discharge*, Journal of Vacuum Sience and Technology A **18** (4), 1533-1537 (2000).

[31] Ehiasarian A P, Hovsepian P E, Hultman L, Helmersson U, Thin Solid Films **457** (270) (2004).

[32] Konstantinidis S, Dauchot J P, Ganciu M, Ricard A, Hecq M, *Influence of pulse duration on the plasma characteristics in high-power pulsed magnetron discharges*, Journal of Applied Physics **99**, 013307 (2006).

[33] Vlček J, Kudláček P, Burcalová K, Musil J, *High -power pulsed sputtering using a magnetron with enhanced plasma confinement*, Journal of Vacuum Science and Technology A **25** (1), 42-47 (2007).

[34] Vašina P, Meško M, Imbert J C, Ganciu M, Boisse-Laporte C, de Poucques L, Touzeau M, Pagnon D, Bretagne J, *Experimental study of a pre-ionized high power impulsed magnetron discharge*, Plasma Sources Science and Technology **16**, 501-510 (2007).

[35] Anders A, Andersson J, Ehiasarian A, *High power impulse magnetron sputtering: Current-voltage-time characteristics indicate the onset of sustained self-sputtering*, Journal of Applied Physics **102**, 113303 (2007).

[36] Anders A, Andersson J, Ehiasarian A, *Erratum: "High power impulse magnetron sputtering: Current-voltage-time characteristics indicate the onset of sustained self-sputtering" [J. Appl. Phys. 102, 113303, 2007]* **103**, 039901 (2008).

[37] Andersson J, Anders A, *Self-Sputtering Far above the Runaway Threshold: An Extraordinary Metal-Ion Generator*, Physical Review Letters **102**, 045003 (2009).

[38] Sittinger V, Ruske F, Werner W, Jacobs C, Szyszka B, Christie D J, *High power pulsed magnetron sputtering of transparent conducting oxides*, Thin Solid Films **516**, 5847– 5859 (2008).

[39] Sarakinos K, Alami J, Dukwen J, Woerdenweber J, Wuttig M, *A semi-quantitative model for the deposition rate in non-reactive high power pulsed magnetron sputtering*, Journal of Physics D: Applied Physics **41** (21), 215301.

[40] Ehiasarian A P, New R, Münz W D, Hultman L, Helmersson U, Kouznetsov V, *Influence of high power densities on the composition of pulsed magnetron plasmas*, Vacuum **65**, 147–154 (2002).

[41] Horwat D, Anders A, *Spatial distribution of average charge state and deposition rate in high power impulse magnetron sputtering of copper*, Journal of Physics D: Applied Physics **41** (13), 135210 (2008).

[42] Sarakinos K, Alami J, Konstantinidis S, *High power pulsed magnetron sputtering: A review on scienti fi c and engineering state of the art*, Surface & Coatings Technology **204**, 1661–1684 (2010).

[43] Alami J, Bolz S, Sarakinos K, *High power pulsed magnetron sputtering: Fundamentals and applications*, Journal of Alloys and Compounds **483** (1-2), 530–534 (2009).

[44] Anders A, *Deposition Rates of High Power Impulse Magnetron Sputtering*, Annual Technical Meeting, Society of Vacuum Coaters (SVC), Chicago, Illinois, 2008.

[45] Anders A, *High power impulse magnetron sputtering and related discharges: Scalable plasma sources for plasma-based ion implantation and deposition*, Surface & Coatings Technology **204**, 2864–2868 (2010).

[46] Emmerlich J, Mráz S, Snyders R, Jiang K, Schneider J M, *The physical reason for the apparently low deposition rate during high-power pulsed magnetron sputtering*, Vacuum **82**, 867–870 (2008).

[47] Samuelsson M, Lundin D, Jensen J, Raadu M A, Gudmundsson J T, Helmersson U, *On the film density using high power impulse magnetron sputtering*, Surface & Coatings Technology **205**, 591-596 (2010).

[48] Brenning N, Axnäs I, Raadu M A, Lundin D, Helmerson U, *A bulk plasma model for dc and HiPIMS magnetrons*, Plasma Sources Science and Technology **17**, 045009 (2008).

[49] Lin J, Moore J J, Sproul W D, Mishra B, Rees J A, Wu Z, Chistyakov R, Abraham B, *Ion energy and mass distributions of the plasma during modulated pulse power magnetron sputtering*, Surface & Coatings Technology **203**, 3676–3685 (2009).

[50] Mark G, US Patent Patent No. 6.735.099 (2004).

[51] Yukimura K, Ehiasarian A P, *Generation of RF plasma assisted high power pulsed sputtering glow discharge without using a magnetic field*, Nuclear Instruments and Methods in Physics Research B **267**, 1701-1704 (2009).

[52] Liebig B, Braithwaite N S J, Kelly P J, Chistyakov R, Abraham B, Bradley J W, *Time-resolved plasma characterisation of modulated pulsed power magnetron sputtering of chromium*, Surface & Coatings Technology **205**, S312-S316 (2011).

[53] Lin J, Moore J J, Sproul W D, Mishra B, Wu Z, *Modulated pulse power sputtered chromium coatings*, Thin Solid Films **518**, 1566-1570 (2009).

[54] Hala M, Viau N, Zabeida O, Klemberg-Sapieha J E, Martinu L, *Dynamics of reactive high-power impulse magnetron sputtering discharge studied by time- and space-resolved optical emission spectroscopy and fast imaging*, Journal of Applied Physics **107**, 043305 (2010).

[55] Liebig B, Braithwaite N S J, Kelly P J, Bradley J W, *Spatial and temporal investigation of high power pulsed magnetron discharges by optical 2D-imaging*, Thin Solid Films **519**, 1699-1704 (2010).

[56] Vetuschka A, Ehiasarian A P, *Plasma dynamics in chromium and titanium HiPIMS discharges*, Journal of Physics D: Applied Physics **41**, 015204 (2008).

[57] Gudmundsson J T, Alami J, Helmersson U, *Evolution of the electron energy distribution and plasma parameteres in a pulsed matnetron discharge*, Applied Physics Letters **78** (2001).

[58] Gudmundsson J T, Sigurjonsson P, Larsson P, Lundin D, Helmersson U, *On the electron energy in the high power impulse magnetron sputtering discharge*, Journal of Appied Physiscs **105**, 123302 (2009).

[59] Pajdarova A, Vlček J, Kudláček P, Lukáš J, *Electron energy distributions and plasma parameters in high-power pulsed magnetron sputtering discharges*, Plasma Sources Science and Technology **18**, 025008 (2009).

[60] Hecimovic A, Burcalova K, Ehiasarian A P, *Origins of ion energy distribution function (IEDF) in high power impulse magnetron sputtering (HIPIMS) plasma discharge*, Journal of Physics D: Applied Physics **41**, 095203 (2008).

[61] Hecimovic A, Ehiasarian A P, *Time evolution of ion energies in HIPIMS of chromium plasma discharge*, Journal of Physics D: Applied Physics **42**, 135209 (2009).

[62] Lundin D, Larsson P, Wallin E, Lattemann M, Brenning N, Helmersson U, *Cross-field ion transport during high power impulse magnetron sputtering*, Plasma Sources Science and Technology **17**, 035021 (2008).

[63] Bohlmark J, Lattemann M, Gudmundsson J T, Ehiasarian A P, Gonzalvo A Y, Brenning N, Helmersson U, *The ion energy distributions and ion flux composition from a high power impulse magnetron sputtering discharge*, Thin Solid Films **515**, 1522-1526 (2006).

[64] Oks E, *Evolution of the plasma composition of a high power impulse magnetron sputtering system studied with a time-of-flight spectrometer*, Journal of Applied Physics **105**, 093304 (2009).

[65] Anders A, Yushkov G Y, *Plasma "anti-assistance" and "self-assistance" to high power impulse magnetron sputtering*, Journal of Applied Physics **105**, 073301 (2009).

[66] Vozniy V O, Duday D, Lejars A, Wirtz T, *Ion density increase in high power twin-cathode magnetron system*, Vacuum **86**, 78-81 (2011).

[67] Vašina P, Meško M, Poucques L d, Bretagne J, Boisse-Laporte C, Touzeau M, *Study of a fast high power pulsed magnetron discharge: role of plasma deconfinement on the charged particle transport*, Plasma Sources Science and Technology **17**, 035007 (2008).

[68] Bäcker H, Bradley J W, *Observations of the long-term plasma evolution in a pulsed dc magnetron discharge*, Plasma Sources Science and Technology **14**, 419-431 (2005).

[69] Gudmundsson J T, Alami J, Helmersson U, *Spatial and temporal behavior of the plasma parameters in a pulsed magnetron discharge*, Surface & Coatings Technology **161**, 249-256 (2002).

[70] Bradley J W, Thompson S, Gonzalvo Y A, *Measurement of the plasma potential in a magnetron discharge and the prediciton of the electron drift speeds*, Plasma Sources Science and Technology **10**, 490-501 (2001).

[71] Bradley J W, Karkari S, Vetuschka A, *A study of the transient plasma potential in a pulsed bi-polar dc magnetron discharge*, Plasma Sources Science and Tehcnology **13**, 189-198 (2004).

[72] Sarakinos K, Alami J, Klever C, Wuttig M, *Process stabilization and enhancement of deposition rate during reactive high power pulsed magnetron sputtering of zirconium oxide*, Surface and Coatings Technology **202**, 5033-5035 (2008).

[73] Lundin D, Helmersson U, Kirkpatrick S, Rohde S, Brenning N, *Anomalous electron transport in high power impulse magnetron sputtering*, Plasma Sources Science and Technology **17**, 025007 (2008).

[74] Gylfason K B, Alami J, Helmersson U, Gudmundsson J T, *Ion-acoustic solitary waves in a high power pulsed magnetron sputtering discharge*, Journal of Physics D: Applied Physics **38**, 3417-3421 (2005).

[75] Alami J, Gudmundsson J T, Bohlmark J, Birch J, Helmersson U, *Plasma dynamics in a highly ionized pulsed magnetron discharge*, Plasma Sources Science and Technology **14**, 525-531 (2005).

[76] Bohlmark J H U, VanZeeland M, Axnäss I, Alami J, Brenning N, *Measurement of the magnetic field change in a pulsed high current magnetron discharge*, Plasma Sources Science and Technology **13**, 654-661 (2004).

[77] Wallin E, U H, *Hysteresis-free reactive high power impulse magnetron sputtering*, Thin Solid Films **516**, 6398– 6401 (2008).

[78] Martin N, Bally A R, Hones P, Sanjines R, Levy F, *High rate and process control of reactive sputtering by gas pulsing: the Ti-O system*, Thin Solid Films **377-378**, 550-556 (2000).

[79] Bruns S, Vergöhl M, Werner O, Wallendorf T, *High rate deposition of mixed oxides by controlled reactive magnetron-sputtering from metallic targets*, Thin Solid Films (2011).

[80] Ellmer K, Mientus R, *Reactive DC Magnetron Sputtering of Elemental Targets in Ar/O2 Mixtures: Relation Between the Discharge Characteristics and the Heat of Formation of the Corresponding Oxides*, Dresden, Germany, 1994.

[81] Depla D, De Gryse R, *Influence of oxygen addition on the target voltage during reactive sputtering of aluminium*, Plasma Sources Science and Technology **10**, 547-555 (2001).

[82] Depla D, De Gryse R, *Target poisoning during reactive magnetron sputtering: Part II: the influence of chemisorption and gettering*, Surface & Coatings Technology **183**, 190-195 (2004).

[83] Depla D, De Gryse R, *Target poisoning during reactive magnetron sputtering: Part III: the prediction of the critical reactive gas mole fraction*, Surface & Coatings Technology **183**, 196-203 (2004).

[84] Depla D, De Gryse R, *Target poisoning during reactive magnetron sputtering: Part I: the influence of ion implantation*, Surface & Coatings Technology **183**, 190-195 (2004).

[85] Depla D, Buyle G, Haemers J, De Gryse R, *Discharge voltage measurements during magnetron sputtering*, Surface & Coatings Technology **200**, 4329-4338 (2006).

[86] Depla D, Chen Z Y, Bogaerts A, Ignatova V, De Gryse R, Gijbels R, *Modeling of the target surface modification by reactive ion implantation during magnetron sputtering*, Journal of Vacuum Science and Technology A **22** (4), 1524-1529 (2004).

[87] Depla D, Haemers J, De Gryse R, *Target surface condition during reactive glow discharge sputtering of copper*, Plasma Sources Science and Technology **11**, 91-96 (2002).

[88] Audronis M, Bellido-Gonzales V, *Hysteresis behaviour of reactive high power impulse magnetron sputtering*, Thin Solid Films **518**, 1962-1965 (2010).

[89] Audronis M, Bellido-Gonzales V, *The effect of Ti sputter target oxidation level on reactive High Power Impulse Magnetron Sputtering process behaviour*, Surface & Coatings Technology **205**, 5322-5325 (2011).

[90] Audronis M, Bellido-Gonzales V, *Investigation of reactive high power impulse magnetron sputtering processes using various target material–reactive gas combinations*, Surface & Coatings Technology **205**, 3613-3620 (2011).

[91] Berg S, Nyberg T, *Review: Fundamental understanding and modeling of reactive sputtering process*, Thin Solid Films **476**, 215-230 (2005).

[92] Aiempanakit M, Kubart T, Larsson P, Sarakinos K, Jensen J, Helmersson U, *Hysteresis and process stability in reactive high power impulse magnetron sputtering of metal oxides*, Thin Solid Films **519** (22), 7779-7784 (2011).

[93] Audronis M, Bellido-Gonzales V, Daniel B, *Control of reactive high power impulse magnetron sputtering processes*, Surface & Coatings Technology **204**, 2159-2164 (2010).

[94] Bogaerts A, Gijbels R, *Numerical modelling of gas discharge plasmas for various applications*, Vacuum **69**, 37-52 (2003).

[95] Verbouncoeur J P, *Particle simulation of plasmas: review and advances*, Plasma Physics and Controlled Fusion **47**, A231-A260 (2006).

[96] Bird G A, *Molecular Gas Dynamics and the Direct Simulation of Gas Flows* (Clerendon Press, Oxford, 1994).

[97] Kim H C, Iza F, Yang S S, Radmilović-Radjenović, Lee J K, *Topical Review: Particle and fluid simulations of low-temperature plasmadischarges: benchmarks and kinetic effects*, Journal of Physics D: Applied Physics **38**, R283-R301 (2005).

[98] Hamaguchi S, *Modeling and simulation methods for plasma processing*, IBM Journal of Research and Development **43** (1/2), 199-215 (1999).

[99] Sungjin K, Lieberman M A, Lichtengerg J A, *Improved volume-averaged model for steady and pulsed-power electronegative discharges*, Journal of Vacuum Science and Technology A **24** (6), 2025-2014 (2006).

[100] Allen J E, *The plasma-sheath boundary: its history and Langmuir's definition of the sheath edge*, Plasma Sources Science and Technology **18**, 014004 (2009).

[101] Lieberman M A, Lichtenberg A J, *Principles of plasma discharges and materials processing*, 2nd ed. (Wiley-Interscience, New York, 2005).

[102] Gudmundsson J T, *Ionization mechanism in the high power impulse magnetron sputtering (HiPIMS) discharge*, Journal of Physics: Conference Series **100**, 082013 (2008).

[103] Vlček J B K, *A phenomenological equilibrium model applicable to high-power pulsed magnetron sputtering*, Plasma Sources Science and Technology **19**, 065010 (2010).

[104] Kubart T, Kappertz O, Nyberg Y B S, *Dynamic behaviour of the reactive sputtering process*, Thin Solid Films **515**, 421-424 (2006).

[105] Kusano E, *Modeling of time-dependent process changes and hysteresis inin Ti-O2 reactive sputtering*, Journal of Applied Physics **73** (12), 8565-8574 (1993).

[106] *EQP/EQS Analyser Operator's Manual, Issue: F Rev. 1, Document Number: HA-085-003* (Hiden Analytical Ltd.).

[107] *EQP and EQS Analysers, Application Note* (Hiden Analytical Ltd.).

[108] Hamers E A G, van Sark. W G J H M, Bezemer J, Goedheerr W J, van der Weg W F, *On the transmission function of an ion-energy and mass spectrometer*, International Journal of Mass Spectrometry and Ion Processes **173**, 91-98 (1998).

[109] Urgošík B, *Elektronova a iontova optika* (Charles University in Praque, Faculty of Mathematics and Physics, Praque, 1982).

[110] Rees J A, Hiden Analytical Ltd. (Personal communication, Plzen, 2007).

[111] Kudláček P, Vlček J, Buraclová K, Lukáš J, *Highly ionized fluxes of sputtered titanium atoms in high-power pulsed magnetron discharges*, Plasma Sources Science and Technology **17** (2008).

[112] Phelps A V, Petrovic Z L, *Review: Cold-cathode discharges and breakdown in argon: surface and gas phase production of secondary electrons*, Plasma Sources Science and Technology **8** (3), R21 (1999).

[113] Donkó Z, *Apparent secondary-electron emission coefficient and the voltage-current characteristics of argon glow discharges*, Physical Review E **64** (2), 026401 (2001).

[114] Buyle G, De Bosscher W, Depla D, Eufinger K, Haemers J, De Gryse R, *Recapture of secondary electrons by the target in a DC planar magnetron discharge*, Vacuum **70**, 29-35 (2003).

[115] Abrams C A, Graves D B, *Cu sputtering and deposition by off-normal, near-threshold Cu+ bombardment: Molecular dynamics simulations*, Journal of Applied Physics **86** (4), 2263 (1999).

[116] Kress J D, Hanson D E, Volter A F, Liu C L, Liu X Y, Coronell D G, *Molecular dynamics simulation of Cu and Ar ion sputtering of Cu (111) surfaces*, Journal of Vacuum Science & Technology A **17** (5), 2819 (1999).

[117] Kersch A, Hansen U, *Atomistic feature scale modeling of the titanium ionized physical vapor deposition process*, Journal of Vacuum Science & Technology A **20** (4), 1284 (2002).

[118] Ziegler J F, Ziegler M D, Biersack J, *SRIM2006.02*, http://srim.org (2006).

[119] Kusano E, *An approach to estimate gettering effects in Ti-O2 reactive sputtering processes*, Journal of Vacuum Science and Technology A **10** (4), 1696-1700 (1992).

[120] Kusano E, *An investigation of hysteresis effect as a function of pumping speed, sputterign current and O2/Ar rati, in Ti-O2 reactive sputtering processes*, Journal of Applied Physics **70** (11), 7089-7096 (1991).

[121] Rossnagel S M, *Gas density reduction effect in magnetrons*, Journal of Vacuum Science and Technology A **6**, 19-24 (1988).

[122] Vlček J, Pajdarová A, Musil J, *Pulsed dc magnetron discharges and their utilization in plasma surface engineering*, Contribution to Plasma Physics **44** (5-6), 426-436 (2004).

[123] Vlček J, Kudláček P, Burcalová K, Musil J, *Ion flux characteristics in high-power pulsed magnetron sputtering discharges*, Europhysics Letters **77**, 45002 (2007).

[124] Huheey J E, Keiter E A, Keiter R L, *Inorganic chemistry: Principles of structure and reactivity*, 4th ed. (Harper, New York, 1993).

[125] James A M, Lord M P, *Macmillan's chemical and physical data* (Macmillan, London, 1992).

[126] Lu J, Kushner M J, *Effect of sputter heating in ionized metal physical vapor deposition reactors*, Journal of Applied Physics **87** (10), 7198 (2000).

[127] Green J M, Webb C E, *The production of excited metal ions in thermal energy charge transfer and Penning reactions*, Journal of Physics B: Atomic and Molecular Physics **7** (13), 1698 (1974).

[128] Danzmann K, Kock M, *Population densities in a titanium hollow cathode* , Journal of Physics B: Atomic and Molecular Physics **14** (16), 2989 (1981).

[129] Tamir Y, Shuker R, *Thermal energy charge transfer in the Zn-Ar system*, Journal of Applied Physics **68** (11), 5415 (1990).

[130] Vlček J, Forejt L, van der Mullen J A M, *Magnesium as a representative analyte metal in argon inductively coupled plasmas. II. Population mechanisms in analytical zones of different spectrochemical systems*, Spectrochimica Acta Part B: Atomic Spectroscopy **52** (5), 609-619 (1997).

[131] Danielson P, *A Journal of Practical and Useful Vauum Technology*, http://www.vacuumlab.com (2011).

[132] Rosen J, Anders A, Hultman L, Schneider J M, *Charge state and time resolved plasma composition of a pulsed zirconium arc in a nitrogen environment*, Journal of Applied Physics **96**, 4793-4799 (2004).

[133] Takagi Y, Skashita Y, Toyoda H, Sugai H, *Generation processes of super-high-energy atoms and ions in magnetron sputtering plasma*, Vacuum **80**, 581-587 (2006).

[134] Kubart T, Aiempanakit M, Andersson J, Nyberg T B S H U, *Studies of hysteresis effect in reactive HiPIMS deposition of oxides*, Surface & Coatings Technology **205**, S303–S306 (2011).

[135] Meeker D, *Finite element method magnetics, FEMM 4.2*, http://femm.org (2010).

[136] Kusano E, Kinbara A, *Time-dependent O2 mass balance change and target surface oxidation during mode transition in Ti-O2 reactive sputtering*, Journal of Applied Physics **87** (4), 2015-2019 (1993).

[137] Vlcek J, Rezek J, Lazar J, Houska J, Cerstvy R, *High-Rate Reactive Deposition of Transparent Zirconium Dioxide Films Using High-Power Pulsed DC Magnetron Sputtering*, Proceedings of the 54th Annual Society of Vacuum Coaters (SVC) Technical Conference, Chicago, Illinois, 2011.

8 Publications of the candidate

8.1 Refereed journal papers

[1] Lazar J, Vlček J, Rezek J, *Ion flux characteristics and efficiency of the deposition processes in high power impulse magnetron sputtering of zirconium*, Journal of Applied Physics **108**, 063307 (2010).

8.2 Conference papers and proceedings

[1] Lazar J, *Characterization of High Power Impulse Magnetron Sputtering of Zirconium*, Proceedings of the 53rd Annual Society of Vacuum Coaters (SVC) Technical Conference, pp. 183-186, Orlando, 2010.

[2] Lazar J, Rezek J, Vlcek J, *Ion flux characteristics and efficiency of the deposition processes in high power impulse magnetron*, Proceedings of Magnetron, Ion processing & Arc Technologies European Conference (MIATEC), pp. 5, Metz, France, 2010.

[3] Lazar J, Rezek J, Vlček J, *High power impulse magnetron sputtering of zirconium*, Proceedings of the 17th International Colloquium on Plasma Processes (CIP), pp. 108, Marseille, France, 2009.

[4] Vlček J, Rezek J, Lazar J, Houška J, *High-Rate Reactive Deposition of Transparent Zirconium Dioxide Films Using High-Power Pulsed DC Magnetron Sputtering*, Proceedings of the 54th Annual Society of Vacuum Coaters (SVC) Technical Conference, pp. 131-134, Chicago, Illinois , 2011.

[5] Lazar J, Rezek J, Vlček J, *Characteristics of ion flux in high power impulse magnetron sputtering of zirconium*, Proceedings of the Potential and Applications of Thin Ceramic and Metal Coatings (PATCMC), pp. 61-62, Plzeň, Czech Republic, 2010.

[6] Rezek J, Lazar J, Vlcek J, *High power impulse magnetron sputtering of zirconium*, 37th International Conference on Metallurgical Coatings and Thin Films (ICMCFT), Book of Abstracts, pp. 106, San Diego, California, 2010.

[7] Rezek J, Lazar J, Vlcek J, *Effect of the enlarged target power densities during shortened voltage pulses on high power impulse magnetron sputtering of zirconium*, 12th International Conference on Plasma Surface Engineering (PSE), Book of Abstracts, pp. 219, Garmisch-Partenkirchen, Germany, 2010.

[8] Vlček J, Lazar J, Rezek J, Calta P, Steidl P, *Two pulsed magnetron systems – characterization and application*, 12th International Conference on Plasma Surface Engineering (PSE), Book of Abstracts, pp. 27, Garmisch-Partenkirchen Germany, 2010.

[9] Rezek J, Lazar J, Vlček J, *High power impulse magnetron sputtering of zirconium*, European Materials Research Society (EMRS) Spring Meeting, Book of Abstracts, Paper No. Q7-01, Strasbourg, France, 2009.

[10] Baroch P, Lazar J, Musil J, *Plasma Drift in Dual Magnetron Discharge*, Proceedings of the 25th Symposium on Plasma Physics and Technology (SPPT), pp. 138-139, Praha, Czech Republic, 2008.

Summary

High-power impulse magnetron sputtering (HiPIMS) is an emerging physical vapor deposition technique. HiPIMS systems operate the magnetron targets with voltage pulses that (i) generate high target power densities in a pulse (on the order of $kWcm^{-2}$), (ii) are of low duty cycles (up to about 10%) and (iii) are applied at relatively low frequencies (50 Hz – 10kHz).

This thesis is focused on the diagnostics, control and modeling of HiPIMS discharge plasmas. The ion fluxes were investigated by time-averaged energy-resolved mass spectroscopy. The methodology of the (i) measurement, (ii) calibration and (iii) interpretation of the energy spectra of singly and multiply charged ions is presented. The HiPIMS depositions of zirconium and zirconium-oxide films were performed using an unbalanced magnetron with a planar zirconium target with a diameter of 100 mm. Substrate was located at a distance of 100 mm from the target and the pulse repetition frequency was 500 Hz.

Zirconium films were deposited at an argon pressure of 1 Pa. Energy-resolved mass spectroscopy was carried out at positions 70 mm, 100 mm and 200 mm from the target. An increase in the average target power density from 0.97 $kWcm^{-2}$ to 2.22 $kWcm^{-2}$ in shortened voltage pulses (from 10% to 4% duty cycle) at an average target power density of 100 Wcm^{-2} in a period resulted in (i) high fractions (21% – 32%) of doubly charged zirconium ions in total ion fluxes onto the substrate, (ii) decreasing fractions of singly charged zirconium ions from 23% to 3%, (iii) a reduced deposition rate of films from 590 nm/min to 440 nm/min and (iv) a weakly decreasing ionized fraction (from 55% to 49%) of the sputtered zirconium atoms in the flux onto the substrate and (v) slight decrease in the flux of ions with high (up to 100 eV) kinetic energies. The doubly charged zirconium ions became strongly predominant (up to 63%) in the total ion flux onto the substrate at a distance of 200 mm from the target. Model calculations indicate that the increase in the losses of sputtered particles as the average target power density in a pulse is increased is inherent to the HiPIMS mode of the discharge and is independent of the particular configuration of the deposition system.

For the reactive depositions of zirconium-oxide films, the sputtering device was further equipped with (i) a reactive-gas inlet system, (ii) a ring-shaped anode located at the position of the substrate holder and (iii) a computer-based control system. The depositions were performed in argon-oxygen gas mixtures at an argon pressure of 2 Pa. Duty cycles ranged from 2.5% to 10%. Transparent (extinction coefficient lower than 4×10^{-3} at 550 nm) zirconium dioxide (ZrO_2) films were deposited. An increase in the average target power density from 5 Wcm^{-2} to 100 Wcm^{-2} in a period at the same duty cycle of 10% resulted in (i) a rise in the deposition rate from 11 nm/min to 73 nm/min and (ii) a decrease (3 times) in the deposition rate per average target power density in a period. An increased target power density in shortened voltage pulses (the duty cycle decreased from 5% to 2.5%) at an average target power density of 50 Wcm^{-2} in a period led to a reduced deposition rate from 64 nm/min to 15 nm/min. ZrO_2 films were crystalline with a predominant monoclinic structure. Their extinction coefficient was between 6×10^{-4} and 4×10^{-3} (at 550 nm) and hardness between 10 GPa and 15 GPa. The ion flux at the substrate position (i) was dominated by the Ar^+ and Ar^{2+} ions, (ii) comprised more oxygen ions than zirconium ions and (iii) the flux of O^+ ions was at least 5 times higher than the flux of O^{2+} ions. By means of a time-resolved model of the deposition process it was demonstrated that the applied control system that utilized the discharge impedance as the input parameter and operated the reactive-gas inlet valves can be used to effectively control the reactive depositions of zirconium-oxide films.

Anotace

Vysokovýkonové pulzní magnetronové naprašování (HiPIMS) přitahuje v posledních letech značnou pozornost odborné veřejnosti. Oproti konvenčním systémům používaným k pulznímu magnetronovému naprašování jsou při HiPIMS depozicích na terč magnetronu přiváděny napěťové pulsy které (i) způsobují vysoké nominální výkonové hustoty na terči (v řádech $kWcm^{-2}$), (ii) mají nízkou střídu (obvykle do 10%) a (iii) relativně nízkou opakovací frekvenci (50 Hz-10 kHz).

Tato disertační práce je zaměřena na diagnostiku, řízení a modelování výbojového plazmatu vytvářeného při HiPIMS depozičních procesech. Časově nerozlišená energiová spektra toků iontů byla zkoumána hmotnostním spektrometrem. V práci je prezentována metodologie (i) měření, (ii) kalibrace a (iii) interpretace energiově rozlišených spekter jednou a vícenásobně ionizovaných částic. K HiPIMS depozicím zirkonových vrstev a vrstev oxidů zirkonu byl použit zirkonový terč o průměru 100 mm osazený na nevyvážený magnetron. Substrát byl umístěn ve vzdálenosti 100 mm od terče, opakovací frekvence pulzů byla 500 Hz.

Zirkonové vrstvy byly deponovány v argonové atmosféře o tlaku 1 Pa. Toky iontů byly měřeny hmotnostním spektrometrem ve vzdálenostech 70 mm, 100 mm a 200 mm od terče. Při zachování průměrné výkonové hustoty (100 Wcm^{-2}) na terči vedlo zkrácení pulzů (střída snížena z 10% na 4%) ke zvýšení průměrné výkonové hustoty v pulzu z 0.97 $kWcm^{-2}$ na 2,22 $kWcm^{-2}$ a k (i) vzrůstu podílu dvojnásobně ionizovaných zirkonových iontů (z 21% až na 32%) v celkovém toku na substrát, (ii) poklesu zastoupení jednou ionizovaných zirkonových iontů (z 23% na 3%), (iii) snížení depoziční rychlosti z 590 nm/min na 440 nm/min, (iv) mírnému poklesu zastoupení iontů zirkonu v celkovém toku zirkonových částic na substrát (z 55% na 49%) a (v) mírnému poklesu toků iotů s vysokými (až 100 eV) kinetickými energiemi. Dvojnásobně ionizované zirkonové ionty za těchto podmínek dominovaly (až 63%) v celkovém toku iontů ve vzdálenosti 200 mm od terče. Naše modelové výpočty naznačují, že pokles depoziční rychlosti při rostoucí průměrné výkonové hustotě v pulzu je charakteristikou HiPIMS modu rozprašování obecně a je nezávislý na konfiguraci depozičního systému.

K depozici vrstev oxidů zirkonu bylo použito totéž naprašovací zařízení doplněné o (i) systém napouštění reaktivního plynu, (ii) prstencovou anodu umístěnou v oblasti substrátu a (iii) řídící systém. Vrstvy byly deponovány ve směsi argonu a kyslíku při tlaku argonu 2 Pa. Opakovací frekvence pulzů byla 500 Hz a střída v rozmezí 2.5% – 10%. Byly deponovány transprentní (extinkční koeficient nižší než 4×10^{-3} při 500 nm) vrstvy oxidu zirkoničitého (ZrO_2). Vzrůst průměrné výkonové hustoty na terči z 5 Wcm^{-2} na 100 Wcm^{-2} při 10% střídě vedl k (i) nárůstu depoziční rychlosti z 11 nm/min na 73 nm/min a (ii) trojnásobnému poklesu poměru depoziční rychlosti ku průměrné výkonové hustotě na terči. Zvýšení průměrné výkonové hustoty v pulzu zkrácením pulzu (pokles střídy z 5% na 2.5%) způsobilo pokles depoziční rychlosti z 64 nm/min na 15 nm/min. Vrstvy ZrO_2 byly krystalické s převažující monoklinickou mřížkou. Jejich extinkční koeficient se pohyboval mezi 6×10^{-4} a 4×10^{-3} (při 550 nm) a tvrdost byla v rozmezí 10 GPa – 15 GPa. Tok iontů na substrát (i) byl tvořen převážně Ar^+ a Ar^{2+} ionty, (ii) obsahoval více kyslíkových iontů než iontů zirkonu a (iii) tok O^+ iontů dosahoval přinejmenším pětkrát vyšších hodnot než tok iontů O^{2+}. Pomocí dynamického modelu depozičního procesu bylo demonstrováno, že použité regulační zařízení, jehož vstupní veličinou je impedance výboje a které ovládá napouštění reaktivního plynu, je použitelné pro efektivnímu řízení reaktivních depozic vrstev oxidů zirkonu.